

CENTRO DE INVESTIGACIONES EN ÓPTICA, A. C.

SYNTHESIS, CHARACTERIZATION, AND APPLICATION OF MAGNETIC NANOPARTICLES FOR USE IN MAGNETIC HYPERTHERMIA

TESIS

QUE PARA OBTENER EL GRADO ACADEMICO DE:

DOCTOR EN CIENCIA Y TECNOLOGÍA EN INGENIERÍA AMBIENTAL

PRESENTA

M.C.A. LUIS FERNANDO GÓMEZ CABALLERO

DIRECTOR: DR. JUAN LUIS PICHARDO MOLINA

CODIRECTOR: DR. GUSTAVO BASURTO ISLAS



LEÓN DE LOS ALDAMA, GUANAJUATO, SEPTIEMBRE, 2025

Acknowledgments

Al culminar esta etapa tan significativa en mi formación académica y personal, quisiera expresar mi más profundo agradecimiento a quienes me acompañaron, guiaron y apoyaron a lo largo de este arduo pero enriquecedor camino.

En primer lugar, extiendo un sincero y respetuoso agradecimiento a mis directores de tesis, el Dr. Juan Luis Pichardo y el Dr. Gustavo Basurto. Su guía experta, paciencia y exigencia académica fueron fundamentales para el desarrollo de este trabajo. Agradezco profundamente la confianza que depositaron en mí, así como las valiosas discusiones y enseñanzas que enriquecieron no solo esta tesis, sino también mi visión científica y profesional.

A mi familia, por su amor incondicional, por creer en mí incluso en los momentos más inciertos, y por brindarme siempre un refugio de apoyo emocional. A mis amigos, quienes con su cercanía, palabras de aliento y compañía, me ayudaron a mantener el equilibrio durante los momentos más complejos del doctorado.

A Viridita, gracias por tu amor, tu comprensión infinita, tu apoyo constante y tu paciencia durante los momentos de ausencia y cansancio. Gracias por caminar a mi lado, celebrar mis logros y sostenerme en los momentos difíciles. Este logro también es tuyo.

Agradezco especialmente a los técnicos Christian Albor y Ricardo Valdivia por su disposición, profesionalismo y apoyo técnico en el laboratorio, sin los cuales muchos de los avances experimentales no habrían sido posibles.

También quiero expresar mi gratitud a las instituciones que hicieron posible esta etapa de formación: al SECIHTI por el apoyo financiero; a la Universidad de Guanajuato por brindarme un espacio de crecimiento académico; al PICYT, al Centro de Investigaciones en Óptica A.C. (CIO), y a la División de Ciencias e Ingenierías (DCI), por su infraestructura, recursos y entorno de colaboración que enriquecieron esta experiencia de manera significativa.

A todos, gracias por haber sido parte esencial de este trayecto. Cada palabra, gesto y contribución dejó una huella en este trabajo y en la persona que soy hoy.

Abstract

Nanotechnology has gained much attention in recent decades due to the unique properties and behavior of materials at the nanoscale. Many nanomaterials have been synthesized for medical applications, including diagnosis, controlling drug release, tissue engineering, and other treatments, such as magnetic hyperthermia. This treatment uses the properties of a specific group of metal oxide nanoparticles that release energy in the form of heat when stimulated by an alternating magnetic field. This heat triggers molecular processes associated with cell death; thus, nanoparticles could induce this effect within tumors, offering potential for cancer therapy. This work reports the synthesis, characterization, and application of magnetite (Fe₃O₄) as the heating agent in the magnetic hyperthermia treatment tested in human colorectal carcinoma cells (HCT 15 cell line) within *in vitro* models for further analysis by microscopy and western blotting for protein analysis.

Table of contents

	Acknowledgments	•••
	Abstract	i
	Table of contents	i
	List of Figures	i\
	List of Tables	. vi
	Abbreviations and acronyms	vii
1	. Introduction	1
	1.1 Background	1
	1.2 Statement of the problem	5
	1.3 Justification	5
	1.4 Objectives	5
	1.5 Hypothesis	6
2	. Literature	7
	2.1 Cancer	7
	2.1.1 Colorectal cancer (CRC)	13
	2.2 Nanomaterials	16
	2.3 Magnetic hyperthermia	17
	2.4 Synthesis methods of MNPs	20
	2.5 Biofunctionalization of MNPs	22
	2.6 Magnetization in the application of hyperthermia	25

	2.7 Characterization techniques for MNPs	. 28
	2.8 MHT frequency determination	. 31
3.	Synthesis, Characterization, and application of magnetite (Fe ₃ O ₄) nanoparticles	. 33
	3.1 Introduction	. 33
	3.2 Materials	. 33
	3.2 MNPs synthesis and bioconjugation	. 34
	3.3 MNPs characterization	. 36
	3.4 MNPs characterization results	. 37
	X-ray diffraction (XRD)	. 37
	Scanning electron microscopy (SEM)	. 38
	Magnetic properties	. 40
	Coil development	. 42
	MNPs heating	. 43
	Fourier Transform Infrared Spectroscopy (FTIR)	. 45
	3.5 MNPs selection for MHT	. 46
4.	Magnetic hyperthermia	. 48
	4.1 Materials	. 48
	4.2 Cell Culture and Toxicity Studies	. 48
	Cell culture	. 48
	WST-1 toxicity test	. 48
	MNPs specificity tests	. 49
	4.3 Magnetic hyperthermia and protein assay	. 49
	4.4 Protein Analysis	. 50
	4.5 Results of MNPs biocompatibility, specificity, and MHT in vitro	. 55
	Biocompatibility tests	. 55
	Specificity tests	. 56
	Magnetic hyperthermia	. 57
	Cell viability test	. 59
	Prussian Blue / Hematoxylin & Eosin staining	. 61
	Protein analysis	. 63
4.	Discussion	. 65
5.	Conclusions	. 67
Re	eferences	. 68

List of Figures
Figure 1.1. Cancer cells progress by multiple mutations in their DNA. After a series of mutations, cells are considered cancerous, as they start forming tumors
network of abnormal, tortuous, and hyperpermeable vessels with inconsistent diamet
diameters and functions
Figure 2.3. Anatomy, blood supply, and lymph node drainage of the large intestine. The three major parts relevant to colorectal cancer are labelled: colon, rectum, and anal canal. For the blood supply, only the arterial main supply is presented
small intestine, receiving processed material at the cecum, and includes the colon, rectum, and anal canal. A polyp is shown as part of a colonoscopy, an exam of the whole colon, performed by a flexible tube with a camera.
Figure 2.5. Schematic representation of superparamagnetic particles. The orientation of their magnetic moments is randomly aligned in the absence of an external magnetic field; they only get aligned in the presence of an external magnetic field and return to their unaligned orientation after removing the external magnetic field
Figure 2.6. Hysteresis loop of magnetic materials showing the magnetization (M) as a function of an applied magnetic field (H). The loop demonstrates that the material's magnetization lags behind the applied field
Figure 2.7. Schematic illustration of biofunctionalization of materials by bioconjugation. This diagram shows how different biomolecules, such as nucleic acids, carbohydrates, peptides, and proteins, can be attached to nanoparticles to perform a required task or enhance a particle's property
Figure 2.8. Representation of the domains in an integrin. These proteins are formed through noncovalent association of two type I transmembrane glycoproteins, the α - and the β subunits
Figure 2.9. Hysteresis curves of various types of magnetic materials. The magnetization, M, lags behind the applied field, B0, and traces out a characteristic curve known as the hysteresis loop. The applied field strength at which the magnetization reverses is called the coercive field. The width of the hysteresis loop indicates the hardness of the magnetic material

Figure 2.10. Geometry of X-ray diffractometer. In this configuration, an X-ray source with a line
focus emits a divergent incident beam that strikes a flat powder sample. The sample is
positioned such that its surface is tangent to the focusing circle. X-rays satisfying Bragg's Law
(nλ = 2d sinθ) for a given set of crystal lattice planes (hkl) are diffracted
Figure 2.11. Schematic diagram of a solenoid. A coil of N = 8 turns is wound around a high-
permeability (µ) ferromagnetic core, forming a closed magnetic path with a cross-sectional
area A and a mean path length ℓ . The core is constructed with a pole piece to direct the
magnetic flux
Figure 3.1. Schematic diagram of the MNPs synthesis system by coprecipitation. A
concentrated NaOH solution is added dropwise into an Fe $^{2+}$ and Fe $^{3+}$ salt solution to form Fe $_3$ O $_4$
nanoparticles. They were synthesized A) under a nitrogen atmosphere, and B) under ambient
conditions
Figure 3.2. Schematic diagram of the MNPs synthesis system by chemical reduction. A solution
of FeCl2 is added to an octadecylamine (ODA) solution under a nitrogen atmosphere and
almost at the boiling point of its solvent
Figure 3.3. X-ray diffraction patterns of MNPs synthesized by coprecipitation under air (black
line) and nitrogen atmosphere (red line), and by reduction in water (blue line), and EG (green
line). All of the patterns present the characteristic peaks of magnetite at 30.43, 35.81, 43.46,
53.78, 57.30, and 62.89°
Figure 3.4. SEM images of MNPs synthesized by coprecipitation and coated with DMSA. A) A-
MNPs. B) N-MNPs. Size distribution histograms of C) A-MNPs and D) N-MNPs. The average
diameters for MNPs synthesized by coprecipitation were 15.0 \pm 3 nm and 23 \pm 5 nm 39
Figure 3.5. SEM images of MNPs synthesized by reduction and coated with NH2 groups. A) W-
MNPs and B) EG-MNPs. Size distribution histograms of C) W-MNPs and D) EG-MNPs. The
average diameters for MNPs synthesized by reduction were 35 \pm 9 nm and 34 \pm 7 nm 40
Figure 3.6. Magnetic characterization of MNPs synthesized by coprecipitation. A) M-H
hysteresis loops of A-MNPs and N-MNPs measured at 300 K. B) M-H hysteresis loops of N-
MNPs measured at 300 and 2 K
Figure 3.7. Magnetic characterization of MNPs synthesized by reduction, M-H hysteresis loops
of EG-MNPs and W-MNPs measured at 300 K from a range from -3 to 3 kOe
Figure 3.8. Diagram of the MHT heating system consisting of a commercial ZVS circuit
connected to a 24 V power supply and cooled with water. The temperature change of the
stimulated MNPs was recorded with an IR thermal camera44
Figure 3.9. MNPs heated at different concentrations, 100, 250 and 500 µg/ml. A) MNPs
synthesized by coprecipitation, A-MNPs and N-MNPs. B) MNPs synthesized by reduction, W-
MNPs and EG-MNPs. C) The concentration of 250 µg/ml resulted to be the best in both
syntheses, reaching an elevation of 6.8 and 8.9 $^{\circ}$ C, respectively. N-MNPs (solid lines) and EG-
MNPs (dashed lines)
Figure 3.10. FTIR spectra of MNPs synthesized by coprecipitation. Bare-MNPs did not show
any significant peak, while MNPs coated with DMSA (blue line) presented the appearance of
peaks corresponding to the v(C=O), C-H, and O-H bands. MNPs@RGD (purple line) presented
the appearance of peaks corresponding to different amine groups, C=N and C-N
Figure 4.1. Schematic diagram for MHT application in vitro. 3 x 3 well arrangements were cut
and sterilized to cultivate cells for 24 hours. Then they were added with different MNPs

concentrations (0 - 1000 $\mu g/ml$) and incubated again for 24 hours. Finally, they were taken to
the MHT system for stimulation 50
Figure 4.2. Order of assembly of a transfer cassette. The stack is assembled between the
negative (-) and positive (+) electrodes of a transfer apparatus. From cathode to anode, the
stack consists of: the cathode transfer clip slide, a sponge, a sheet of filter paper, the
polyacrylamide gel, the PVDF membrane, a second sheet of filter paper, a second sponge, and
the anode transfer clip slide 53
Figure 4.3. Cellular viability percentages for different MNPs concentrations, bare Fe3O4, and
coated with DMSA. Both groups of MNPs present a linear tendency of toxicity as the particles
concentration increases. Nonetheless, DMSA-MNPs only presented a 21 $\%$ cell death at the
highest concentration (250 μ g/ml), while bare MNPs reached a 53 % cytotoxicity 55
Figure 4.4. Combined PB and H&E staining of HCT-15 and HEK 293 cell lines treated with
increasing concentrations (0, 50, 100, 200 µg/ml) of MNPs@RGD. A, C, E, G (HCT-15 cells)
Show internalized MNPs@RGD (dark blue, indicated by arrows) and cytoplasm (pink). B
D, F, H (HEK 293 cells): Show minimal MNP uptake, with only occasional agglomerations
outside cells (arrows) and pink cytoplasmic staining.
Figure 4.5. Temperature rise means in the cell cultures exposed to an AMF with different
MNPs@RGD concentrations. A) 0 μg/ml. B) 100 μg/ml. C) 200 μg/ml. D) 1000 μg/ml. In the
absence of MNPs, there was only an elevation of 3 °C; in the following concentrations: 100, 200
and 1000 µg/ml, the temperature increased over 5 °C
Figure 4.6. WST-1 cell viability assay after exposing cells to MHT. The increase in MNPs
concentration in MHT significantly reduced their viability. In the absence of MNPs, but with
magnetic stimulation, cellular viability was reduced by ~ 10 %, it dropped by ~ 15 % with a 100
μ g/ml concentration, and by ~ 45 and 80 % with concentrations of 200 and 1000 μ g/ml
respectively
Figure 4.7. PB and H&E combination stain on cells treated by MHT with different MNPs
concentrations. A), B) 0 μg/ml. C), D) 100 μg/ml. E), F) 200 μg/ml. G), H) 1000 μg/ml. The cellular
morphology and integrity were lost as the MNPs' concentration increased
Figure 4.8. Gel electrophoresis for evaluation of protein integrity after MHT. The control lanes
do not show significant protein degradation. Nonetheless, the lanes with proteins that were
treated with 100, 200, or 1000 µg/ml show the disappearance of high MW bands or protein
agglomeration. 64
Figure 4.9. Western blot for GAPDH (37 kDa). The band only appeared in the control lane and
the one with no MNPs. While in the groups treated by MHT with MNPs, the band did not appear
indicative of protein denaturation 64

List of Tables

Table 2.1. Temperature effect on Biological Tissues	17
Table 2.2 Summary comparison of MNPs synthetic methods	19
Table 2.3. Effects of coating on MNPs	22
Table 3.1. Magnetic parameters of the M-H hysteresis loops	42
Table 3.2. Coil settings and parameters summary	43
Table 3.3 Temperature increase generated by MHT in MNPs	43
Table 3.4 SAR values for MNPs	44
Table 4.1. Solutions for preparing electrophoresis gels	51
Table 4.2. Blocking conditions	53
Table 4.3. Incubation conditions for primary antibodies	54
Table 4.4. Secondary antibody incubation conditions	54
Table 4.5. Cellular viability for cells exposed to MHT	60

Abbreviations and acronyms

Alternating magnetic field (AMF)

Antiferromagnetic (AFM)

Blocking temperature (TB)

Coercivity (HC)

Colorectal cancer (CRC)

Curie temperature (TC)

Diamagnetic (DM)

Dulbecco's Modified Eagle's Medium (DMEM)

Electromagnetic (EM)

1-ethyl-3-(3-dimethylaminopropyl) carbodiimide (EDC)

Ethyleneglycol (EG)

Extracellular matrix (ECM)

Far infrared (FIR)

Fetal bovine serum (FBS)

Ferromagnetic (FOM)

Ferrimagnetic (FIM)

Fourier Transform Infrared Spectrometry (FTIR)

Frequency (f)

Full width at half the maximum height (FWHM)

Glyceraldehyde-3-phosphate dehydrogenase (GADPH)

Hematoxylin and Eosin (H & E)

Hydrochloric acid (HCI)

Hyperthermia (HT)

Infrared (IR)

Magnetic field strength (H)

Magnetic fluid hyperthermia (MFH)

Magnetic hyperthermia (MHT)

Magnetic nanoparticles (MNPs)

Magnetic resonance imaging (MRI)

Magnetic saturation (MS)

Middle infrared (MIR)

Meso-2,3-dimercaptosuccinic acid (DMSA)

Molecular weight (MW)

Molecular weight marker (MWM)

Nanoparticles (NPs)

National Cancer Institute (NCI)

Near infrared (NIR)

N-hydroxysuccinimide (NHS)

Nuclear magnetic resonance (NMR)

Octadecylamine (ODA)

Paramagnetic (PM)

Photothermal therapy (PTT)

Prussian Blue (PB)

Radiofrequency (RF)

Remnant magnetization (M)

Roswell Park Memorial Institute (RPMI 1640)

Scanning electron microscopy (SEM)

Superparamagnetic (SPM)

Tetramethylbenzidine (TMB)

World Health Organization (WHO)

X-ray diffraction (XRD)

CHAPTER 1 INTRODUCTION

1. Introduction

1.1 Background

General information on cancer

Cancer is a disease characterized by a group of abnormal cells that grow uncontrollably, ignoring the rules of cell division. Normal cells undergo cell signaling, inducing division, differentiation, or apoptosis. On the other hand, cancer cells develop a degree of autonomy over these signals, resulting in uncontrolled growth and proliferation [1].

A single abnormal cell (clonal origin) can cause cancer due to an alteration in the DNA sequence (mutation). The uncontrolled proliferation of these cells leads to a second mutation, which continues and expands in these cells, causing the formation of tumors (Figure 1.1). Subsequent rounds of mutation and expansion generate growth and metastasis of the cancer, which breaks through the basal membrane surrounding tissues and spreads to other parts of the body.

The onset and progression of cancer depend on external factors and lifestyle, such as physical inactivity, overweight, diet, tobacco, alcohol, and drugs, as well as intracellular factors like inherited mutations, hormonal, immunological conditions, and metabolic mutations. These factors may act together or separately, resulting in abnormal cell behavior and excessive proliferation. As a result, cell masses grow and expand, which affects nearby tissues and may spread to other regions of the body [2].

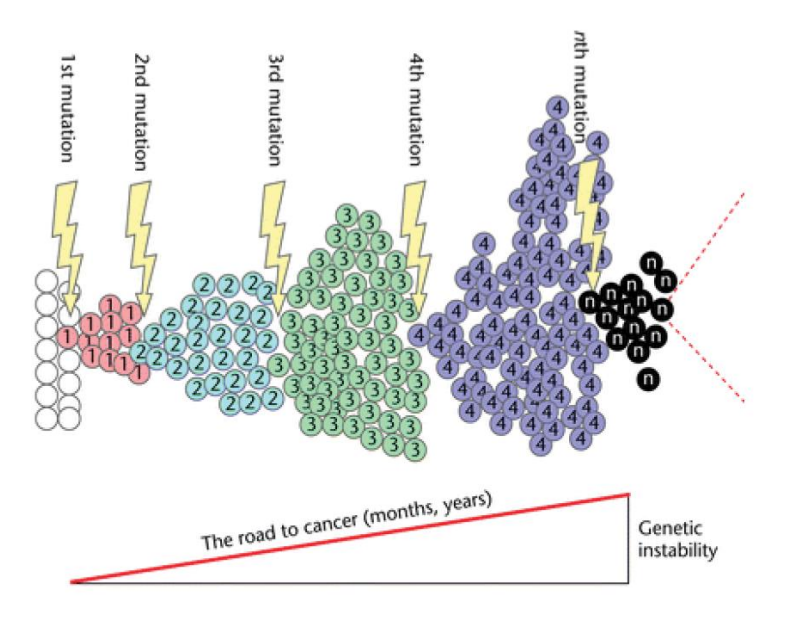


Figure 1.1. Cancer cells progress by multiple mutations in their DNA. After a series of mutations, cells are considered cancerous, as they start forming tumors.

Colorectal cancer

In colorectal cancer, growth initially occurs in the inner lining of the large intestine, and then it may spread to the wall of the colon or rectum (Figure 1.2). Once the cancer reaches the walls, it can penetrate the blood or lymphatic vessels. Cancer cells usually spread to nearby lymph nodes first and can also be transported in blood vessels to the liver, lungs, or other organs and tissues. The staging of cancer at the time of diagnosis is known as its stage. This is essential for determining treatment options and assessing prognosis [2].

In most cancers, the tumor takes months or years to be detectable. In colorectal cancer, the growth from precancerous polyps to invasive cancer provides a unique opportunity for prevention and early detection. Monitoring helps detect cancer early, making treatment more successful. It also reduces mortality by decreasing the incidence and increasing survival rates.

According to the World Health Organization (WHO), colorectal cancer is the second leading cause of cancer-related deaths worldwide. In 2020, more than 1.9 million new cases of colorectal cancer and more than 930,000 deaths due to colorectal cancer were estimated to have occurred worldwide [3].

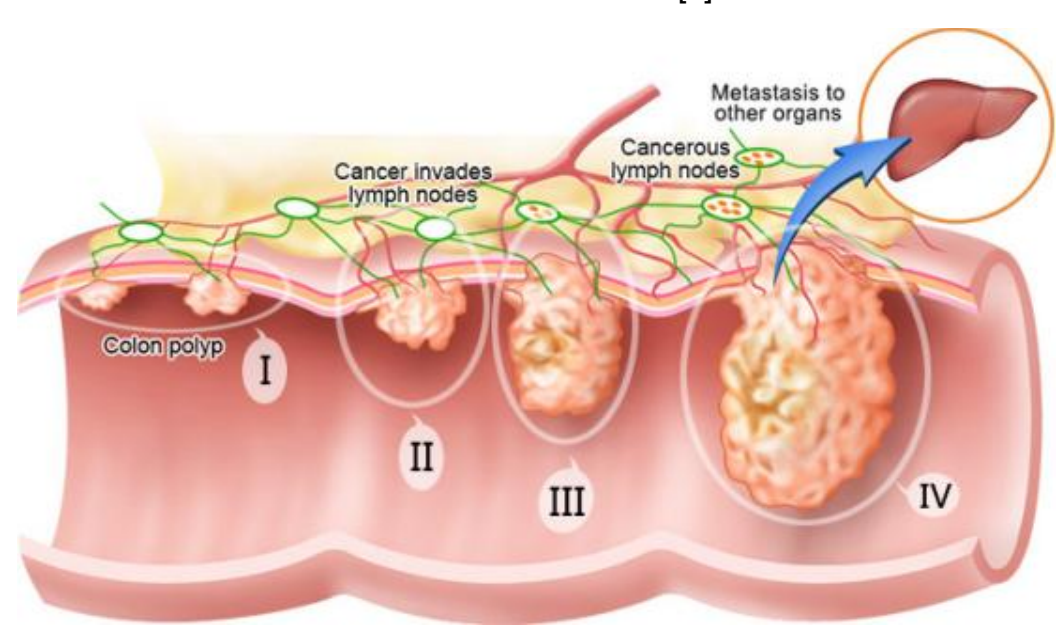


Figure 1.2. Stages of colorectal cancer. It starts growing in the inner lining of the large intestine, then it can penetrate the blood or lymphatic vessels to finally metastasize to other organs.

Treatments

As with other cancers, the treatment of colorectal cancer is delicate and requires good follow-up since, in addition to the removal of the tumor, in most cases, it is necessary to supplement the treatment with chemotherapy and radiotherapy. The treatment of patients with colorectal cancer is mainly based on the stage at which it

occurs, emphasizing the importance of a comprehensive strategy for diagnosis, evaluation, and treatment [4].

Current cancer treatments can cause side effects, problems that occur when treatment affects healthy organs or tissues. These vary from person to person, even when receiving the same treatment. Some people have only a few side effects, while others have many. Factors that influence this include the type of treatment, the frequency or amount of treatment, age, and other health conditions present in the patient [5]. However, it is important to note that, at this stage, any cancer treatment results in the death of a large number of normal cells. Therefore, developing new therapies is crucial.

Hyperthermia

Hyperthermia (HT) is defined as an abnormally high body temperature. This may be caused by infection, exposure to heat, or treatment. In hyperthermia treatment, body tissue is exposed to high temperatures to damage and eliminate cancer cells, either alone or as an adjuvant by sensitizing cells to radiation and certain anti-cancer drugs [6].

Since the late 19th century, doctors have observed that patients with high fever had an unusual reduction in the number of cancerous cells. In addition, some studies have shown that at moderately elevated temperatures (< 45 °C), there is a significant regression or destruction of the tumors. Therefore, heat treatment originated as an option for the destruction of cancer cells.

HT treatment is divided into two types: external and internal hyperthermia. In the external type, heat is applied from outside the body using microwaves, radio frequencies, ultrasound, and other methods. Conversely, the internal type introduces substances into the body that act as sources of heat [7]. The National Cancer Institute (NCI) recognizes three types of hyperthermia.

- 1. Local HT: exposes a small area, such as a tumor, to high temperatures.
- 2. Regional HT: heat is applied to a large area of tissue, such as an organ, cavity, or limb.
- 3. Whole-body HT: used to treat metastatic cancer that has already spread throughout the body

HT is classified according to the source of heating and the nature of the heated target, ranging from whole-body to local and interstitial levels (Fig. 1.3). The basis of magnetic hyperthermia (MHT) modalities is the insertion of heating sources where macroscopic mediators are inserted into the body by precise interventions. In contrast, micro- or nano-scale mediators are injected in the form of a colloidal dispersion of magnetic particles, called magnetic fluid hyperthermia (MFH).

LOCAL HYPERTHERMIA

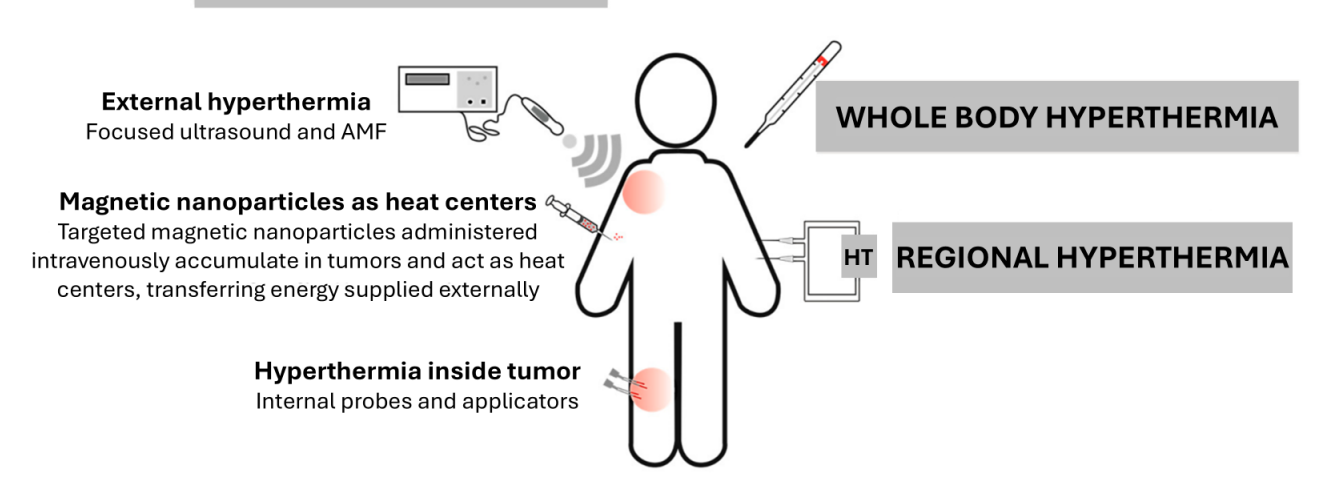


Figure 1.3. Types of HT used in cancer therapy, depending on their extension, they are classified as local HT, whole body HT, and Regional HT. Abbreviations: alternating magnetic field (AMF), hyperthermia (HT).

MFH involves the use of a magnetic nanofluid in an alternating magnetic field of a specific intensity and frequency, causing the particles to heat through the loss of magnetic hysteresis or Neel relaxation.

Nanoparticles (NPs) are particles with a nanometric dimension range (between 1 and 100 nm). NPs have a high surface-to-volume ratio, which makes them very reactive, versatile, and strong compared to bulk material. These properties provide many possibilities for improving the mechanical, optical, and magnetic properties of NPs [8]. Magnetic nanoparticles (MNPs) have garnered significant attention due to their capability for functionalization in biomedical applications. [9]

MNPs are inorganic, zero-dimensional materials with metal-based configurations. These NPs have gained significant importance because they can be easily manipulated using an alternating magnetic field (AMF) and subsequently used in various applications. MNPs exhibit intrinsic and unique properties, such as high magnetic saturation (Ms), biocompatibility, and low toxicity.

It has been proposed that MNPs give HT a safe, easy, and practical approach to cancer treatment. This is due to the use of MNPs with high Ms, which produce heat to improve treatment efficiency. The route of administration may be by local injection or in the nearby intravascular region while an external AMF is applied. This leads to heat being concentrated in the affected cells, known as magnetic hyperthermia or magnetic nanofluid hyperthermia (MNFHT). In which magnetic fluids are used as stable colloidal suspensions of NPs in liquid media.

1.2 Statement of the problem

The necessity of developing novel materials with multifunctional capabilities is vital for technological advancement. Nanotechnology, a rapidly progressing field, offers numerous applications within this size regime. For instance, in biomedicine, nanomaterials can be engineered to perform singular or multiple functions, contingent upon their composition, design, and preparation methodology.

Most routes to synthesize nanomaterials require complex systems and equipment to apply and carry out determined conditions, such as high temperatures, pressures, or atmospheres, among others. The cost of these devices tends to be high, and they often require specialized installations, which also demand high energy consumption.

In this work, we synthesized magnetite nanoparticles using basic lab equipment to obtain nanoparticles with high crystallinity, size monodispersity, superparamagnetism, and biocompatibility, excellent properties for using these MNPs in MHT. In addition, the proposed methodology can be considered green chemistry, as it does not require the use of toxic reagents and is performed at ambient temperature, only requiring magnetic stirring and a nitrogen atmosphere.

1.3 Justification

This work aims to develop magnetite nanoparticles that can act as heating agents in MHT. Most of the particles reported in the specialized literature, used for this treatment, are synthesized in organic solvents with high boiling points, making them cytotoxic and water-insoluble; therefore, further functionalization steps are required to enable their use in biological systems. Here, we developed nanoparticles capable of performing MHT without requiring organic solvents or high temperatures for their synthesis, making the synthesis route more eco-friendly than most currently employed particle preparation methodologies. Additionally, our particles were tested for MHT, yielding promising results in in vitro models.

1.4 Objectives

General

To develop magnetite nanoparticles (MNPs) by a modified method for their use in MHT in *in vitro* cancer models.

Specific

- To synthesize and characterize superparamagnetic MNPs.
- To functionalize MNPs to enhance their biocompatibility and specificity toward cancer cells.
- To determine the biocompatibility and target specificity of functionalized MNPs.
- To evaluate the ability of MNPs in generating magnetic hyperthermia therapy.

• To identify proteins involved in cellular metabolic pathways that are affected following magnetic hyperthermia therapy.

1.5 Hypothesis

Magnetite nanoparticles synthesized by the co-precipitation method at room temperature exhibit superparamagnetic properties and show specificity toward cancer cells after bioconjugation, making them suitable for inducing magnetic hyperthermia and promoting cancer cell death through protein denaturation.

CHAPTER 2 LITERATURE

2. Literature

In this chapter, it is presented the literature review of the main characteristics of cancer, how it is treated, and how new technologies as nanomaterials and targeted therapy, are being used to treat this disease. As part of these novel therapies, magnetic nanoparticles are presented as the cornerstone of this work; they are briefly described, and how they can be evaluated to achieve magnetic hyperthermia treatment.

2.1 Cancer

Cancer is a life-threatening disease caused usually by environmental factors that mutate genes responsible for coding proteins critical to cellular regulation. These factors lead to aberrant cellular behavior, resulting in abnormal cell masses that expand and destroy healthy tissue in the surrounding environment. The cancer then spreads to vital organs, resulting in a disseminated disease that commonly leads to death [1].

By 2040, it is expected to have 30 million new cases of cancer and 15.3 million deaths. One of the leading causes of this is increased life expectancy and the fact that most cancers are more common in older people, combined with the lifestyle adopted (junk food, smoking cigars, and drinking alcohol), which are the causes of about 30% of cases. Today, cancer treatment is very expensive, so it's crucial to prioritize early detection. By identifying and classifying the type of cancer being treated, a more accurate prognosis can be obtained, and a tentative treatment plan can be developed [3].

Classification

Tumors are classified according to their behavior as 'benign' or 'malignant.' The former are usually slow-growing masses that, instead of invading surrounding tissue, only compress it. They generally do not represent a major threat and may be easily removed. However, in some cases, they have malignant potential, especially those developed in the large intestine, which must be eliminated before they develop malignancy by invading nearby tissue [1].

Nomenclature

Usually, the suffix "oma" is used to denote a benign tumor. In the case of glandular epithelium, it is called "adenoma," and the superficial epithelium is called "papilloma." Malignant tumors of epithelium and connective tissue are called "carcinoma" and "sarcoma," respectively. There are also some exceptions to this nomenclature. Leukemia and lymphoma refer to tumors in the bone marrow and lymphatic system, respectively [1].

Hallmarks of cancer

They are comprised of six biological abilities acquired during tumor development. They are organized in such a way that they can rationalize the complexities of this neoplastic disease (Fig. 2.1) [10]. They consist of sustaining proliferative signaling, evading growth suppressors, resisting cell death, enabling replicative immortality, inducing angiogenesis, and activating invasion and metastasis.

- Sustaining proliferative signaling
 It is the ability to maintain chronic proliferation by producing proteins that allow them to continue with it.
- Evading growth suppressors
 Cancer cells disregard the inhibitory signals that regulate cell growth, allowing them to continue their growth and proliferation.
- Resisting cell death
 Tumor cells develop several strategies to limit or prevent apoptosis, the most common being the loss of the TP53 tumor suppressor function, which eliminates this cell damage sensor that induces apoptosis. At the same time, cells increase the expression of anti-apoptotic regulatory proteins.
- Enabling replicative immortality
 Tumor cells maintain telomeric DNA long enough to prevent senescence or apoptosis by regulating telomerase expression or with a telomere maintenance mechanism.
- Inducing angiogenesis
 Tumor cells require nutrients and O₂, as well as the ability to eliminate metabolic waste and CO₂. These cells release pro-angiogenic factors to produce neovascularization from nearby vessels.
- Activating invasion and metastasis
 Cells migrate from the primary tumor to another site through the blood or lymphatic system, and metastases cause almost 90% of cancer deaths [10].

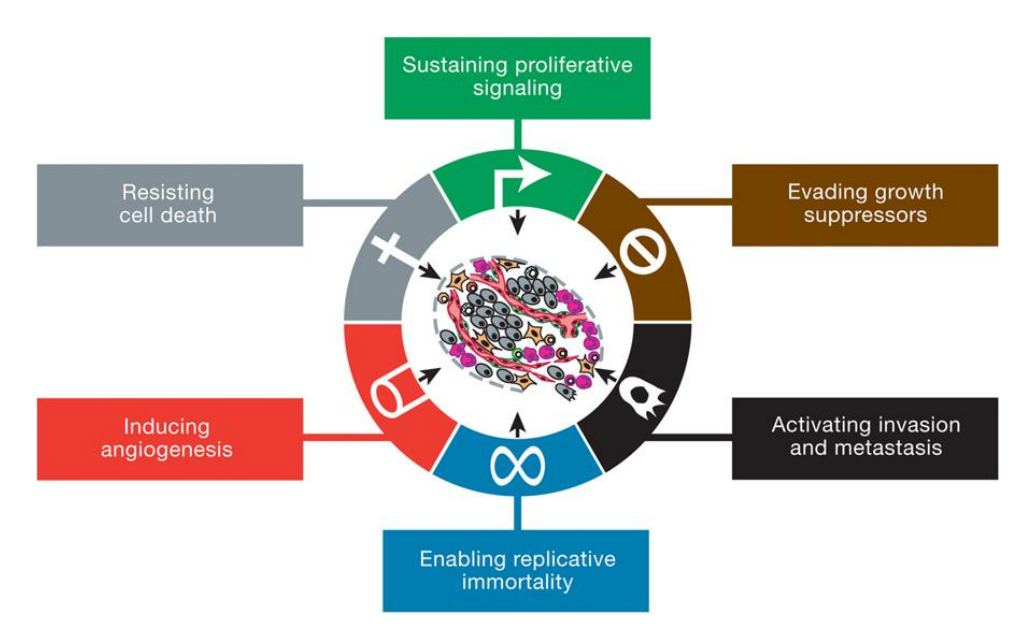


Figure 2.1. The Hallmarks of Cancer describe fundamental capabilities acquired by cancer cells as they develop tumors, including sustaining proliferative signaling, evading growth suppressors, resisting cell death, enabling replicative immortality, inducing angioge angiogenesis, and activating invasion and metastasis.

Treatment

The cancer treatment landscape has changed dramatically in recent years. The time when surgery and radiation therapy were the only effective ways to combat tumor growth is over. Currently, a scenario is emerging where the molecular characteristics of tumors appear to be the cornerstone of any therapy. There is an overview of different approaches to cancer treatment, including some classical therapies for cancer, including surgery, radiation therapy, chemotherapy, and endocrine therapy, among others [11,12].

Surgery is the most effective treatment for well-located primary and lymphatic tumors. When used as a single treatment, surgery heals more patients than any other cancer therapy used individually because surgery kills 100% of the cells removed. On the other hand, chemotherapy and radiation therapy can only kill a percentage of tumor cells with each treatment, so these processes are complementary.

In the last couple of decades, there have been significant improvements in both surgical technique and the use of combined modality therapy, which has significantly reduced morbidity and mortality associated with surgery for solid neoplasms.

Surgery

Small, thin knives called scalpels and other sharp tools are used in surgery to cut through the body during the process. Surgery often requires cuts through the skin,

muscles, and even bones. After surgery, these cuts may be painful and may take some time to heal.

In this procedure, anesthesia prevents pain during surgery. This refers to drugs or other substances that cause loss of sensitivity or awareness, depending on the type of anesthesia used: local, regional, or general.

Other ways of performing surgery do not involve scalpel cuts, such as cryosurgery, laser surgery, and photodynamic therapy, among others.

Radiotherapy

It is a cancer treatment that uses high doses of radiation to kill cancer cells and reduce the size of tumors. Cancer cells whose DNA is damaged stop dividing or die. When the damaged cells die, the body breaks them down and eliminates them.

This therapy does not destroy cancer cells immediately. Days or weeks of treatment are needed before the DNA is damaged enough that cancer cells die.

There are two main types of radiation therapy, external and internal beam. External beam radiation therapy comes from a machine that directs the radiation to the cancer. Internal radiation therapy is a local treatment, meaning it treats a specific body part. In it, a source of radiation, which can be solid or liquid, is placed inside the body.

Chemotherapy

It is a type of cancer treatment that uses drugs to kill cancer cells. It works by stopping or slowing the growth of cancer cells, which grow and divide rapidly. This therapy can be used to treat cancer by decreasing the chance of it coming back after another treatment and also by stopping or slowing its growth. This therapy can also relieve some symptoms of cancer, such as reducing tumors that cause pain and other problems.

Chemotherapy destroys rapidly growing cancer cells and kills or slows down the growth of healthy cells that grow and divide quickly, such as oral and intestinal mucosa cells and follicular epithelium cells. This treatment can cause side effects, such as mouth sores, nausea, and hair loss. However, the side effects usually improve or disappear after the chemotherapy ends.

Novel therapies have also recently emerged in the age of directed therapy, including new antibodies, small molecules, antiangiogenic agents, viral therapy, gene therapy, and hyperthermia.

Hyperthermia

Hyperthermia (HT), also known as heat therapy or thermotherapy, is used in addition to surgery, radiation therapy, chemotherapy, gene therapy, and immunotherapy. HT consists of raising the body's temperature or a particular region above a temperature

threshold set by the body's thermoregulation system [13]. In oncology, an artificial way to increase body tissue temperature is by supplying heat from external sources to destroy cancer cells or prevent their growth. HT works in a temperature range from 40 to 48 °C for one hour or more. Other thermal therapies are defined by the temperature range in which they work; for example, coagulation is in ranges > 50 °C, thermal ablation between 60 and 90 °C, and carbonization at > 200 °C [14–16].

Biological principles of hyperthermia

Several studies have shown that high temperatures directly damage cancer cells and sensitize them to other treatment modalities (radiotherapy, chemotherapy, immunotherapy, gene therapy), usually producing minimal or no injury to healthy tissue, so it is considered an adjuvant therapy [6,17]. HT can kill cells independently, and it helps eliminate radiation-resistant cells deeper into tumors due to hypoxic conditions. It also improves the effects of chemotherapeutic agents and increases immune system reactions against the tumor.

Cell death depends on the heating duration and the temperature levels reached in a determined number of treatment sessions. The higher the temperature and the longer the tumor is exposed to heat, the more lethal the effect will be, and the cells will generate no thermotolerance. By raising the temperature above its physiological level, intracellular proteins are denatured, destabilizing the membrane, cytoskeleton, enzymes, signal transduction, macromolecular synthesis, and nucleus, as well as producing changes in blood flow, vascular permeability, and tumor oxygenation. Finally, the heated cells are necrotic or apoptotic, dead or sensitized to radio or chemotherapy [18,19].

Environmental and vascular conditions are also important. Damage to cancer cells is promoted by chronic hypoxia, decreased pH, nutrient deprivation, and poor cooling caused by pathological microvasculature found within the tumor (Fig. 2.2). These conditions are not seen in healthy tissue and therefore it is not affected by heat treatment [20].

A) Normal vasculature

B) Cancer vasculature

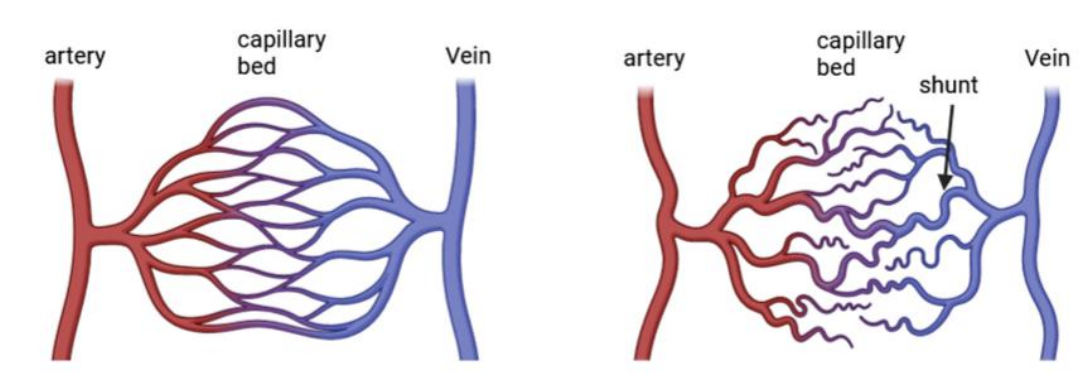


Figure 2.2. The difference between normal vasculature, which is a system of stable vessels with consistent diameters and functions, whereas cancer vasculature is a chaotic, immature network of abnormal, tortuous, and hyperpermeable vessels with inconsistent diameters and functions.

Methods of hyperthermia

There are three clinical methods of hyperthermia with high-temperature application, depending on the location, depth, and tumor staging: local, regional, and whole-body. In local hyperthermia, heat is transferred to localized neoplasms, where the heating temperature can reach 80 °C for complete tumor ablation [21]. Regional hyperthermia is used for advanced or deep neoplasms; the goal is to achieve specific physiological effects, such as cell death, without causing serious injury to the adjacent normal tissue, so the heating temperature is usually 41-45 °C [22]. In full-body hyperthermia, a heating temperature of 39-41 °C is used to mimic the effects of fever and not damage healthy tissue; this method, with more moderate temperatures, is used in combination with other therapies to treat metastatic cancer and widespread neoplasms [14].

Different types of energy are currently used for heat application and hyperthermia induction. One of the most common methods is exposure to external stimuli, such as infrared (IR) light, or immersing the tumor in a hot water bath. However, it is only used for easily accessible tumors because of its difficulty in application and lack of spatial control. Another widely used method is the insertion of metal probes into the tumor and raising its temperature by supplying it with specified amounts of energy using radio waves or microwaves, thus allowing rapid and substantial increases in temperature, which is suitable for ablation [23]. Techniques such as high-intensity focused ultrasound allow non-invasive warming of internal organs and are very promising for local hyperthermia of deep tumors [24]. Recently, nanomaterials activated by external energy sources have been used for local hyperthermia [25]. Distributing nanoparticles (NPs) evenly throughout the tumor allows better temperature control and a more even temperature distribution [26]. These

advantages facilitate studies on how local hyperthermia stimulates the antitumor immune response.

2.1.1 Colorectal cancer (CRC)

Introduction

The adult large intestine includes the colon, rectum, and anal canal. The colon can be divided into the right colon (cecum, ascending colon, and right 2/3 transverse colon) and left colon (left 1/3 transverse colon, descending colon, and sigmoid colon). The blood supply of the colon is mainly from the mesenteric artery; the veins are accompanied by the arteries of the same name, and the lymphatic network drains through the regional lymph nodes (Figure 2.3). The colon is innervated by the vagus and pelvic nerves. The function of the right colon is mainly to absorb water and some nutrients, while the main function of the left colon is to store and excrete feces. Notably, the colon secretes gastrointestinal hormones and alkaline mucus substances.

Based on sites of onset, rectal cancer accounts for 49.66%, colon cancer accounts for 49.09%, and both sites combined account for 1.25%. Among colon cancers, the most common sites are the sigmoid colon (55%), followed by the ascending colon (23.3%), transverse colon (8.5%), descending colon (8.1%), cecum (8.0%), and crossing site (2.1%) [27].

Overview

Colon cancer is a growth of cells that begins in a part of the large intestine called the colon. The colon is the first and longest part of the large intestine. The large intestine is the last part of the digestive system. The digestive system breaks down food for the body to use.

Colon cancer typically affects older adults, though it can happen at any age. It usually begins as small clumps of cells called polyps that form inside the colon. Polyps generally aren't cancerous, but some can turn into colon cancers over time.

Polyps often don't cause symptoms. For this reason, doctors recommend regular screening tests to look for polyps in the colon. Finding and removing polyps helps prevent colon cancer.

If colon cancer develops, many treatments can help control it. Treatments include surgery, radiation therapy, and medicines, such as chemotherapy, targeted therapy, and immunotherapy.

Colon cancer is sometimes called colorectal cancer. This term combines colon cancer and rectal cancer, which begins in the rectum [28].

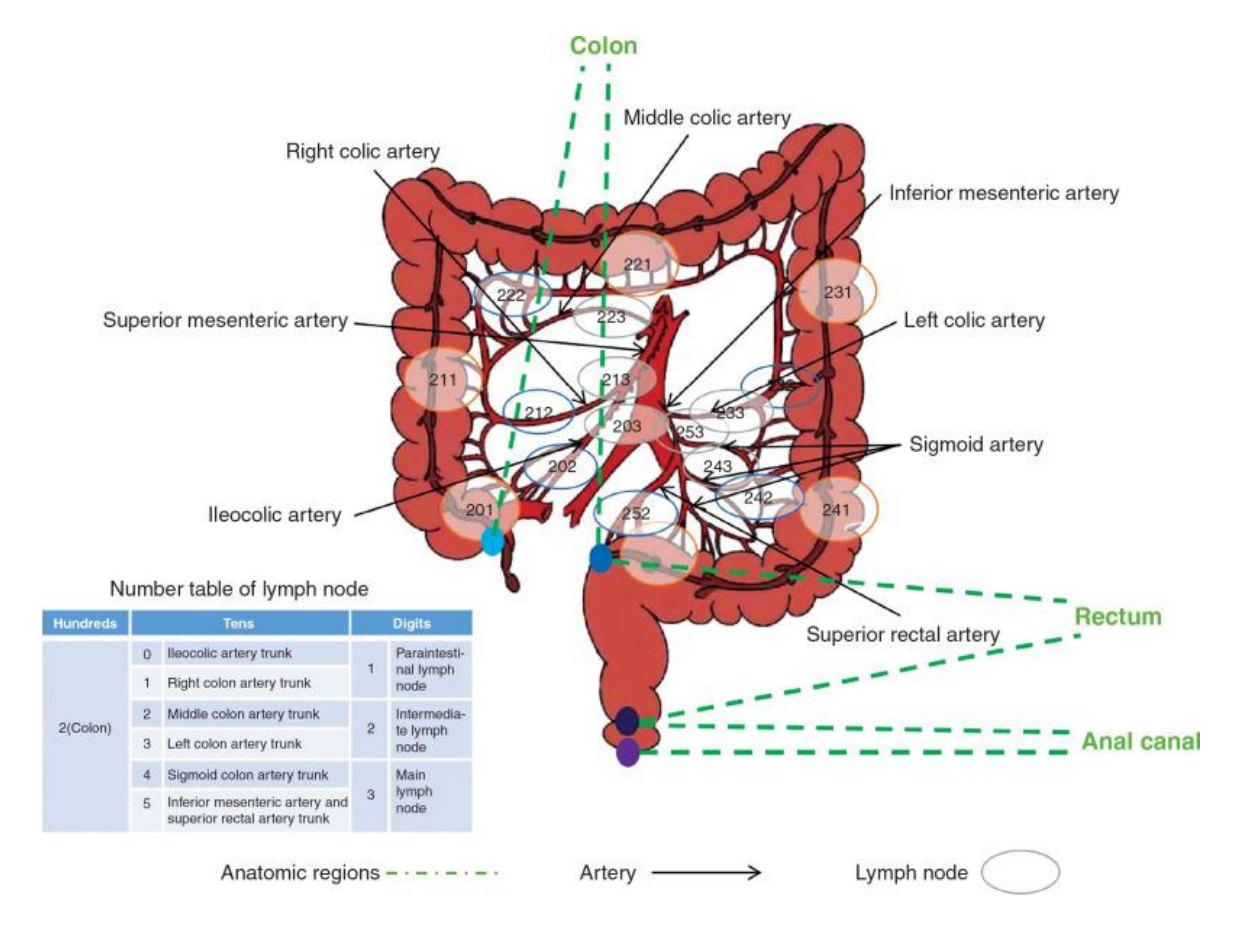


Figure 2.3. Anatomy, blood supply, and lymph node drainage of the large intestine. The three major parts relevant to colorectal cancer are labelled: colon, rectum, and anal canal. For the blood supply, only the arterial main supply is presented.

Symptoms

Many people with colon cancer don't have symptoms at first. When symptoms appear, they'll likely depend on the cancer's size and where it is in the large intestine (Figure 2.4).

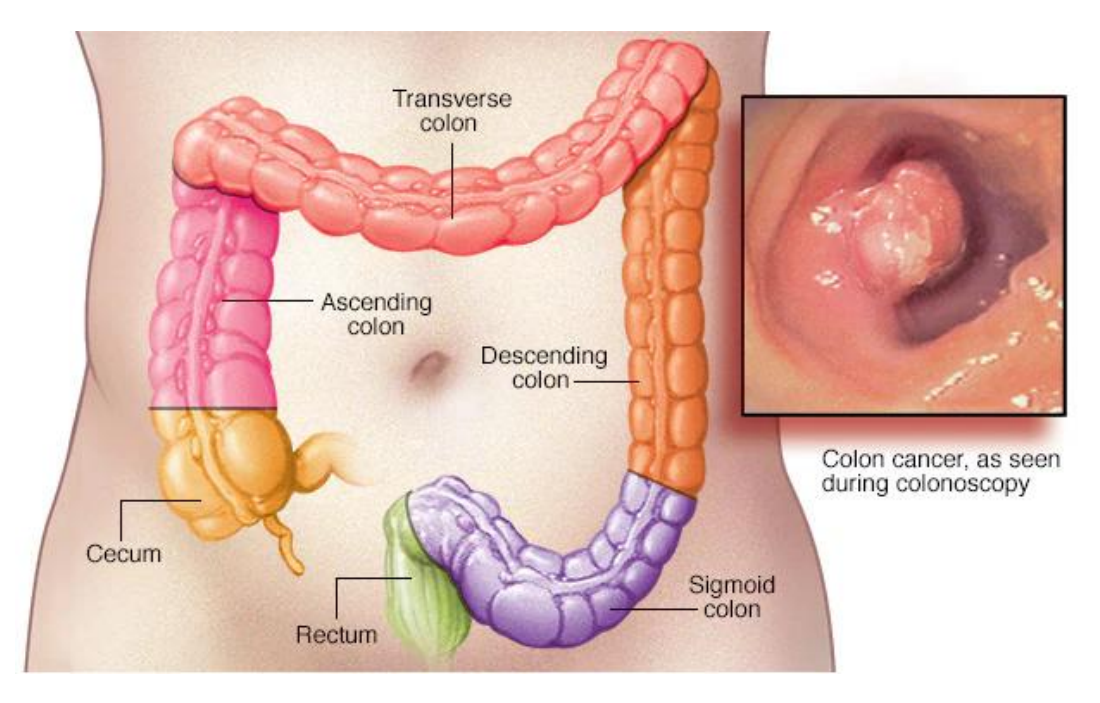


Figure 2.4. Colon cancer anatomy and internal view given by colonoscopy. It extends from the small intestine, receiving processed material at the cecum, and includes the colon, rectum, and anal canal. A polyp is shown as part of a colonoscopy, an exam of the whole colon, performed by a flexible tube with a camera.

Symptoms of colon cancer can include:

- A change in bowel habits, such as more frequent diarrhea or constipation.
- Rectal bleeding or blood in the stool.
- Ongoing discomfort in the belly area, such as cramps, gas, or pain.
- A feeling that the bowel does not empty during a bowel movement.
- Weakness or tiredness.
- Losing weight without trying.

Causes

Colon cancer happens when cells in the colon develop changes in their DNA. A cell's DNA holds the instructions that tell the cell what to do. The changes tell the cells to multiply quickly. The changes let the cells continue living when healthy cells die as part of their natural lifecycle.

This causes too many cells. The cells might form a mass called a tumor. The cells can invade and destroy healthy body tissue. In time, the cells can break away and spread to other parts of the body. When cancer spreads, it's called metastatic cancer.

Risk factors

Factors that may increase the risk of colon cancer include: older age, inflammatory bowel diseases, family history of colon cancer, low-fiber, high-fat diet, not exercising regularly, diabetes, obesity, smoking, drinking alcohol, and radiation therapy for cancer [28].

Prevention

Screening for colon cancer

It is recommended that people with an average risk of colon cancer consider starting colon cancer screening around age 45. But people with an increased risk should think about starting screening sooner. People with an increased risk include those with a family history of colon cancer.

There are several different tests that are used for colon cancer screening. Talk about your options with your health care team.

Lifestyle changes to reduce the risk of colon cancer

Making changes in everyday life can reduce the risk of colon cancer. For example: eat a variety of fruits, vegetables, and whole grains, drink alcohol in moderation, if at all, stop smoking, exercise most days of the week, and maintain a healthy weight, among others.

2.2 Nanomaterials

Nanomaterials are materials with at least one dimension in the 'nano' scale, which is a billionth part (10⁻⁹) of a unit. Within this range, materials present unique properties that significantly differ from those presented at an atomic level and those found in bulk materials. The properties of nanoparticles depend on their material, size, geometry, and even the medium in which they are dispersed. Based on the degree of spatial confinement, nanomaterials can be subdivided into four major types: (a) zero-dimensional nanomaterials (0D), all the dimensions are in nanometer scale, e.g., nanoparticles, (b) one-dimensional (1D) nanomaterials, any one of the three dimensions is of nanometer scale e.g., nanorods, nanowires, (c) two-dimensional (2D) nanomaterials, any two of the three dimensions are of nanometer scale e.g., nanosheets, nanoplates, and nano-coatings and (d) three-dimension (3D) nanomaterials, their three dimensions are larger than 100 nm and electrons are not confined in any direction [29].

Metallic nanoparticles (NPs) are widely used in different areas, such as electronics, optics, catalysis, industry, and some biomedical applications, including drug delivery, diagnosis, therapy, or the latter combination known as theragnosis [30–35]. These particles are also known as inorganic NPs due to their composition based on gold, silver, copper, iron, nickel, or cobalt, to mention a few [36,37]. For example, noble metal NPs present surface plasmon resonances with absorption in the visible and

infrared regions. This makes them suitable as sensing materials by controlling their optical properties, such as absorption or scattering, which depend on the particle size, morphology, and composition [38]. On the other hand, metallic NPs can also be used as contrast agents, typically containing paramagnetic ions that influence the nuclear magnetic resonance (NMR) of water protons in magnetic resonance imaging (MRI) [39–43].

Besides detection, metallic NPs can be used in treatments, often modifying them by adding other metals, biological molecules, or carbon-based substances [44]. For example, in 2008, Liu et al. [45] used graphene as a nanocarrier, and since then, it has been used in diverse biomedical applications. Another technique consists of doping noble metals such as gold or silver to facilitate and deliver drugs precisely [46–49] or use them directly as the treatment agents in photothermal therapy (PTT), an increment in temperature after absorbing light at a resonant frequency [50–53]. This heating has been recently used to treat cancer because it can be well localized, avoiding damaging healthy cells nearby, and it can be done in different ways: optical heating by lasers, heating microbubbles with ultrasound, or exposing magnetic NPs to an alternating magnetic field (AMF) known as magnetic hyperthermia (MHT) [54–57].

2.3 Magnetic hyperthermia

Thermal therapy, also known as thermotherapy, is based on the transfer of thermal energy into or out of the body. The primary goal of this therapy is to achieve a successful treatment outcome while minimizing damage to healthy tissue. Depending on the power and thermal energy applied to the tissue, it can reach a certain temperature with different effects (Table 2.1) [58].

HT works in a range between 40 and 46 °C, temperatures at which cancer cells are vulnerable due to their pathological vascularization [8,13,58]. This therapy can be classified into three main categories: localized, regional, and whole-body hyperthermia. Depending on where the tumor is located, HT can also be classified based on the energy source used to apply heat, such as microwaves, radio frequency, and ultrasound [14,18,22,59].

Table 2.1. Temperature effect on Biological Tissues.

Temperature (°C)	Time requirements	Physical effects	Biological effects	Biological effects	
30 -39	No time limit	None	Growth		

40 – 46	30 – 60 min	Change in optical properties	Increased perfusion, thermotolerance induction, hyperthermic killing
47 – 50	> 10 min	Necrosis, coagulation	Protein denaturation, not subtle effects
> 50	> ~ 2 min	Necrosis, coagulation	Cell death
60 – 140	Seconds	Coagulation, ablation	Protein denaturation, membrane rupture, cell shrinkage
100 - 300	Seconds	Vaporization	Cell shrinkage and extracellular steam vacuole
> 300	Milliseconds	Carbonization, smoke generation	Carbonization

MHT was first used in 1957 by Gilchrist et al. [60], using magnetic particles as heating sources when exposed to a radio frequency field (RF). Three effects generated the material heating:

- Dielectric loss occurs in poorly conductive materials when exposed to an electromagnetic (EM) field
- Eddy's current loss for conductive materials in an EM field
- Hysteresis acts as a magnetic friction

This work served as a foundational step in utilizing magnetic particles, which have greatly advanced with the development of nanotechnology to produce as a foundational step in utilizing magnetic particles, which have greatly advanced with the development of nanotechnology to produce MNPs [61,62].

MNPs have been synthesized in different sizes and morphologies. These kinds of particles can be classified into two main categories depending on their structure: magnetic alloy nanoparticles and magnetic metal oxide nanoparticles [8]; nevertheless, in the latter group, iron oxide nanoparticles (magnetite Fe_3O_4 and maghemite γ - Fe_2O_3) are more suitable for biomedical applications due to their low-cost production, physical and chemical stability, biocompatibility and biodegradability, besides they can be designed to accomplish certain tasks [63,64].

However, despite these advantages, MHT clinical use is limited by the magnetic field strength (H) and frequency (f) applied. Due to AMF limitations, the thermal conversion efficiency relies on the MNPs, so controlling their crystalline structure, shape, and monodisperse size range is indispensable when synthesizing them [8,61,65–72]. There are several protocols for synthesizing MNPs, which can be categorized into two major routes: aqueous and non-aqueous. The first approach is convenient due to its relatively low cost and sustainability; however, obtaining water-soluble, monodisperse MNPs that exhibit excellent magnetic properties remains

challenging. On the other hand, most non-aqueous routes generate MNPs that can only be dissolved in nonpolar solvents [8,61,64]. Some of the most common synthesis routes and their characteristics are presented in Table 2.2 [64].

Table 2.2. Summary comparison of MNPs synthetic methods.

Method	Reaction temp. (°C)	Reaction time	Size distribution	Shape control
Co-precipitation	20 - 150	Minutes	Relatively narrow	Not good
Thermal decomposition	100 – 350	Hours-days	Very narrow	Very good
Hydro or solvothermal	150 – 220	Hours-days	Very narrow	Very good
Sol-gel and polyol	25 - 200	Hours	Narrow	Good

When MNPs are below ~70 nm, they present superparamagnetic behavior, meaning that thermal energy within them is enough to change their magnetization (Figure 2.5) spontaneously. This means that they have no net magnetic moment at room temperature in the absence of a magnetic field. In the presence of a magnetic field, net magnetization originates from the alignment of the magnetic moments with the field; however, this effect does not persist when the field is removed. This lack of remanent magnetization is required for biomedical applications. This phenomenon can be observed in the hysteresis curve (Figure 2.6); when the applied magnetic field (H) is absent, the remnant magnetization (M_R) is zero. Then, when H is increased, the dipoles within the material start aligning with the field, and the magnetization increases. M reaches its maximum value at the saturation magnetization (M_S) and cannot increase beyond this with increasing H. The absolute value of H at which M becomes zero is called the coercivity (Hc) or the residual magnetism of the material [57,73]. The performance of nanoparticles can be enhanced by functionalization with suitable materials [57,74], either organic or inorganic compounds [75]. Nanoparticles' functionalization determines properties such as wettability, stability, biochemical affinity, loading capacity, cell adhesion, intracellular delivery, toxicity, and therapeutic performance [8,64].

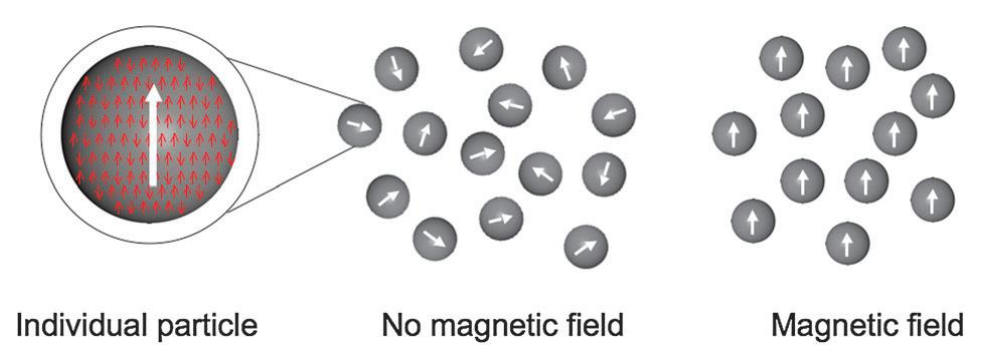


Figure 2.5. Schematic representation of superparamagnetic particles. The orientation of their magnetic moments is randomly aligned in the absence of an external magnetic field; they only get aligned in the presence of an external magnetic field and return to their unaligned orientation after removing the external magnetic field.

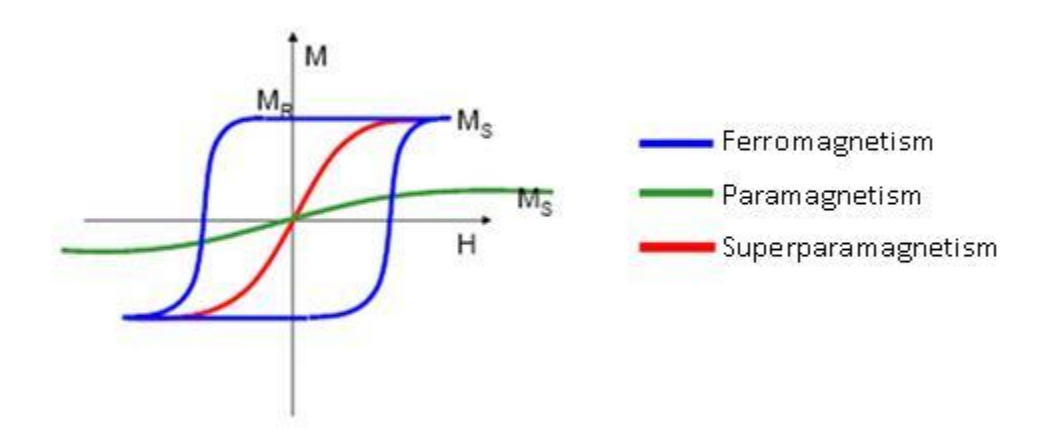


Figure 2.6. Hysteresis loop of magnetic materials showing the magnetization (M) as a function of an applied magnetic field (H). The loop demonstrates that the material's magnetization lags behind the applied field.

2.4 Synthesis methods of MNPs

Coprecipitation

Coprecipitation is the most common method and was first reported by Massar. It consists of mixing ferric and ferrous ions at a 1:2 ratio in a room or at an elevated temperature in the presence of a base. The nucleation of Fe₃O₄ occurs quickly when the solution pH is below 11, while growing Fe₃O₄ particles is easier when the pH is above 11 [64,75,76]. It has been widely used since then for its numerous advantages, such as its simplicity and high-scale production, besides the particle tuning by changing the reaction temperature [77].

Different surfactants and biomolecules have been introduced to avoid aggregation and biocompatibility problems. For example, Salavati-Niasari et al. [76] added

octanoic acid as a surfactant, obtaining 25 nm monodisperse particles. Adding surfactants directly during synthesis enables multiple surface functionalities for subsequent coatings.

However, the coprecipitation method's control over particle size, morphology, and composition remains limited. NPs properties are highly dependent on experimental parameters, such as the nature of the iron salts, the Fe(II) / Fe(III) ratio, pH, and the ionic strength of the medium. For example, in the presence of NaOH, Pereira et al. improved some particles' properties by using alkanolamines as their alkaline agent instead of regular bases [78].

Thermal decomposition

This synthesis route can be divided into two strategies: hot-injection approaches, where the precursor is injected into a hot reaction mixture, and conventional reactions, where the mixture is prepared at room temperature and then heated. Contrary to the polydispersity and amorphous MNPs obtained by co-precipitation, this route offers the possibility of obtaining a narrow-size particle distribution and highly crystalline particles [64].

Thermal decomposition involves forming metal oxides by exposing organometallic precursors to high temperatures (100-350°C) and adding organic molecules as stabilizers. These molecules can slow down the nucleation process, affecting the adsorption of additives on the nuclei and their subsequent growth, thereby allowing smaller MNPs to form. Sun and Zeng [79] synthesized monodisperse MNPs from 3 to 20 nm by using Tris(acetylacetonate) iron (III) (Fe(acac)₃) in phenyl ether with alcohol, oleic acid, and oleylamine by a seed-mediated growth method and then dispersed the particles in nonpolar solvents. Using cupferron Fe(Cup)3 as a single precursor, it produces monodispersed maghemite (y-Fe₂O₃) NPs [80], which can also be synthesized by changing the precursor to Fe(CO)₅ in the presence of residual oxygen of the system and by consecutive aeration [81]. Hyeon et al. [82] also prepared highly crystalline and monodisperse y-Fe₂O₃ NPs by the aging of the iron-oleic acid metal complex from iron pentacarbonyl (Fe(CO)₅) in the presence of oleic acid. This synthesis route is commonly used to prepare MNPs with different shapes, such as nanocubes or nanospheres, using different precursors, additives, and solvents during the process. Nonetheless, this method has many advantages in controlling size distribution and morphology. However, MNPs can only be dissolved in nonpolar solvents and require post-functionalization to be transferred to water.

Hydrothermal synthesis

The hydrothermal route involves various wet-chemical technologies for crystallizing substances in a sealed container from a high-temperature aqueous solution and elevated pressure, at 130-250 °C and 0.3 to 4 MPa, respectively. This method can be divided according to whether or not to use specific surfactants, and it is suitable for the growth of MNPs while maintaining control over their composition [64,75].

Hydrothermal and solvothermal synthesis routes have been developed to prepare MNPs with controllable size and shape [83–85]. For example, Ma et al. developed a facile template-free synthetic route to fabricate various hematite (α-Fe₂O₃) nanostructures by modifying synthesis parameters such as reaction time and solvent [86]. This method has also been combined with co-precipitation to prepare monodisperse magnetite MNPs at 70 °C from ferrous and ferric ions by an N(CH₃)₄OH solution, followed by hydrothermal treatment at 250 °C [87].

Despite presenting advantages over thermal decomposition while obtaining a similar size distribution and shape control, MNPs synthesized by this route are commonly easily oxidized in contact with air.

2.5 Biofunctionalization of MNPs

MNPS should show extremely low toxicity when interacting with biological systems. However, this does not always happen; for this reason, nanoparticles usually need to be functionalized or even bioconjugated before they can interact with living organisms (i.e., cells) in a desirable and controllable manner to reduce their side effects.

Besides biocompatibility, additional advantages are obtained after functionalizing the nanoparticles. Some of them have major resistance to oxidation, better colloidal stability, and the ability to bind to desired biomolecules on cells known as targets [88]. Among the most commonly used coating materials are biomolecules, including proteins, DNA, carbohydrates, lipids, and peptides, as well as nanomaterials such as quantum dots, carbon nanotubes, metal nanoparticles, and polymers. Table 2.3 shows some advantages of coated MNPs.

Table 2.3. Advantages of coating MNPs.

Improving physical and chemical properties of MNPs.

Become biocompatible and exhibit low toxicity.

Improves colloidal stability, dispersity, blood circulation enhancement, and specific targeting

More resistant to oxidation.

Appropriate surface functionalization for protein absorption.

Prevention of opsonization of MNPs by the reticuloendothelial system for faster blood clearance.

The synthesis routes utilized to prepare MNPs are fundamental for fabricating monodisperse and superparamagnetic nanoparticles, which could later be functionalized for different applications. Despite several synthesis techniques, obtaining materials with suitable physical and chemical properties for safe application in biological systems with minimal collateral effects remains challenging.

Magnetic hyperthermia can be significantly enhanced by combining it with specific-targeting ligands, luminescent molecules, and chemotherapeutic drugs, thereby acting as a multifunctional material that facilitates diagnosis, drug delivery, and efficient therapy.

MNPs bioconjugation

Bioconjugation refers to a group of chemical techniques used to ligate two molecules, one of which is usually a biomolecule, as mentioned previously, thereby combining the properties and characteristics of both starting materials in the final structure (Figure 2.7) [89].

The bioconjugation of MNPs with peptides such as Arginylglycylaspartic acid (RGD) can take advantage of the overexpression of cellular receptors on the membrane surface that also allow molecular internalization by different mechanisms, such as binding to membrane integrins [90].

Integrins are membrane proteins that play important roles in pathological and developmental processes. This family consists of 24 $\alpha\beta$ heterodimeric members that are responsible for binding cells to the extracellular matrix (ECM), in addition to participating in specialized cell-cell interactions. The α subunit is composed of a β helix with seven blades, which is connected to a thigh, a calf-1 and calf-2 domain, forming the structure of the leg supporting the integrin head (Fig. 2.8). A subset of integrins recognizes the arginylglycilaspartic acid (RGD) sequence in native ligands. In some ECM molecules, such as collagen and specific laminin isoforms, the RGD sequences are exposed during denaturation or proteolytic cleavage, allowing cells to bind to these ligands through RGD-binding receptors [91].

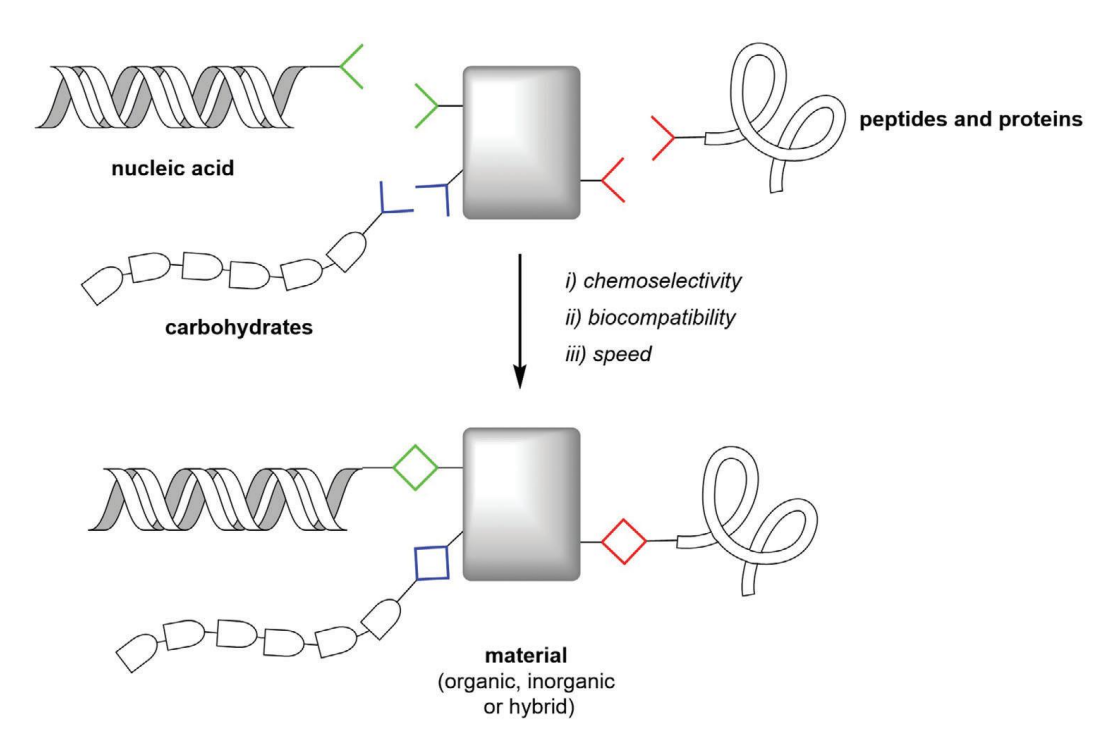


Figure 2.7. Schematic illustration of biofunctionalization of materials by bioconjugation. This diagram shows how different biomolecules, such as nucleic acids, carbohydrates, peptides, and proteins, can be attached to nanoparticles to perform a required task or enhance a particle's property.

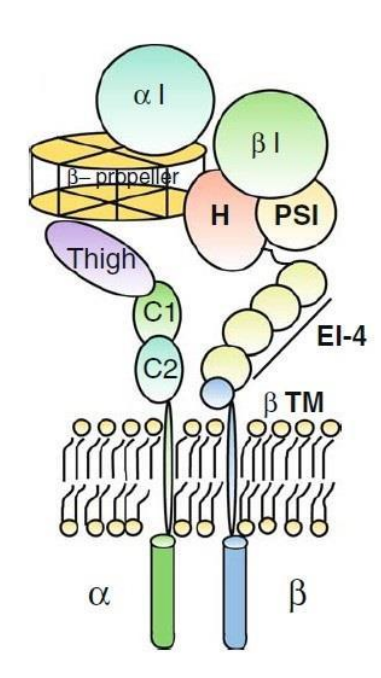


Figure 2.8. Representation of the domains in an integrin. These proteins are formed through noncovalent association of two type I transmembrane glycoproteins, the α - and the β subunits.

2.6 Magnetization in the application of hyperthermia

Types of magnetism

Magnetism originates from the orbital and spin movements of electrons, and its strength depends on the intensity of interaction between them. In some materials, the interactions of atomic magnetic moments are not collective, and the interactions of the other atomic materials are sufficiently strong, leading to a significant distinction between all magnetic materials. Because of this, materials are mainly classified into five categories according to their response to AMF: diamagnetic (DM), paramagnetic (PM), ferromagnetic (FOM), ferrimagnetic (FIM), antiferromagnetic (AFM), and Superparamagnetic [92,93].

Ferromagnetism

It is an inherent property that makes some materials naturally magnetic. FOM materials are attracted to magnets in the presence of an AMF, which is insignificant because this property makes them capable of attracting other FOM materials. Transition metals (Fe, Ni, Co) and their alloys are commonly FOM materials at room temperature or even higher; their atomic magnetic moments tend to be parallel. In general, FOM materials can be classified according to their coercivity (Hc) as soft (low Hc) and hard (high Hc). This classification implies that the hard group exhibits a broader hysteresis cycle, requiring more energy for magnetization. These materials have two distinct characteristics. The first is the net (spontaneous) magnetization attributed to the internal molecular field, even after removing the AMF. The second refers to the temperature-dependent magnetic order [93]. These characteristics indicate that FOM materials retain magnetic properties even without an AMF. The positive energy moment indicates that FOM materials show a high positive susceptibility and magnetic permeability [9].

Below the Curie temperature (T_C), long-range FOM magnetic moments are aligned in one direction, reducing the energy of material exchange. Above the T_C , the FOM properties disappear, and the PM properties replace them, and consequently, the magnetic moments become disordered. Thanks to these remarkable characteristics of the FOM on the nanoscale, a monodomain can achieve the desirable magnetism known as superparamagnetism [94,95], which is an essential requirement for magnetic hyperthermia. It has been observed that graphene oxide can transform from ferromagnetism to superparamagnetism if the magnetic domain of graphene oxide FOM is decreased through the removal of functional groups [96]. Therefore, FOM materials may be promising thermal agents for magnetic hyperthermia.

Ferrimagnetism

This state of magnetism can be observed in compounds with more complex structures, but not in pure elements. Some Fe oxides combine with at least one transition metal, such as Mn, Ni, or Zn, to produce FIM materials whose magnetic

properties depend on electronic interactions related to metal ions. Ferrimagnetism states, such as ferromagnetism, occur when the magnetic moments of a material spontaneously align under the T_C to produce net magnetization. In the absence of a magnetic field, the FIM network consists of two distinct subnets with varying forces. The magnetic moments of these subnets are randomly oriented with unequal magnitudes and anti-parallel alignments, implying that the magnetic moments in one direction are stronger than those in the opposite direction, which generates net magnetization. Therefore, the FIM magnetic behavior, like FOM, involves net magnetization, T_C , and hysteresis, but these vary depending on the magnetic arrangement. FIM materials show the FOM properties below the T_C but follow the PM behavior above the T_C . Both FIM and FOM show superparamagnetic behavior above the blocking temperature (T_B) [97]. This indicates that nanomaterials with this type of magnetism demonstrate the FOM capabilities that can be achieved in magnetic hyperthermia.

Superparamagnetism

It is a type of magnetism that occurs in very small FIM or FOM particles, in the range of a few nanometers to a couple of tenths of nanometers. The aligned spin orientations of large particles are arranged in domains; therefore, these domain walls (multidomain) are present in most materials and require relatively little energy to move them. However, in smaller particles (~2 - 20 nm), the number of domain walls per particle decreases to one wall (monodomain), where superparamagnetism (SPM) is observed due to the lack of limits and minimum energy.

Nanoparticles with SPM make sense if the temperature is below the T_{C} , because their properties depend on the net magnetic moment. The NPs with SPM are aligned in a preferred arrangement, thereby achieving magnetization faster than other states. At the same time, each atomic magnetic motion retains its ordered state, leading to a non-hysteresis curve with zero Hc and residual magnetization (Mr) [98]. Unlike FOM NPs, SPM NPs ignore maintaining net magnetization when removing AMF, indicating that these materials do not show magnetic memory or magnetic hysteresis on the B-H curve. In addition, NP SPM usually shows two different magnetic structures: a nucleus of magnetic particles (generally iron oxides), which may be coated with organic materials or precipitated within a porous biocompatible polymer [99]. Therefore, biocompatible SPM NPs are considered the optimal candidate for magnetic HT, compared with other NPs with different magnetism states.

Magnetic properties

Owing to their magnetic properties, MNPs can react to external magnetic fields. SPM allows MNPs to be manipulated with an external field. The size of these particles has a significant impact on their physical characteristics. Quantum effects become increasingly noticeable as the particle size drops within the nanoscale,

producing unique phenomena like improved surface-to-volume ratio and size-dependent magnetic behavior [100].

Magnetic saturation (Ms)

The maximum magnetization of FOM and FIM materials can be obtained at Tb < Tc when exposed to a strong AMF. Ms is considered a function of temperature, Ms(T), since, by increasing the magnitude of the AMF, no further increase in the stabilized magnetization occurs. The crystal size of MNPs negatively affects Ms by reducing it. When the particle size of MNPs is reduced below the transition point (from multidomain to monodomain), they become suitable for biomedical applications. In such a magnetic state, the magnitude of Ms decreases due to the increased effect of spin disorder on the surface of MNPs. Therefore, the magnitude of the Ms is directly proportional to the size of the MNPs. Ms is a substantial factor in hyperthermia for two reasons: First, MNPs with a high Ms result in a high SAR value, indicating that the MNPs have a great heating power to destroy cancer cells; secondly, the high Ms makes the movements of MNPs more controllable in the bloodstream by using an AMF to keep them around tumor cells [101].

Curie temperature (Tc)

It is a defined transition of FOM materials at which ferromagnetism disappears, and the material becomes PM. This transition temperature is called "Curie temperature" or "Curie point." Many materials lose all their magnetism after being heated above this point and then cooled. Some can return to a permanent magnet by placing them in a strong magnetic field. Others require heat treatment in a strong magnetic field. Below the T_C, the FOM material is ordered, and above it, it is cluttered. Saturation magnetization reaches zero at the Curie temperature.

Coercivity (Hc)

It is the force required to return a FOM material to zero magnetization after being stimulated with an AMF. This goes in the opposite direction to the applied field and is where the flow density also decreases to zero. This process leads to a cycle known as hysteresis. This cycle represents the correlation between the magnetic field and the induced flux density, also known as a magnetization curve (B-H curve) (Figure 2.9).

Residual magnetization (Mr)

It is a type of magnetization that remains in the FOM and FIM materials when the AMF is removed. MNPs are magnetically saturated once AMF is removed. FOM NPs use an auxiliary magnetic field to resist sudden change and maintain their magnetization; however, SPM NPs possess large magnetic moments and behave as PM NPs, for instance, to demagnetize with insignificant Hc and Mr.

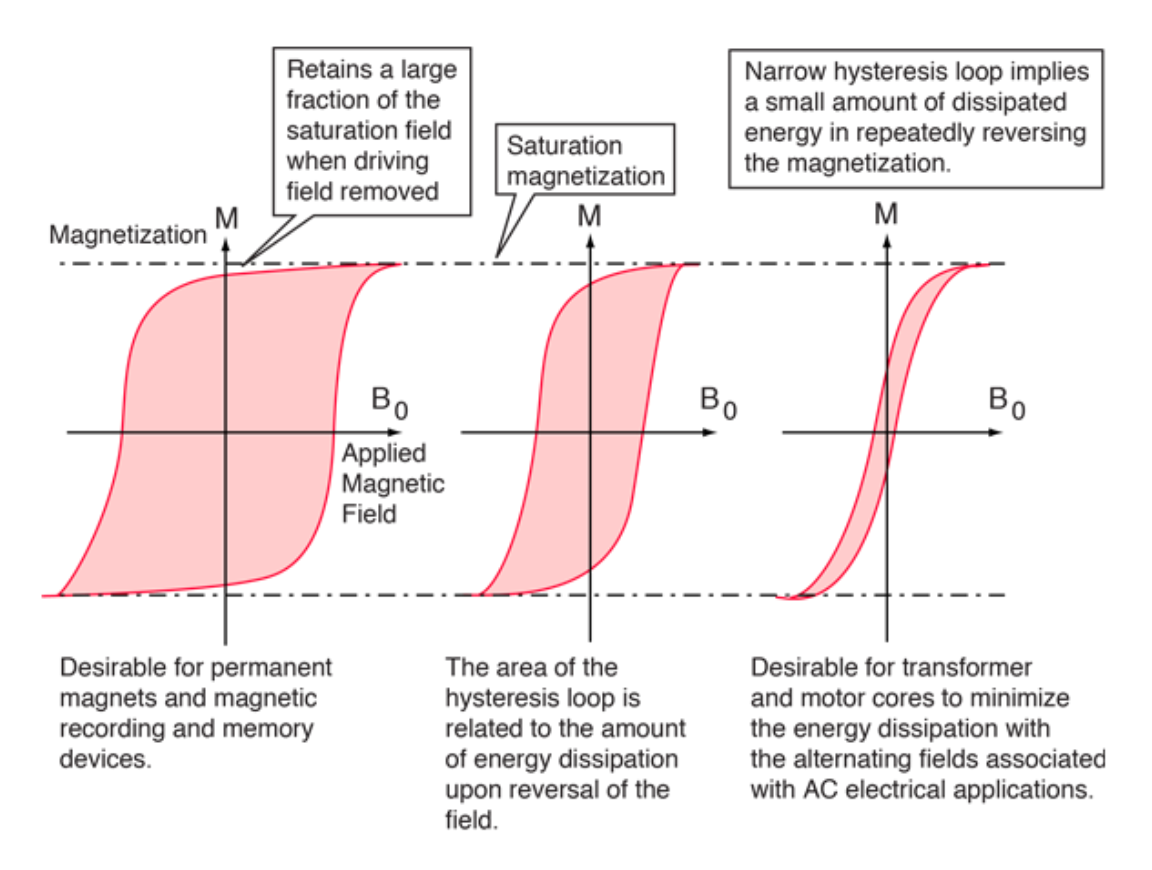


Figure 2.9. Hysteresis curves of various types of magnetic materials. The magnetization, M, lags behind the applied field, B0, and traces out a characteristic curve known as the hysteresis loop. The applied field strength at which the magnetization reverses is called the coercive field. The width of the hysteresis loop indicates the hardness of the magnetic material.

2.7 Characterization techniques for MNPs

Scanning electron microscopy (SEM)

Electron microscopy consists of the interaction between electrons and matter. These types of microscopes use a high-energy electron beam that interacts with a material. From this interaction, information can be obtained from the sample, such as topology, morphology, chemical composition, and crystallographic structure. These microscopes are capable of examining features on the nanoscale and are the most widely used characterization instruments in nanotechnology.

Electron microscopes work similarly to optical microscopes, both having a light source and magnifying lenses. Here, the source of illumination is a high-energy electron beam. These microscopes have a significantly higher resolution than optical ones, due to the interaction of the matter wave of an electron with the sample. According to Bragg's law, the minimum separation, d, which can be solved with any microscope, is given by:

$$d = \frac{\lambda}{2\sin\theta} \,. \tag{1}$$

Resolution can be improved by using shorter wavelengths. The wavelength associated with an electron is given by the De Broglie relation:

$$\lambda = \frac{h}{p} = \frac{h}{\sqrt{2 \text{meEk}}} , \qquad (2)$$

where me is the mass of the electron, Ek is its kinetic energy, and h is the Planck constant. The electrons in the microscope obtain their kinetic energy from an applied electric potential of the order of kilovolts or even megavolts. Depending on the kinetic energy, a typical wavelength range may be between 1 - 0.005 Å

The incident electron beam causes secondary electrons to be emitted from the surface, which can be controlled to produce a topological and morphological image at a nanoscale. In the scanning electron microscope, this electron beam is emitted from a heated filament, which is commonly made of lanthanum hexaboride (LaB6) or tungsten. The filament is heated by applying a voltage that causes electrons to be emitted [102].

X-ray diffraction (XRD)

XRD is used to study the crystal structure of solids. In this technique, an X-ray beam with a wavelength of between 0.07 and 0.02 nm is diffracted by the crystalline sample according to the Bragg law:

$$\lambda = 2 d \sin \theta, \tag{3}$$

where d is the interplanar distance and λ is the wavelength of the X-rays. The intensity of the diffracted beam is measured as a function of the angle of diffraction (20) and the orientation of the sample (Figure 2.10). The diffraction pattern can be used to identify crystalline phases and their structural characteristics.

Homogeneity and heterogeneity in materials can be measured as X-ray intensities and depend on the Bragg angle. The homogeneous or uniform elastic deformation displaces the positions of the diffraction peaks, without changing their profile. A change in the positions of the X-ray peaks indicates a change in spacing d caused by a change in the crystal lattice constants. Heterogeneous deformations vary from crystallite to crystallite or even within a single crystallite. Since XRD provides the average of the total volume of crystallites, there is an increase in the diffraction peaks, which increases with the increase in sin θ . The increase in the peaks may also be due to the fine size of the crystallite, which is independent of the sen θ . The contribution of crystallite size and crystal lattice deformation can be determined independently by peak profile analysis.

POWDER X-RAY DIFFRACTION GEOMETRY

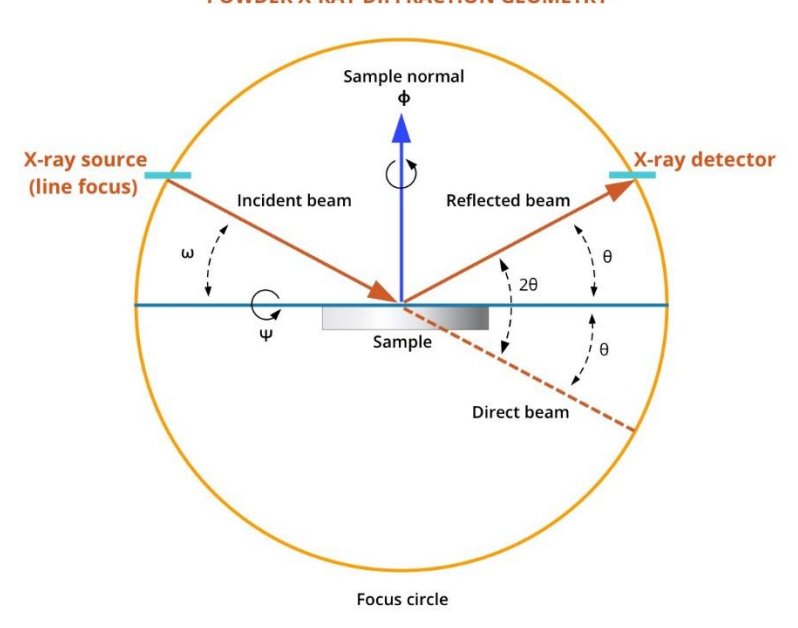


Figure 2.10. Geometry of X-ray diffractometer. In this configuration, an X-ray source with a line focus emits a divergent incident beam that strikes a flat powder sample. The sample is positioned such that its surface is tangent to the focusing circle. X-rays satisfying Bragg's Law $(n\lambda = 2d \sin\theta)$ for a given set of crystal lattice planes (hkl) are diffracted.

Since no heterogeneous forces are present, the size of the crystallite can be determined. D by Scherrer's formula:

$$D = \frac{K\lambda}{B \cos \theta_B}, \tag{4}$$

where λ is the wavelength of X-rays, B is the maximum width at half the maximum height (FWHM) of a diffraction peak, θ_B is the angle of diffraction, and K is the Scherrer constant, which is of the order of the unit for a spherical crystal. However, nanoparticles often form twin structures, and therefore, the Scherrer formula may not always give true particle sizes [103].

Infrared Spectroscopy with Fourier Transform (FTIR)

Infrared (IR) spectroscopy is the measurement of absorption of infrared radiation by a material as a function of wavenumber. The resulting graph of absorption versus wave number is called the FTIR spectrum. Infrared spectroscopy provides information mainly due to the vibrational and rotational modes that accompany molecules. Since absorption bands are associated with vibrations of particular

functional groups within the molecule, band identification can result in the identification of the molecules that make up a material.

With Fourier Transform Infrared Spectrometry (FTIR), high-resolution, fast, and reproducible infrared spectra can be obtained in a wide variety of sample types, including bulk gas, liquid, solid, powder, thin films, and nanomaterials. FTIR is used for the identification of organic and inorganic materials, the quantitative determination of species in complex mixtures, the determination of the molecular composition of surface species, the differentiation of structural and geometric isomers, and the determination of molecular orientation in polymers and solutions.

Infrared radiation is electromagnetic radiation in the region of approximately $0.78 \, \mu m$ - $1000 \, \mu m$ wavelength. It is a wavelength longer than the visible range and shorter than a microwave. The IR spectral region for material evaluation by absorption spectroscopy can be divided into near-infrared (NIR), middle infrared (MIR), and far infrared (FIR) [104].

2.8 MHT frequency determination

The frequency of an alternating current (AC) circuit with an inductor is primarily determined by the inductance (L) and the capacitance (C) in the circuit, not by the number of turns directly. The resonant frequency (f) of an LC circuit (inductor and capacitor) is calculated using the formula:

$$f = \frac{1}{2\pi\sqrt{LC}} \tag{5}$$

The inductance itself is affected by the number of turns, and the formula for the inductance of a solenoid is

$$L = \frac{\mu * N^2 * A}{1} \tag{6}$$

where μ is permeability, *N* is the number of turns, *A* is the cross-sectional area, and *I* is the length of the coil as shown in Figure 2.11 [105].

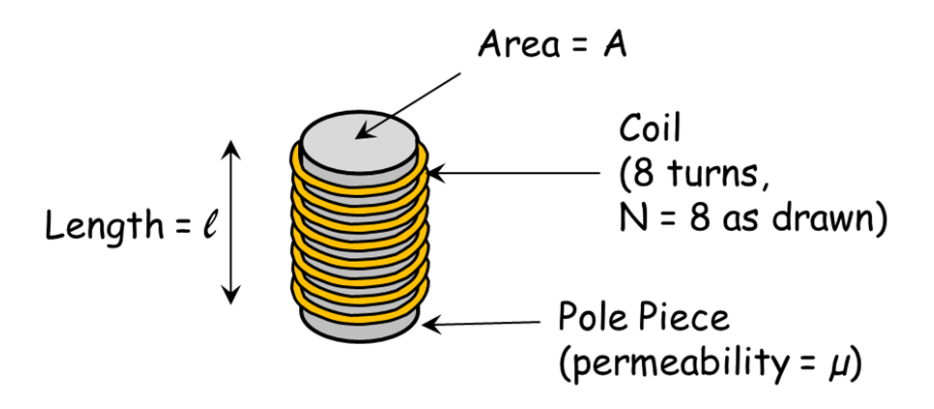


Figure 2.11. Schematic diagram of a solenoid. A coil of N=8 turns is wound around a high-permeability (μ) ferromagnetic core, forming a closed magnetic path with a cross-sectional area A and a mean path length ℓ . The core is constructed with a pole piece to direct the magnetic flux.

CHAPTER 3 SYNTHESIS, CHARACTERIZATION, AND APPLICATIONS OF MAGNETITE (Fe₃O₄) NANOPARTICLES

3. Synthesis, Characterization, and application of magnetite (Fe₃O₄) nanoparticles

Here, it is described the whole process for the preparation and characterization of magnetite (Fe₃O₄) nanoparticles; this section is the first experimental part of two. A couple of synthesis routes, reduction and coprecipitation, were followed to obtain particles capable of performing magnetic hyperthermia treatment, which requires at least three fundamental characteristics that the particles must possess; they need to be monodisperse, biocompatible, and superparamagnetic. To evaluate if the particles have these characteristics, a series of characterizations were carried out, among them, X-ray diffraction, scanning electron microscopy, magnetic hysteresis loop, Fourier transform infrared spectroscopy, and heating tests, among others.

3.1 Introduction

Physical, chemical, and magnetic properties depend mainly on the particles' size, morphology, and composition, with their preparation method, or synthesis route, being fundamental as it determines the size, shape, and composition within the particles and on their surface. Controlling the size or growth of nanoparticles relies on the selected route and the precursors; this property is generally affected by the temperature used, the atmosphere of preparation, and the synthesis time. Meanwhile, the precursor dictates the reaction rate and, hence, the formation of a predetermined number of particles.

To synthesize nanoparticles in different shapes typically requires complex procedures, often involving high temperatures, pressures, or both. In some cases, organic solvents are necessary due to their high boiling points. After this, in most cases, a second step is required to change the nanoparticles from a hydrophobic state to a hydrophilic one, to make them suitable for working with biological systems.

The selection of particles' core and surface is fundamental for applications where the particles are used in biomedical applications, magnetic hyperthermia, and analyte detection.

Here, two syntheses of Fe_3O_4 nanoparticles with similar morphological characteristics, such as shape and size, are described by two distinct methods, coprecipitation and chemical reduction.

3.2 Materials

Ferric chloride hexahydrate (FeCl₃·6H₂O), ferrous chloride tetrahydrate (FeCl₂·4H₂O), iron (II) chloride (FeCl₂) 98 %, octadecylamine (ODA) 90 %, sodium hydroxide (NaOH, 97%), meso-2,3-dimercaptosuccinic acid (DMSA), 1-ethyl-3-(3-dimethylaminopropyl) carbodiimide (EDC), and N-hydroxysuccinimide (NHS), and ethanol (96%) were purchased from Merck; Cyclo(-RGDyK) peptide (\geq 95 %) was

acquired from AnaSpec; sodium acetate 99 %, acetic acid 99.7 %, hydrochloric acid (HCl) 37 %, hydrogen peroxide 30 % and ethylene glycol (EG) 99 %, obtained from Karal S.A. de C.V.; 3,3',5,5' tetramethylbenzidine (TMB) purchased from Thermo Scientific and Milli-Q water was used for the solution preparation and MNPs cleaning.

3.2 MNPs synthesis and bioconjugation

Coprecipitation synthesis route

Fe₃O₄ NPs were synthesized following a previously reported method with slight modifications [106,107]. Two samples were prepared at room temperature, the first one under ambient conditions and the other under nitrogen atmosphere, by the following protocol of synthesis: firstly, 1.387 g of FeCl₂·4H₂O and 2.2 g of FeCl₃·6H₂O were added to 100 ml of Milli-Q water under vigorous mechanical stirring (300 rpm). Then, 25 ml of a NaOH solution (3 M) was added drop-wise to the solution at a rate of 0.1 ml/min. When the addition of NaOH was finished, the colloidal solution continued under agitation for twenty minutes more before adding 75.0 mg of DMSA to the colloid, and the solution remained under mechanical agitation for twenty minutes more (Figure 3.1). Finally, MNPs were washed several times with Milli-Q water to eliminate free molecules or inert impurities by a series of magnetic decantation and centrifugation (15 minutes at 4400 RCF) until the supernatant became transparent.

Reduction synthesis route

Fe₃O₄ MNPs were synthesized by first preparing a 90 ml solution of ODA at 40 mM, using either deionized water or ethylene glycol (EG) as solvent. Each solution was heated at 90 °C under magnetic stirring and purged with nitrogen gas for 3 hours to ensure an inert atmosphere. Simultaneously, a 10 ml solution of FeCl₂ (10 mM) was also being purged with nitrogen. When the FeCl₂ solution was completely purged, it was syringed into the ODA solution and was reduced immediately, as observed by a color change from a white milky consistency to a deep black color. After this, the solution remained under agitation for two more hours at 90 °C for the aqueous system and 150 °C for the EG-based system, then the heating was turned off, and the stirring continued until the solution was cooled to room temperature. Finally, the MNPs were purified by magnetic decantation with water and ethanol several times to remove ODA residues, and then redispersed in water. Figure 3.2 shows the schematic diagram of the synthesis process.

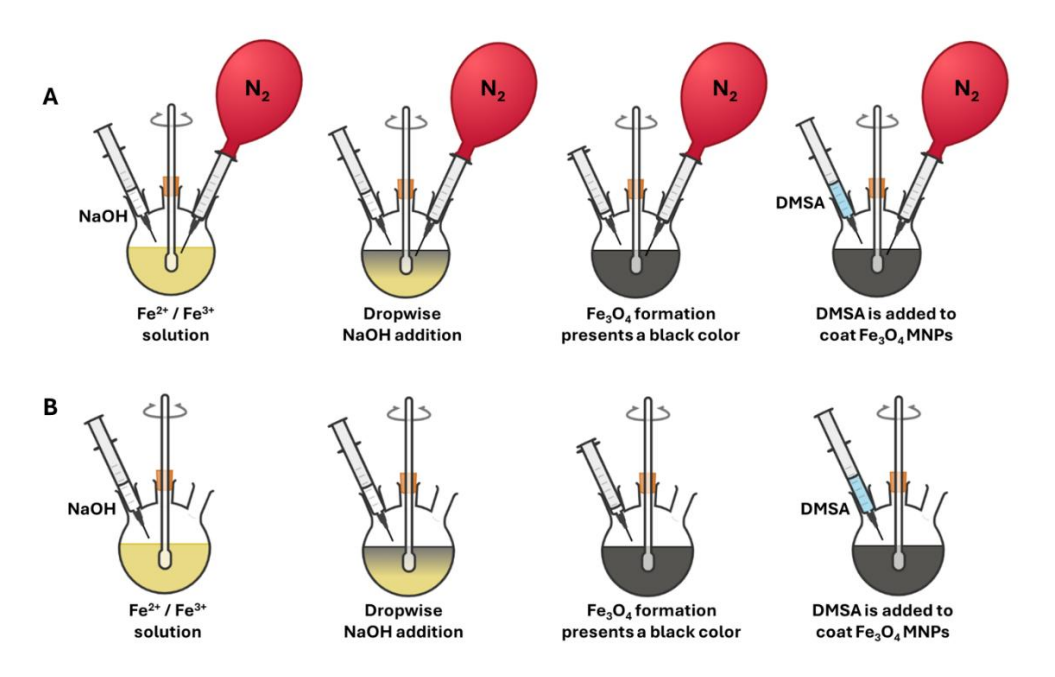


Figure 3.1. Schematic diagram of the MNPs synthesis system by coprecipitation. A concentrated NaOH solution is added dropwise into an Fe^{2+} and Fe^{3+} salt solution to form Fe_3O_4 nanoparticles. They were synthesized A) under a nitrogen atmosphere, and B) under ambient conditions.

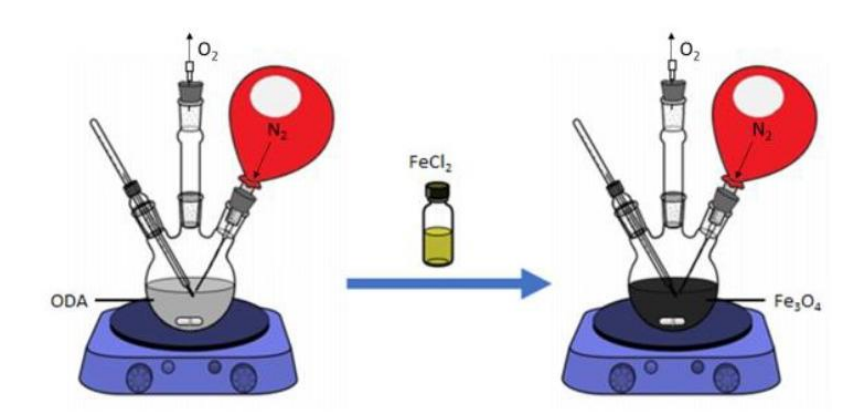


Figure 3.2. Schematic diagram of the MNPs synthesis system by chemical reduction. A solution of FeCl2 is added to an octadecylamine (ODA) solution under a nitrogen atmosphere and almost at the boiling point of its solvent.

Bioconjugation

MNPs coated with DMSA contain carboxylic groups, making them suitable for use in the EDC/NHS crosslinking method. Briefly, 0.2 M solutions of hetero-bifunctional coupling agents EDC and NHS were prepared in MES buffer (pH 4). EDC was used

to activate the carboxylic groups of the MNPs by mixing 1 ml of a 0.2 M solution of EDC with 3 mg of MNPs@DMSA by sonication for 10 minutes, followed by 4 hours of agitation. Then, this MNPs-EDC complex was mixed with the NHS solution and agitated for 16 hours. After this, 1 ml of RGD peptide aqueous solution (2mg/ml) was added and stirred for 24 hours [108,109]. Finally, the RGD-coated MNPs (MNPs@RGD) were washed several times with water by magnetic decantation and stored under refrigeration for future use.

3.3 MNPs characterization

MNPs prepared by coprecipitation under air and nitrogen atmospheres and coated with DMSA were labeled as A-MNPs and N-MNPs, respectively. They were analyzed using several characterization techniques, as well as MNPs synthesized by reduction prepared in EG and water, labeled as EG-MNPs and W-MNPs, respectively.

X-ray diffraction (XRD) patterns were acquired from dried MNPs powder to analyze their crystalline structure with a *Bruker D2 Phaser* diffractometer, using a Scherrer constant k = 0.9, a radiation Cu K α $\lambda = 1.5418$ Å, in a measurement range from 20 to 70°, and a step size of 0.02°/s.

Scanning electron microscopy (SEM) images were acquired using a *JEOL-JSM-7800F* microscope using a power of 15 kV. Image processing and analysis of MNP size dispersion were performed on a series of micrographs using *ImageJ* software.

Additionally, dynamic light scattering (DLS) was employed to estimate the hydrodynamic radius of magnetic nanoparticles prepared by the coprecipitation route, either bare or coated with DMSA, on a *Malvern Zetasizer Nano ZS* using a detection angle of 173°. The average measurements were acquired ten times from the distribution at 25°C. The instrument uses a 4.0 mW He–Ne laser at a wavelength of 633 nm. Intensity and volume correlations were obtained by using the equipment software.

Magnetic properties were evaluated using a vibrating sample magnetometer, *Cryogenic, miniVSM*, ranging from – 2 to + 2 T at temperatures of 2 and 300 K for the particles prepared by coprecipitation, while a LakeShore 7300 vibrating sample magnetometer (VSM), ranging from - 3 to + 3 T at 300 K, was utilized to measure EG-MNPs and W-MNPs.

To determine the best parameters for MNPs heating, AMFs were tested at different frequencies, obtaining that a frequency $f=100\,$ kHz was the most adequate frequency to achieve MHT in N-MNPs, while $f=85\,$ kHz for EG-MNPs. Then, different MNPs concentrations, 100, 250, and 500 µg/ml, were poured into Eppendorf tubes positioned at the center of the coil, where the field intensity was the highest. After turning on the equipment, the temperature was measured each minute by an Infrared

(IR) camera (Fluke, TiS45). These concentrations were chosen to be applied to biological systems without producing toxic effects before the MHT stimulation.

Finally, iron quantification was determined by ultraviolet–visible spectroscopy (UV-Vis). This methodology was previously reported by M. Torras et al. [107]. The method consists of two steps for the sample preparation: first, the addition of a concentrated hydrochloric acid (HCl) solution to digest the sample and, second, the addition of a complexation agent to generate iron complexes that can be detected and quantified by UV-Vis spectroscopy, the spectrum was acquired in 1 cm square quartz cuvettes using a StellarNet spectrometer EPP200 from 200 to 550 nm; each spectrum was the average of three scans.

Fourier Transform Infrared (FTIR) spectra were also collected using dry powder samples to determine the functional groups on the MNPs surface from an *Agilent Technologies Cary 670 FTIR Spectrometer*, ranging from 3600 to 500 cm⁻¹.

3.4 MNPs characterization results

X-ray diffraction (XRD)

XRD patterns (Figure 3.3) show the characteristic diffractograms of magnetite of A-MNPs, N-MNPs, W-MNPs, and EG-MNPs. Here, the positions of the narrow peaks at 30.43, 35.81, 43.46, 53.78, 57.30, and 62.89° (± 0.12°) together with their relative intensities, corroborate the presence of a crystalline cubic spinel structure found in Fe₃O₄ nanoparticles. Both syntheses produced magnetite NPs coated with DMSA or amino groups (NH₂) for coprecipitation and reduction syntheses, respectively.

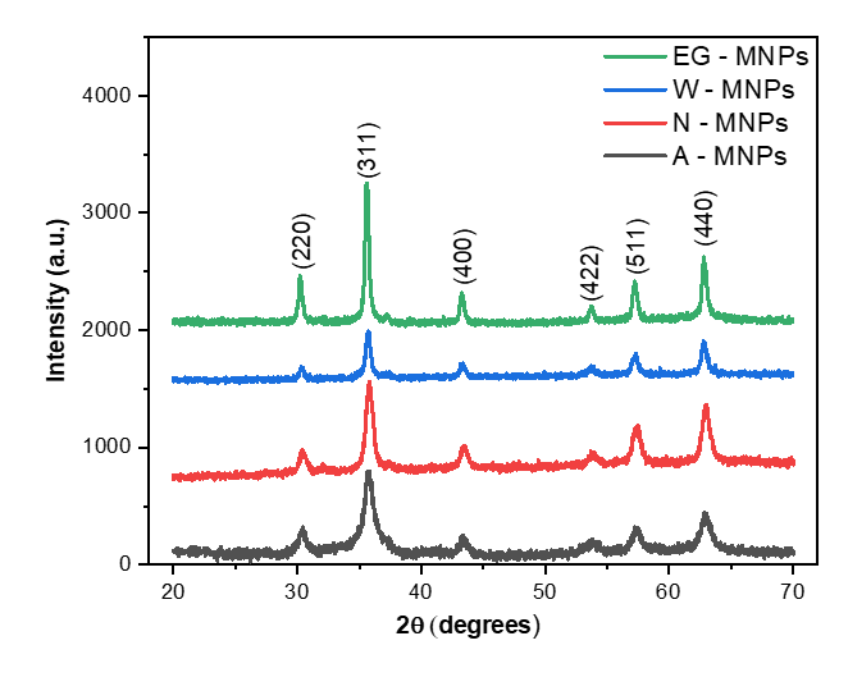


Figure 3.3. X-ray diffraction patterns of MNPs synthesized by coprecipitation under air (black line) and nitrogen atmosphere (red line), and by reduction in water (blue line), and EG (green line). All of the patterns present the characteristic peaks of magnetite at 30.43, 35.81, 43.46, 53.78, 57.30, and 62.89°.

Scanning electron microscopy (SEM)

Morphology and particle size distribution were determined through the analysis of a series of SEM images using the free software ImageJ. The corresponding size distribution histograms are presented in Figure 3.4. The MNPs synthesized by coprecipitation exhibited average diameters of 15.0 ± 3 nm for A-MNPs and 23 ± 5 nm for N-MNPs, with polydispersity indices (PDI = (standard deviation/average)²) of 0.04 and 0.03, respectively. These PDI values are < 0.1, implying monodisperse particle size distributions (Figure 3.4). For MNPs synthesized by reduction, the presented diameters of 35 ± 9 nm and 34 ± 7 nm for W-MNPs and EG-MNPs, respectively (Figure 3.5).

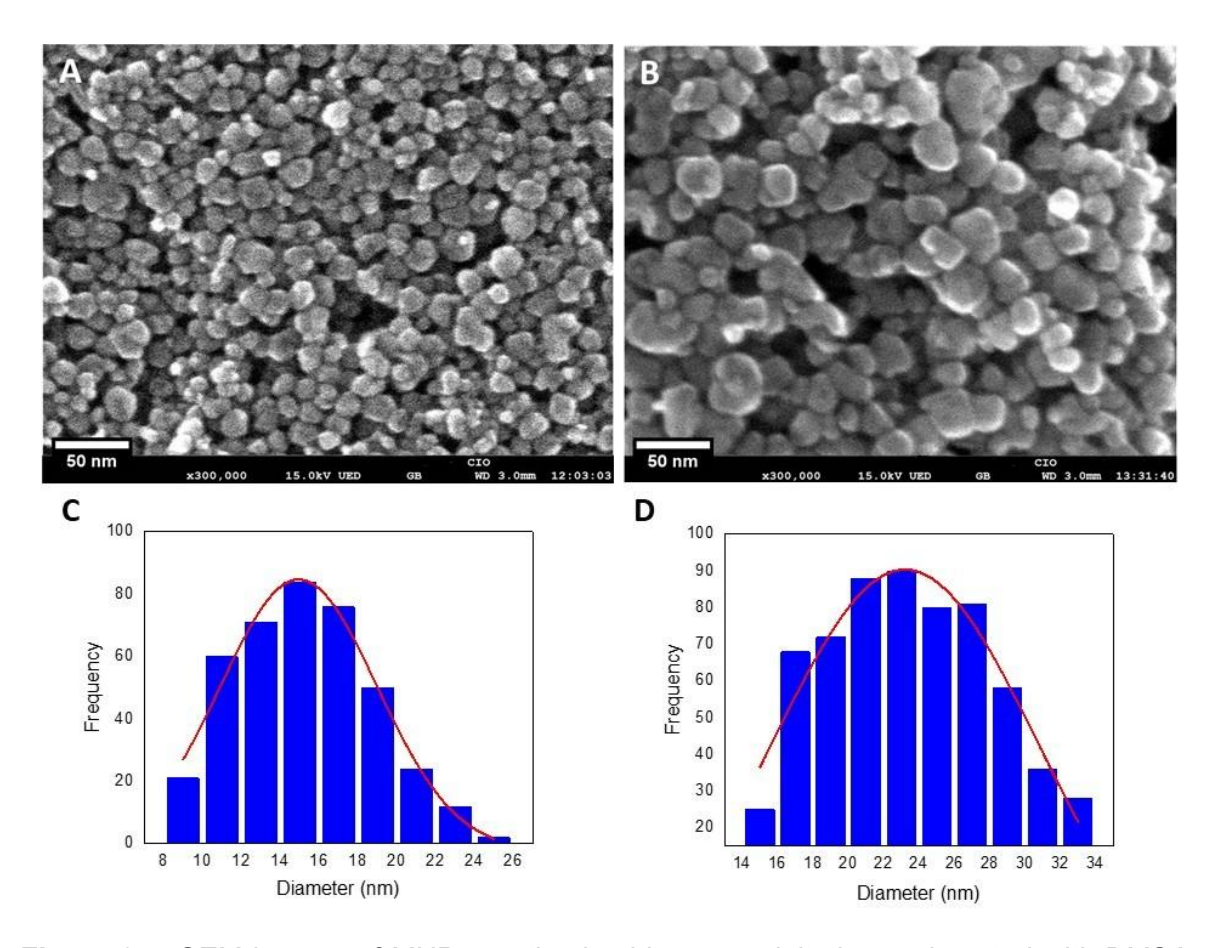


Figure 3.4. SEM images of MNPs synthesized by coprecipitation and coated with DMSA. A) A-MNPs. B) N-MNPs. Size distribution histograms of C) A-MNPs and D) N-MNPs. The average diameters for MNPs synthesized by coprecipitation were 15.0 ± 3 nm and 23 ± 5 nm.

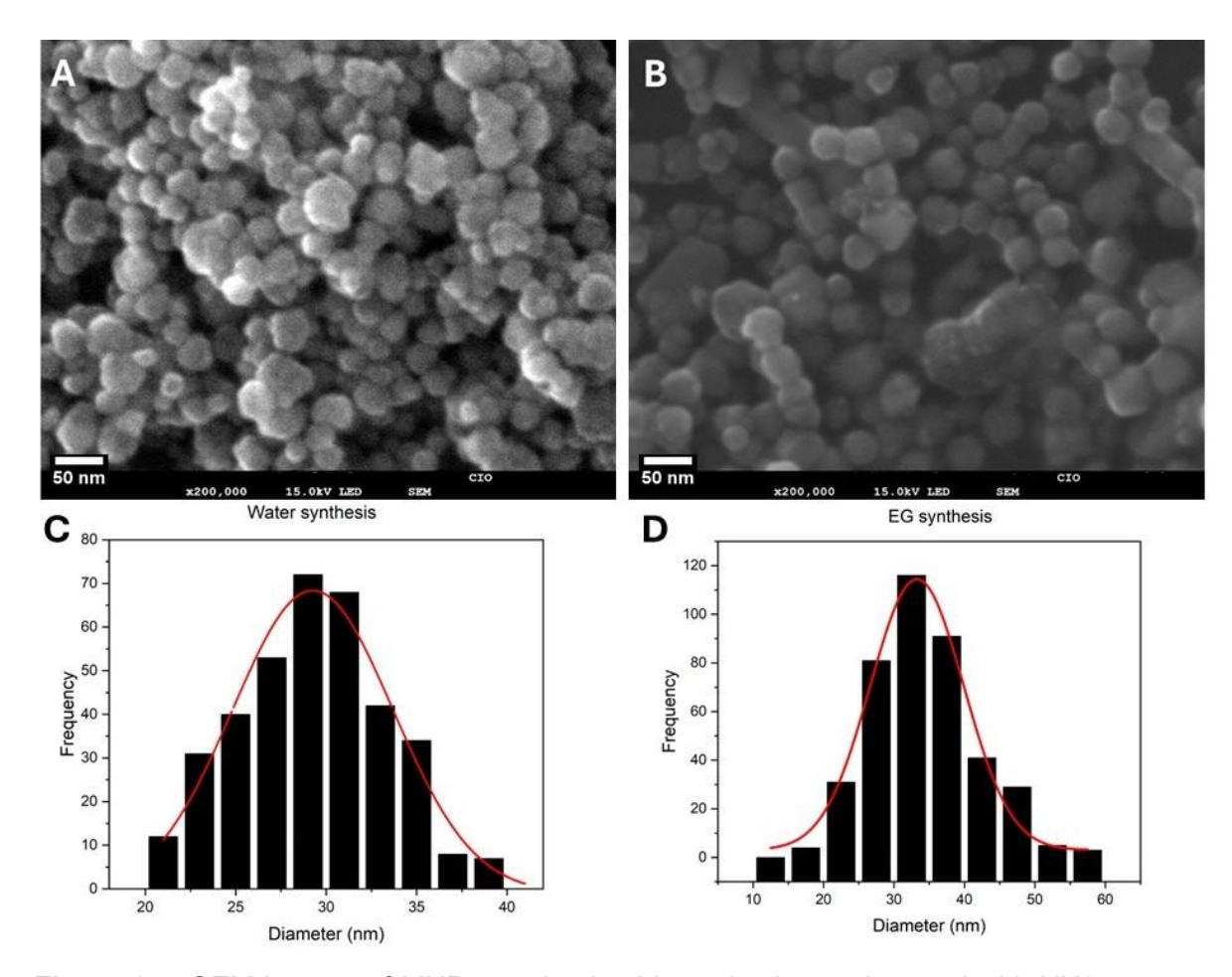


Figure 3.5. SEM images of MNPs synthesized by reduction and coated with NH2 groups. A) W-MNPs and B) EG-MNPs. Size distribution histograms of C) W-MNPs and D) EG-MNPs. The average diameters for MNPs synthesized by reduction were 35 ± 9 nm and 34 ± 7 nm.

Magnetic properties

Figure 3.6 A shows that the hysteresis loops exhibit a very low coercivity, a characteristic behavior of superparamagnetic NPs (from – 10 kOe to 10 kOe). M-H hysteresis loops of sample MNPs were also measured at a temperature of 2 K through the zero-field cooling protocol, and the sample temperature was cooled down from room temperature to the above temperatures in the absence of any applied magnetic field. The saturation magnetization values were determined by extrapolating the M versus 1/H curves to the limit when 1/H approaches zero. Table 3.1 summarizes the corresponding values of coercivity (Hc), saturation magnetization (Ms), and remanence magnetization (MR). Figure 3.6 B and Table 3.1 show the increase in coercivity as the temperature decreases. MNPs exhibit efficient Ms compared with the typical values reported previously (30–50 emu/g) [8,110]. Additionally, it is well known that only MNPs with a smaller size of 15 nm and good

crystallinity exhibit values closer to those of bulk magnetite (86 emu/g) (Figure 3.6). On the other hand, Figure 3.7 shows the hysteresis loop of MNPs synthesized by reduction in water and EG, and their H_C , M_S , and M_R values are presented in Table 3.1.

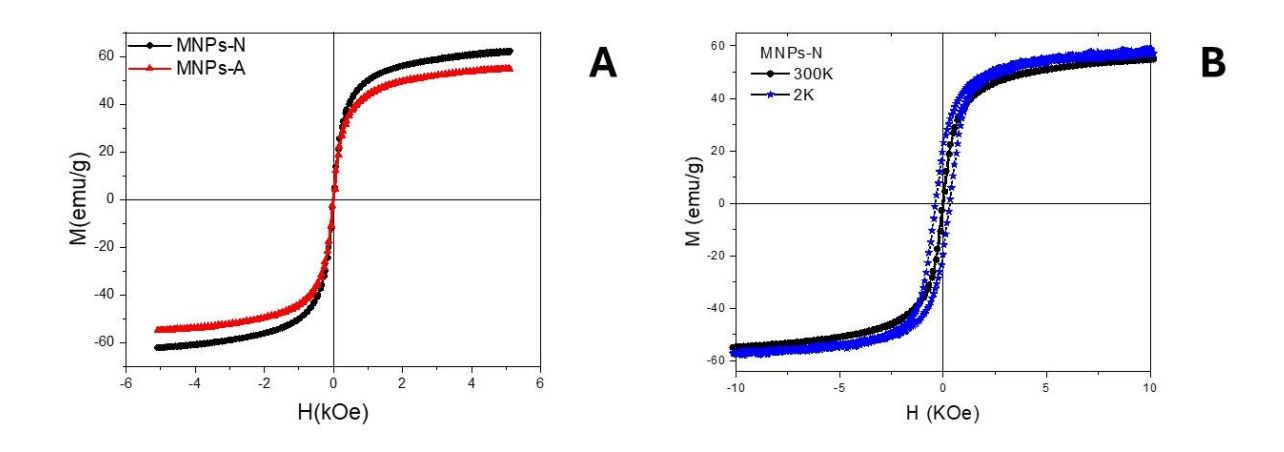


Figure 3.6. Magnetic characterization of MNPs synthesized by coprecipitation. A) M-H hysteresis loops of A-MNPs and N-MNPs measured at 300 K. B) M-H hysteresis loops of N-MNPs measured at 300 and 2 K.

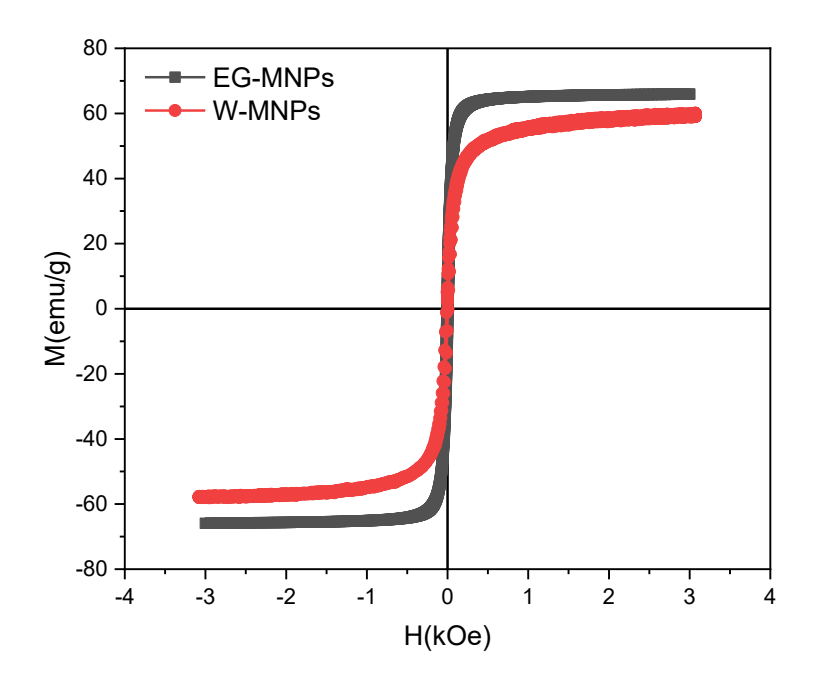


Figure 3.7. Magnetic characterization of MNPs synthesized by reduction, M-H hysteresis loops of EG-MNPs and W-MNPs measured at 300 K from a range from -3 to 3 kOe.

Table 3.1. Magnetic parameters of the M-H hysteresis loops

Sample	Temperature (K)	H _C (Oe)	M _S (emu/g)	M _R (emu/g)
N-MNPs	300	43.0	55.0	3.0
A-MNPs	300	41.0	62.3	3.3
N-MNPs	2	370.0	60.5	22.3
W- MNPs	300	58.0	66.0	7.1
EG- MNPs	300	120.0	60.0	8.4

Coil development

As mentioned in section 2.8, the frequency (f) given by the inductance (L) and capacitance (C) in the circuit depends on the length (I), number of turns (N), and diameter or cross-sectional area (A) of the coil. And are related by the following equations:

$$f = \frac{1}{2\pi\sqrt{LC}}$$
 (7), $L = \frac{\mu * N^2 * A}{1}$

The acquired ZVS equipment for performing MHT has a built-in capacitor bank, which means it has a fixed capacitance that cannot be modified. The equipment came with a coil which had 7 turns, a cross-sectional area A = 62mm, and a length I = 58.0 mm, that gave a calculated inductance of $L_c = 2.4$ µH, which was quite approximate to the real value measured $L_m = 2.2$ µH and a frequency f = 58.55 kHz. As the frequency depends on both capacitance and inductance, we opted to vary the inductance by building coils with different areas, numbers of turns, and lengths.

Although the frequency measured on the given coil is theoretically capable of performing the MHT, it did not work with the synthesized nanoparticles, so it was decided to work with higher frequencies. It was also needed to increase the magnetic field intensity (B) at the center of a circular coil which is given as $\mathbf{B} = (\mu_0 * \mathbf{n} * \mathbf{I}) / (2 * \mathbf{R})$, where μ_0 is the permeability of free space, n is the number of turns, l is the current, and l is the radius of the coil.

Different coil designs were tested to optimize the MHT heating. Table 3.2 compiles the most relevant values obtained with different coil models.

Table 3.2. Coil settings and parameters summary.

Number of turns (N)	Cross-sectional area (A) (mm)	Inductance (<i>L</i>) (µH)	Frequency (f) (kHz)	Magnetic field intensity (<i>B</i>) (mT)
7	62	2.20	58.55	2.21
4	38	0.60	100.10	33.50

After testing different coil designs and sizes, it was found that reducing the area of the coils was the most feasible approach, as this increased both the magnetic field intensity and frequency, resulting in the heating described in the following section.

MNPs heating

Figure 3.8 shows the MHT system utilized to stimulate MNPs with an AMF while the temperature change was measured with an Infrared (IR) camera (Fluke, TiS45). The system consisted of a 24 V power supply, with a 12 A current, inducing an AMF of 100 kHz through a 4-turn coil while it was cooled with water.

After turning on the equipment, the temperature was measured every minute for 12 minutes. Figure 3.9 A shows the temperature elevation of A-MNPs and N-MNPs at 100, 250, and 500 μ g/ml. Here, both groups of particles presented the highest temperature with the 250 μ g/ml concentration, reaching a rise of 7.2 and 8.9 °C for A-MNPs and N-MNPs, respectively.

Figure 3.9 B shows the temperature change corresponding to W-MNPs and EG-MNPs, which exhibited increases of 5.6 and 6.8 °C, respectively. A comparative analysis revealed that MNPs synthesized by coprecipitation, and within both groups of syntheses, EG-MNPs and N-MNPs presented better heating than W-MNPs and A-MNPs, respectively, where N-MNPs had the best heating (Figure 3.9).

Table 3.3 summarizes the values obtained by each group of nanoparticles at different concentrations.

Table 3.3. Temperature increase generated by MHT in MNPs.

	Coprecipitation synthesis				Reduction synthesis							
Label	A	A-MNP	s	1	N-MNP	s	-	A-MNP	s	1	N-MNP	S
Concentration	100	250	500	100	250	500	100	250	500	100	250	500
(µg/ml)												
ΔT (°C)	5.9	7.2	6.8	8.3	8.9	7	3.9	5.6	5.3	5.2	6.8	6

Besides the heating produced by the different synthesized MNPs, their specific absorption rate (SAR) was calculated using the formula.

$$SAR = C \frac{m_s}{m_p} \left. \frac{dT}{dt} \right|_{t \to 0} \tag{9}$$

The values obtained are presented in Table 3.4.

Table 3.4. SAR values for MNPs.

Sample	dT/dt (°C/s)	SAR (W/g)
A-MNPs	0.013	154.89
N-MNPs	0.016	231.58
W-MNPs	0.009	110.56
EG-MNPs	0.013	183.42

N-MNPs and EG-MNPs obtained the highest SAR values, indicating superior heating efficiency.

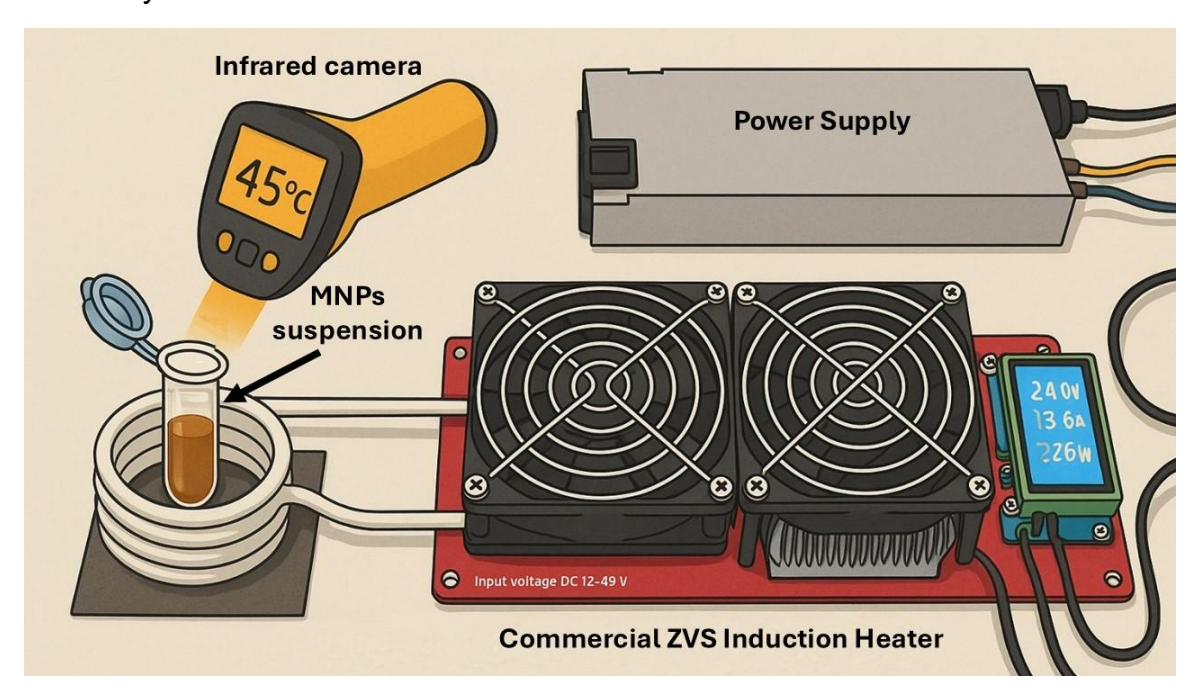


Figure 3.8. Diagram of the MHT heating system consisting of a commercial ZVS circuit connected to a 24 V power supply and cooled with water. The temperature change of the stimulated MNPs was recorded with an IR thermal camera.

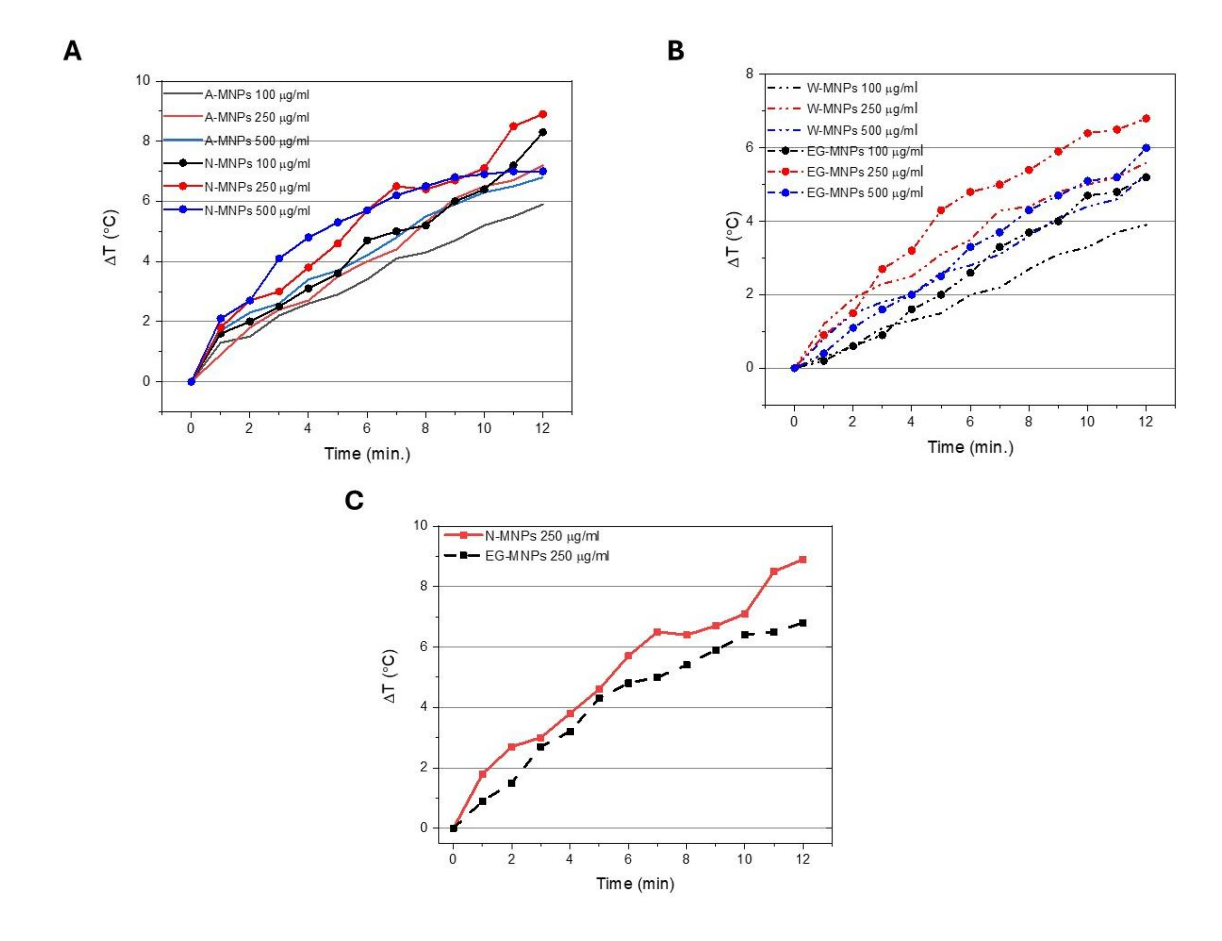


Figure 3.9. MNPs heated at different concentrations, 100, 250 and 500 μ g/ml. A) MNPs synthesized by coprecipitation, A-MNPs and N-MNPs. B) MNPs synthesized by reduction, W-MNPs and EG-MNPs. C) The concentration of 250 μ g/ml resulted to be the best in both syntheses, reaching an elevation of 6.8 and 8.9 °C, respectively. N-MNPs (solid lines) and EG-MNPs (dashed lines).

Fourier Transform Infrared Spectroscopy (FTIR)

MNPs coated with DMSA were analyzed through FTIR in the spectral region from 2000 to 500 cm⁻¹. Figure 3.10 shows the FTIR spectra of two molecules, DMSA and arginine, an amino acid, RGD, and MNPs at different stages of surface functionalization, where the appearance of different peaks corresponds to specific functional groups attached to MNPs. Each specific molecule can be divided into two main FTIR regions, one below 1500 cm⁻¹, which is considered the molecule fingerprint, as it presents unique and complicated groups in its bending vibration modes, and is different for each compound. On the other hand, above 1500 cm⁻¹, there are simple and functional groups on their stretching vibration modes, which can be present in different compounds.

For example, bare MNPs (black line) did not present any significant peak, this is because there is only iron oxide, lacking of functional groups; these groups are presented mostly in organic molecules, such as DMSA (red line) where are presented as a series of peaks within the spectra, the bands at $1703 \, \mathrm{cm}^{-1}$ and $1623 \, \mathrm{cm}^{-1}$ are assigned to v(C=0), all in their stretching vibration modes as they are presented in the range above $1500 \, \mathrm{cm}^{-1}$. Also, some deformation vibrations of C-H groups are visible in the range of $1342-1200 \, \mathrm{cm}^{-1}$. Then, after being bioconjugated with the RGD peptide, the band at $1641 \, \mathrm{cm}^{-1}$ is assigned to C=O from Amide I stretching vibration modes. The band at $1029 \, \mathrm{cm}^{-1}$ corresponds to the C–N from aliphatic amines, and $628 \, \mathrm{cm}^{-1}$ to the C–H bending.

3.5 MNPs selection for MHT

MNPs

MNPs synthesized in this work by both of the previously mentioned routes presented a morphology similar to spheres and a comparable crystalline structure. Nonetheless, the particles synthesized by reduction (W-MNPs and EG-MNPs) were almost double the size of the particles synthesized by coprecipitation (A-MNPs and N-MNPs). This last group has sizes below 30 nm, which makes them superparamagnetic by being within the magnetic monodomain. Thanks to this property, these particles show narrow hysteresis loops characterized mainly by low remanence magnetization and coercivity, with coercivity as the most important parameter, and it is inversely proportional, which means that with smaller particle size, there is an increase in coercivity and vice versa. Thanks to this, A-MNPs and N-MNPs presented a higher temperature elevation when stimulated with an AMF, reaching a couple of degrees more than W-MNPs and EG-MNPs, which made them the best option to be applied in MHT, and the addition of DMSA on their surface showed other advantages that will be presented later.

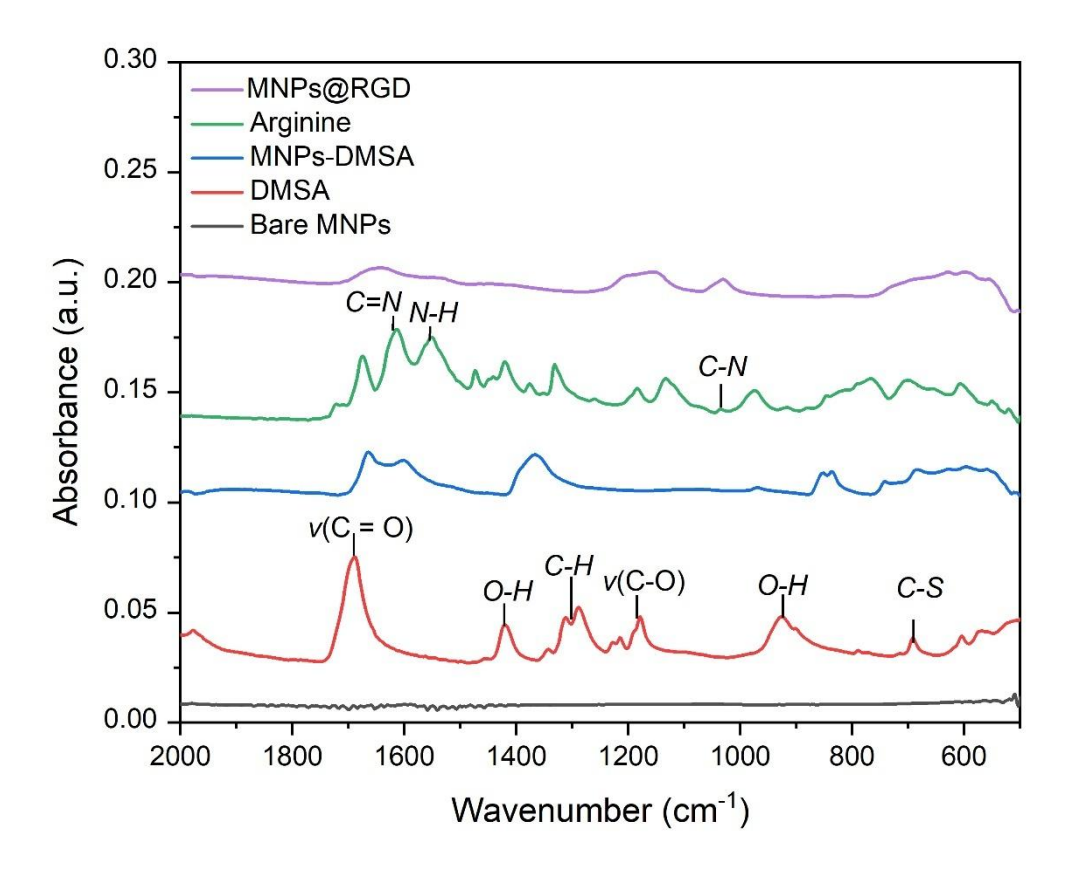


Figure 3.10. FTIR spectra of MNPs synthesized by coprecipitation. Bare-MNPs did not show any significant peak, while MNPs coated with DMSA (blue line) presented the appearance of peaks corresponding to the v(C=0), C-H, and O-H bands. MNPs@RGD (purple line) presented the appearance of peaks corresponding to different amine groups, C=N and C-N.

CHAPTER 4 MAGNETIC HYPERTHERMIA

4. Magnetic hyperthermia

After characterizing the particles and testing their ability to perform MHT, they were taken to the next level and they were evaluated in cell cultures. Here, two cell lines were used to accomplish the treatment in in vitro models. A series of tests was made to evaluate particles' cytotoxicity, specificity and the effects of MHT within the cells after being treated.

4.1 Materials

Dulbecco's Modified Eagle's Medium (DMEM), Roswell Park Memorial Institute (RPMI 1640), fetal bovine serum (FBS), Penicillin–Streptomycin, and Cell Proliferation Reagent WST-1 were purchased from Merck; Cyclo(-RGDyK) peptide (≥ 95 %) was acquired from AnaSpec, and Milli-Q water was used for the solution preparation and MNPs cleaning.

4.2 Cell Culture and Toxicity Studies

Cell culture

HCT-15 (human colorectal carcinoma) and HEK-293 (human embryonic kidney) cell lines were cultivated in the following fashion: HCT-15 cells were cultivated in RPMI-1640 medium, while HEK-293 cells were cultivated in DMEM. Both media were supplemented with 10% FBS and 1% penicillin–streptomycin. Both cell lines were grown at 37 °C in a 95% air and 5% CO₂ atmosphere.

WST-1 toxicity test

The HCT-15 cell line was selected to assess the Fe₃O₄ nanoparticle's toxicological and magnetic hyperthermia effects since HCT-15 cells are one of the most frequently studied cell lines when evaluating nanoparticle toxicity due to exposure to AMF. This cell line exhibits adherent growth, epithelial-like morphology, and a rapid migratory behavior. HCT-15 cells grow as adherent cells under the conditions described in this protocol. 2.5×10^4 cells were suspended in 100 µl of RPMI-supplemented medium for toxicity assay into 96-well plates (Costar, Corning, USA).

Some authors, as Soenen & De Cuyper [111] and Sun [112], mention a working range between 20 and 500 μ g/ml of nanoparticles, which are considered non-toxic. In our case, we used four different concentrations (30, 60, 125, and 250 μ g/ml) to achieve low cytotoxicity and efficient heating, which was obtained with 250 μ g/ml of particles.

It is worth mentioning that the use of different coatings or bioconjugations enhances the biocompatibility of the MNPs. Here, we compared the effects of Fe₃O₄-MNPs@DMSA and bare Fe₃O₄-MNPs using the previously mentioned

concentrations. A group of cells without MNPs was used as a control, and all groups were prepared in quadruplicate.

Cell cultures were incubated for 24 hours at 37 $^{\circ}$ C and 5% CO₂. Then, 10.0 μ l of WST-1 was added to each well and incubated for 2 hours at 37 $^{\circ}$ C and 5% CO₂. Finally, the plate was shaken for 1 minute, and the absorbance was read on a Thermo Scientific Multiskan FC spectrophotometer at 450 nm.

MNPs specificity tests

The two cell lines were used to test the specificity of RGD-coated MNPs: HCT-15 as cancerous cells overexpressing $\alpha\nu\beta3$ and $\alpha\nu\beta5$ integrins, and HEK-293 as a control group with a lower integrin expression [108]. 2 × 10⁵ cells of each line were suspended in 1 ml of its respective supplemented culture medium, RPMI-1640 for HCT-15, and DMEM for HEK-293. Additionally, medium containing MNPs@RGD (0, 50, and 100 µg/ml) was added, poured into 24-well plates, and incubated for 24 hours at 37 °C and 5% CO₂. After the incubation time, the medium was removed from the wells, and cells were washed three times with PBS to remove MNPs that were not attached to the cells, and then fixed with 4 % formaldehyde solution for 15 minutes. After this, the solution was removed, and the cells were washed with PBS.

A 1 % potassium ferrocyanide (Prussian Blue (PB)) solution was prepared and mixed with 0.2 M HCl (1:1). 300 μ l of PB solution was added to each well, removed after 15 minutes of reaction, and then washed with PBS. Hematoxylin and Eosin (H & E) solutions (10 %) were used to counterstain the PB dye [113]. First, hematoxylin was added to the cells for 2 minutes and washed out, and finally, eosin was added for 3 minutes and washed out. Cells were observed using an inverted microscope with a 40× objective.

4.3 Magnetic hyperthermia and protein assay

Magnetic hyperthermia: To demonstrate the effect of hyperthermia on the cells with A-MNP stimulated with AMF. To organize the cells into the coil (D = 3.5 cm), a 3 × 3 well arrangement was prepared by cutting from 96-well plates and subsequently sterilized (Figure 4.1). After this, 2.5×10^4 HCT-15 cells were suspended in 100 μl of supplemented RPMI-1640 medium, and incubated for 24 hours at 37 °C and 5% CO₂, after this time, the medium was removed from the wells and replaced with 100 μl of MNPs@RGD diluted in RPMI medium at 0, 100, 200, and 1000 μg/ml concentrations. After another 24 hours of incubation under the same conditions, the well plate arrangements were placed in the middle of the coil of the hyperthermia equipment, a commercial ZVS circuit with a frequency operation of 100 kHz, 2500 Watts, powered with 40 V and 8 A current. For this study, five samples of cells were prepared; one sample (in triplicate) was selected as a positive control and was not stimulated with AMF. The next four samples were prepared in triplicate and incubated for 24 hours with 0, 100, 200, or 1000 μg/ml of A-MNPs and stimulated with AMF

(100 KHz) for 100 minutes. After stimulation, all samples were taken into the incubator for 24 hours for further analysis.

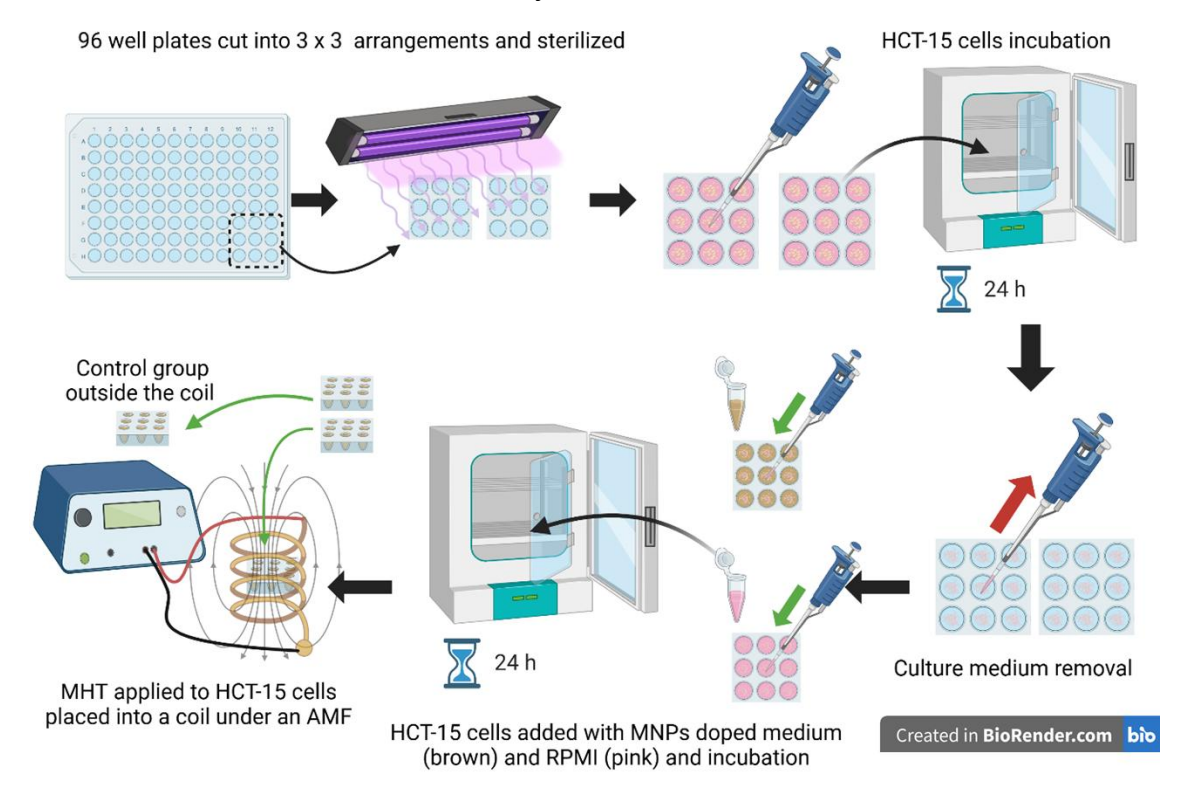


Figure 4.1. Schematic diagram for MHT application in vitro. 3 x 3 well arrangements were cut and sterilized to cultivate cells for 24 hours. Then they were added with different MNPs concentrations (0 - 1000 μ g/ml) and incubated again for 24 hours. Finally, they were taken to the MHT system for stimulation.

4.4 Protein Analysis

Electrophoresis SDS-PAGE

Before protein separation and analysis, cell integrity was determined by SDS-PAGE and Coomassie blue staining, which confirmed that the extraction, quantification, and separation of proteins were carried out satisfactorily, following the Bio-Rad protocol [110].

Electrophoresis is commonly used for the purification, analysis, and characterization of proteins. It was carried out under denaturing conditions using sodium dodecyl sulfate (SDS) as a detergent, which disrupts hydrophobic interactions with proteins. The molecular weight of proteins can be determined by the amount of SDS binding to them because it is proportional to their size, and each SDS-protein complex has a specific charge-mass value [111].

The procedure was performed using precast gels (4-15%) of Bio-Rad Mini-PROTEAN TGX, which were mounted in a Mini-PROTEAN 3 Cell system for electrophoretic adjustment with 1× run buffer (25 mM Tris, 190 mM glycine, and 0.1% SDS) inside. Subsequently, 20 µg of protein per sample was loaded into each rail, avoiding the formation of bubbles. After adding the samples to the wells, the camera cap was closed, ensuring that the anode and cathode of the electrodes were correctly connected. The cap was connected to a BioRad PowerPac HC power supply with an initial voltage of 60V to allow samples to enter the gel, and once the samples were properly loaded and aligned, the voltage was increased to 100V until the separation was complete.

When the electrophoresis was completed, the gels were carefully removed from the chamber with a spatula. Then the gels were placed in a container with distilled water for 10 minutes to remove the excess SDS before the staining protocol.

Gel staining and scanning

The gels were placed in Coomassie's blue solution under constant stirring overnight. Then the dye was removed, and a bleaching solution was added and allowed to stir until the protein bands were visible.

Once the gels were bleached, they were hydrated with distilled water and stirred for 10 minutes. Finally, the gels were scanned using a BioRad GS-900 densitometer, and the images were processed using computer software.

Western blot protein analysis

Following an assessment of the proteins' integrity, biochemical analysis was conducted to identify the proteins using the Western blot. This process was performed using SDS-PAGE electrophoresis to separate proteins, with an OmniPAGE Mini Modular System featuring 20 wells. For this, the glasses were first assembled, previously washed with a detergent solution, rinsed with distilled water and 70% ethanol, and placed on a rubber in the chamber support to form the gel cassette, and allowed to align on a flat surface.

Subsequently, 5% concentrator gels and 12% separator gels were prepared for protein separation following the specifications outlined in Table 4.1 of the Sambrook protocol [114].

Table 4.1. Solutions for preparing electrophoresis gels

Components	Concentrator gel (10 ml)	Separation gel (30 ml)
H ₂ O	6.8	9.9
Acrylamide 30%	1.7	12.0
Tris 1.5M (pH 8.8)	-	7.5
Tris 1.0 M (pH 6.8)	1.25	-
SDS 10%	0.1	0.3

Ammonium persulphate (APS) 10%	0.1	0.3
TEMED	0.01	0.012

First, the solution of the separator gel was prepared (15 ml for each gel), mixed gently, and added between the glasses with a micropipette, so that the level reached approximately 1 cm before the edge of the glasses. Immediately, 70 % ethanol was added to remove bubbles, align the gel, and avoid contact with air, about 15 minutes after the solution was polymerized, and the ethanol was carefully removed.

Then, the concentrator gel was prepared (2 ml for each gel). The mixture was added between the glasses to its limit, and the comb was placed immediately to avoid the formation of bubbles. Fifteen minutes later, the solution was polymerized, and the comb was removed. Subsequently, the glasses with the gels were removed from the supports and placed in the running chamber, which was filled with 1x running buffer.

As a next step, one of the wells was loaded with $5.0~\mu l$ of molecular weight marker (MWM), and then the remaining samples were loaded according to the volume corresponding to $10~\mu g$ of protein.

The system was connected to a BioRad PowerPac HC power source, and samples were run at 60 V until they reached the separator gel. Then, the voltage was elevated to 100 V until they reached the end of the gel.

Transfer to the wet chamber.

At the end of electrophoresis, the gels were removed by cutting the comb wells with a spatula from the electrophoresis chamber and then placed in a container with transfer buffer for approximately 20 minutes. The wet chamber transfer was then performed using the Omni-PAGE Mini Modular Systems camera transfer equipment and a 0.45 μ M BioRad PVDF membrane previously activated with methanol for 2 minutes. A cold transfer buffer was added to a container by placing the open transfer cassette and assembling it, as shown in Figure 4.2.

When the cassettes were assembled, they were placed inside the transfer chamber, and a cold transfer buffer was added until the cassettes were covered. Then, the camera was in a container with ice inside the cold room, and the transfer was carried out at 1.15 h / 250 mA / 4 $^{\circ}$ C. Upon completion of the transfer, the membrane was removed, stained with red Ponceau dye for approximately 10 minutes to identify proteins and rinsed with TBS-Tween 0.05 $^{\circ}$ 6 until faded.

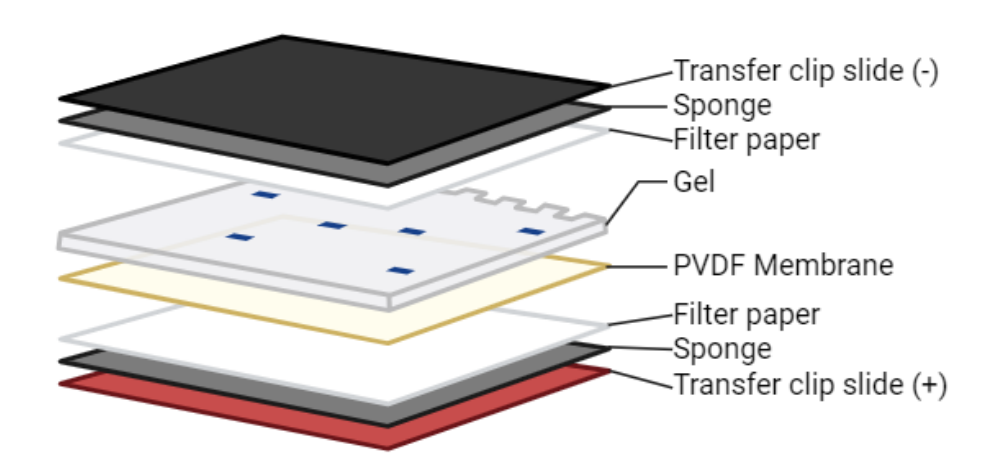


Figure 4.2. Order of assembly of a transfer cassette. The stack is assembled between the negative (-) and positive (+) electrodes of a transfer apparatus. From cathode to anode, the stack consists of: the cathode transfer clip slide, a sponge, a sheet of filter paper, the polyacrylamide gel, the PVDF membrane, a second sheet of filter paper, a second sponge, and the anode transfer clip slide.

Membrane blocking

Immediately after rinsing, the membranes were incubated in a blocking solution using Svelty skimmed milk according to the specific conditions for each antibody, according to Table 4.2. The blockade was carried out in constant agitation.

Table 4.2. Blocking conditions

Antibody	Blocking conditions
GAPDH	Milk 3% in TBS-Tween 0.05% for 1 h at 4 °C
Caspase 3	Milk 3% in TBS-Tween 0.05% for 1 h at 4 ℃
Alpha Tubulin	Milk 3% in TBS-Tween 0.05% for 1 h at 4 °C
Beta Actin	Milk 3% in TBS-Tween 0.05% for 1 h at RT
Beta Tubulin	Milk 3% in TBS-Tween 0.05% for 1 h at RT

Incubation with primary antibodies

To determine the effect of hyperthermia, the proteins involved in the molecular mechanisms were tested according to the respective antibody and their molecular weight. After the membrane blocking was completed, the blocking solution was removed and incubated with a solution containing the primary antibody according to the dilution and incubation conditions detailed in Table 4.3. The antibodies were incubated overnight at 4°C under constant stirring.

Table 4.3. Incubation conditions for primary antibodies

Antibody	Catalog number/Commercial house	Incubation conditions
GAPDH	sc-25779, Santa Cruz Biotechnology	1:1000 in milk, 3% in TBS- Tween 0.05%
Caspase 3	110543, Genetex	1:2000 in milk, 3% in TBS- Tween 0.1%
Alpha Tubulin	ab48389, abcam	1:2000 in milk, 3% in TBS- Tween 0.1%
Beta Actin	MAB8929, R&D Biosystems	1:2000 in milk, 3% in TBS- Tween 0.1%
Beta Tubulin	MAB8527, R&D Biosystems	1:2000 in milk, 3% in TBS- Tween 0.1%

After incubation, the membranes were washed 3 times for 5 minutes each with their respective buffer, TBS-Tween.

Incubation with secondary antibodies

The previously washed membranes were incubated with secondary antibodies at room temperature under constant stirring, as described in Table 4.4.

Table 4.4. Secondary antibody incubation conditions

Antibody	Secondary antibody	Incubation conditions
GAPDH	goat anti-rabbit	1:10,000 in milk 3% in TBS-Tween 0.05%, at 4 °C for 1 h
Caspase 3	goat anti-rabbit	1:10,000 in milk 3% in TBS-Tween 0.1%, at room temperature for 1 h
Alpha Tubulin	goat anti-rabbit	1:10,000 in milk 3% in TBS-Tween 0.1%, at room temperature for 1 h
Beta Actin (45 kDa)	goat anti-rabbit	1:10,000 in milk 3% in TBS-Tween 0.1%, at room temperature for 1 h
Beta Tubulin (50 kDa)	goat anti-rabbit	1:10,000 in milk 3% in TBS-Tween 0.1%, at room temperature for 1.5 h

Membrane development

The membranes were developed to identify proteins of interest marked with the respective antibodies. For this procedure, the Millipore WBKLS0500 Immobilon Substrate Quimoluminating Transfer Kit from HRP was used. Each membrane was carefully handled, and 2 ml of the kit's solution mixture at a 1:1 concentration was added to it. The membrane was then placed on Bio-Rad's ChemiDoc MP Photo Binder and exposed until the protein bands were visible.

Finally, the generated data was analyzed using BioRad's Image Lab 6.1 software to study the level of protein expression in each membrane.

4.5 Results of MNPs biocompatibility, specificity, and MHT in vitro

Biocompatibility tests

The viability of HCT-15 cells exposed to Fe₃O₄ NPs at different concentrations, 30, 60, 125, and 250 μ g/ml with and without DMSA was evaluated by WST-1 assay. HCT-15 cell cultures were exposed to bare MNPs and N-MNPs, and the dose-response curves were obtained (Figure 4.3). It was observed that Fe₃O₄ NPs without DMSA significantly reduced cell survival from 89.8% to 47.2% at concentrations ranging from 30 μ g/ml to 250 μ g/ml. On the other hand, MNPs coated with DMSA improve the cell survival rate, with a value of 97.6% at 30 μ g/ml, and it falls to only 79.0% at a concentration of 250 μ g/ml. The results show that Fe₃O₄ NPs coated with DMSA during the synthesis reduced the toxic effects of Fe₃O₄ core NPs.

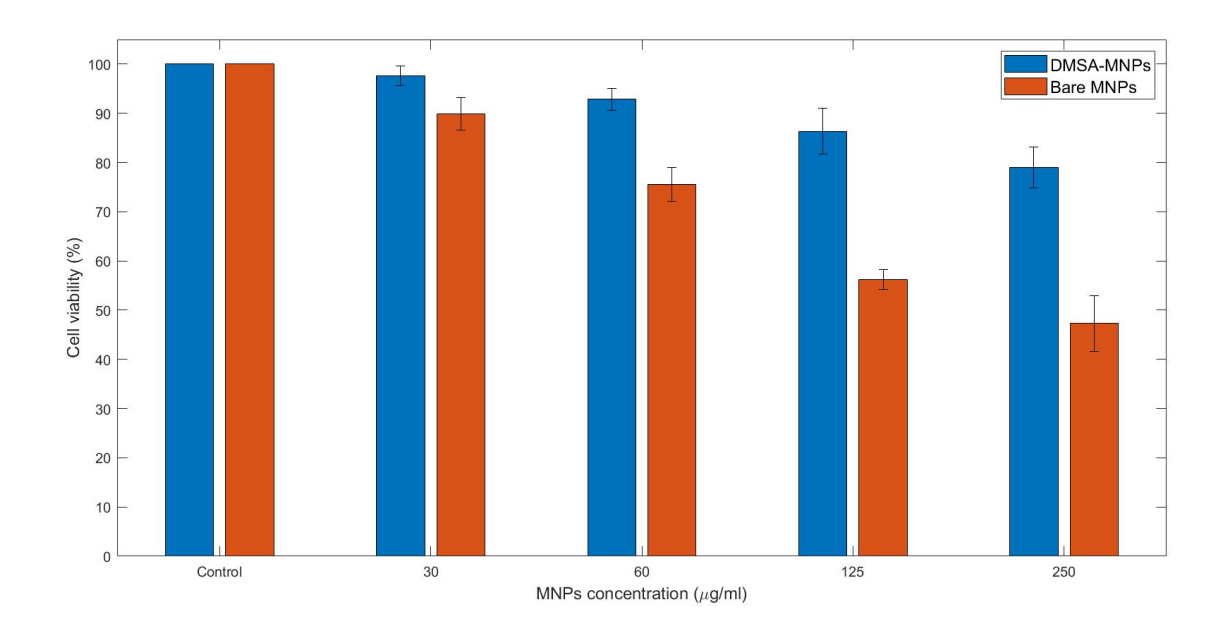


Figure 4.3. Cellular viability percentages for different MNPs concentrations, bare Fe3O4, and coated with DMSA. Both groups of MNPs present a linear tendency of toxicity as the particles' concentration increases. Nonetheless, DMSA-MNPs only presented a 21 % cell death at the highest concentration (250 μ g/ml), while bare MNPs reached a 53 % cytotoxicity.

Specificity tests

The iron attached to cells was observed after the PB reaction, where MNPs appear as dark blue stains surrounding or within the cancer cells. It can also be observed that a pink-like staining of cells' cytoplasm, by the H&E counterstain, where acidic eosin counterstains the basic elements, such as the cytoplasm. As previously mentioned, HCT-15 cells exhibited a dark blue coloration when the MNPs were linked to the cells (Figure 4.4 A, C, E, and G). On the other hand, HEK-293 cells did not present notorious blue staining, indicating a low or null adhesion of MNPs to them (Figure 4.4 B, D, F, and H).

On the top row of Figure 4.4 (A and B), the morphology of both cell lines is appreciated; in the left column, HCT-15 cells are observed to form projections, as they are an adherent line and use their cell extensions to adhere onto the cell culture dishes. On the other hand, in the right column, HEK 293 cells have a fibroblastic shape with extensions that become thinner as they move away from the cell center. In both cases, the pink and red coloration of the cytoplasm is appreciated, while the nuclei and organelles appear darker due to the H&E stain counterstain.

On the second row of Figure 4.4 (C and D), dark blueish spots, marked with white arrows, can be observed corresponding to the MNPs@RGD (50 µg/ml) added to the cell cultures. In the case of HCT-15 cells, these dark spots appear around or within most of the cellular membranes, as the RGD peptide has an affinity for integrins, proteins overexpressed on these cells. Contrarily, there are just a few or no MNPs@RGD attached to HEK 293 cells, which do not present as many integrins on their membranes as the HCT-15 line.

The third row in Figure 4.4 (E and F) shows a higher area of dark spots, indicating a major concentration of MNPs@RGD ($100 \mu g/ml$). In the case of HCT-15 cells, there is a higher adhesion of particles to the cells, despite being present in several cells, these did not present a significant change in their structure, it still can be seen the membrane of each cell, while in HEK 293 cells some dark agglomerates are observed, however most cells are not attached or surrounded by MNPs@RGD.

Finally, in the last row, Figure 4.4 (G and H), the nanoparticles have already adhered to most of the HCT 15 cells, with particle agglomerates completely covering the cells. On the other hand, in the case of HEK 293 cells, MNPs@RGD still do not appear in large quantities, only some isolated stainings.

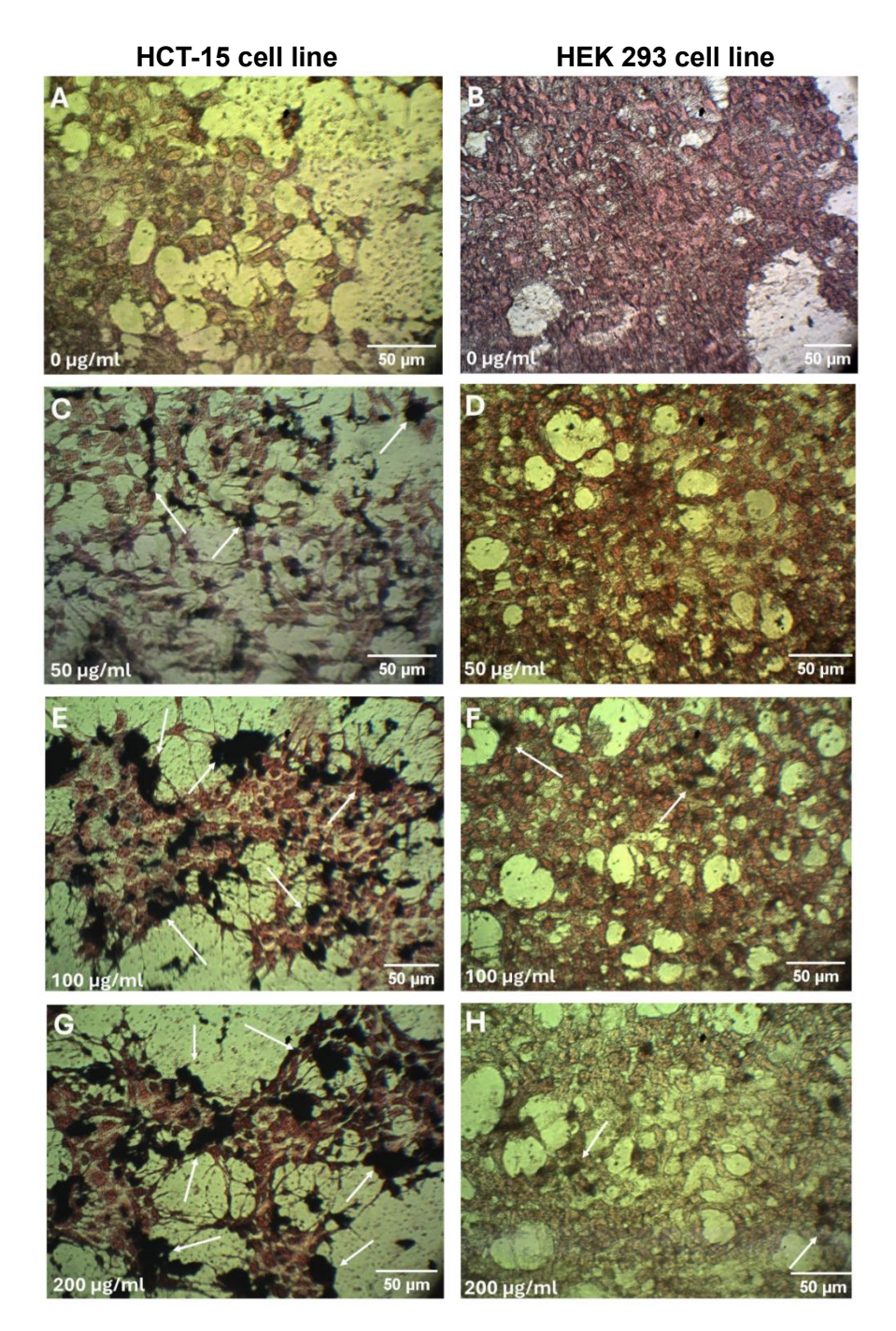


Figure 4.4. Combined PB and H&E staining of HCT-15 and HEK 293 cell lines treated with increasing concentrations (0, 50, 100, 200 μ g/ml) of MNPs@RGD. A, C, E, G (HCT-15 cells): Show internalized MNPs@RGD (dark blue, indicated by arrows) and cytoplasm (pink). B, D, F, H (HEK 293 cells): Show minimal MNP uptake, with only occasional agglomerations outside cells (arrows) and pink cytoplasmic staining.

Magnetic hyperthermia

Figure 4.5 presents the temperature elevations for different particle concentrations after 100 minutes of magnetic stimulation. When cells without the addition of MNPs@RGD (0 μ g/ml) were set in the midpoint of the coil and then stimulated, the temperature did increase 3 °C (Figure 4.5 A). This short variation in temperature is due mainly to the heating induced by the hyperthermia equipment itself and was not enough to cause significant damage to the cells.

When nanoparticles with a concentration of 100 μ g/ml were added, a heating of 6 degrees was obtained after 100 minutes of stimulation (Figure 4.5 B). Approximately 1 hour after initiating the stimulation, the 5 °C necessary to induce cell death by MHT was reached. After this time, the remaining 40 minutes of stimulation, the temperature increased by only 1 °C.

When 200 μ g/mL of MNPs were added (Figure 4.5 C), the temperature increase was comparable to that observed at 100 μ g/mL. However, it required approximately 20 minutes more to reach the 5 °C necessary to induce cell death by MHT, and at the end of the stimulation time, it did not reach the 6 °C obtained with half of the concentration. It is worth mentioning that by adding more MNPs to the culture medium suspension, they tend to precipitate more quickly, which results in a lower temperature increase.

Finally, a very high concentration of MNPs (1000 μ g/ml) was used to ensure cell death (Figure 4.5 D), not only due to the heating, but also due to the high particle concentration that turns out to be toxic itself. In this case, the particles were precipitated again, as in the previous case. They only performed some temperature readings above 6 °C in the last minutes of stimulation, reaching 5 °C shortly after the stimulation hour.

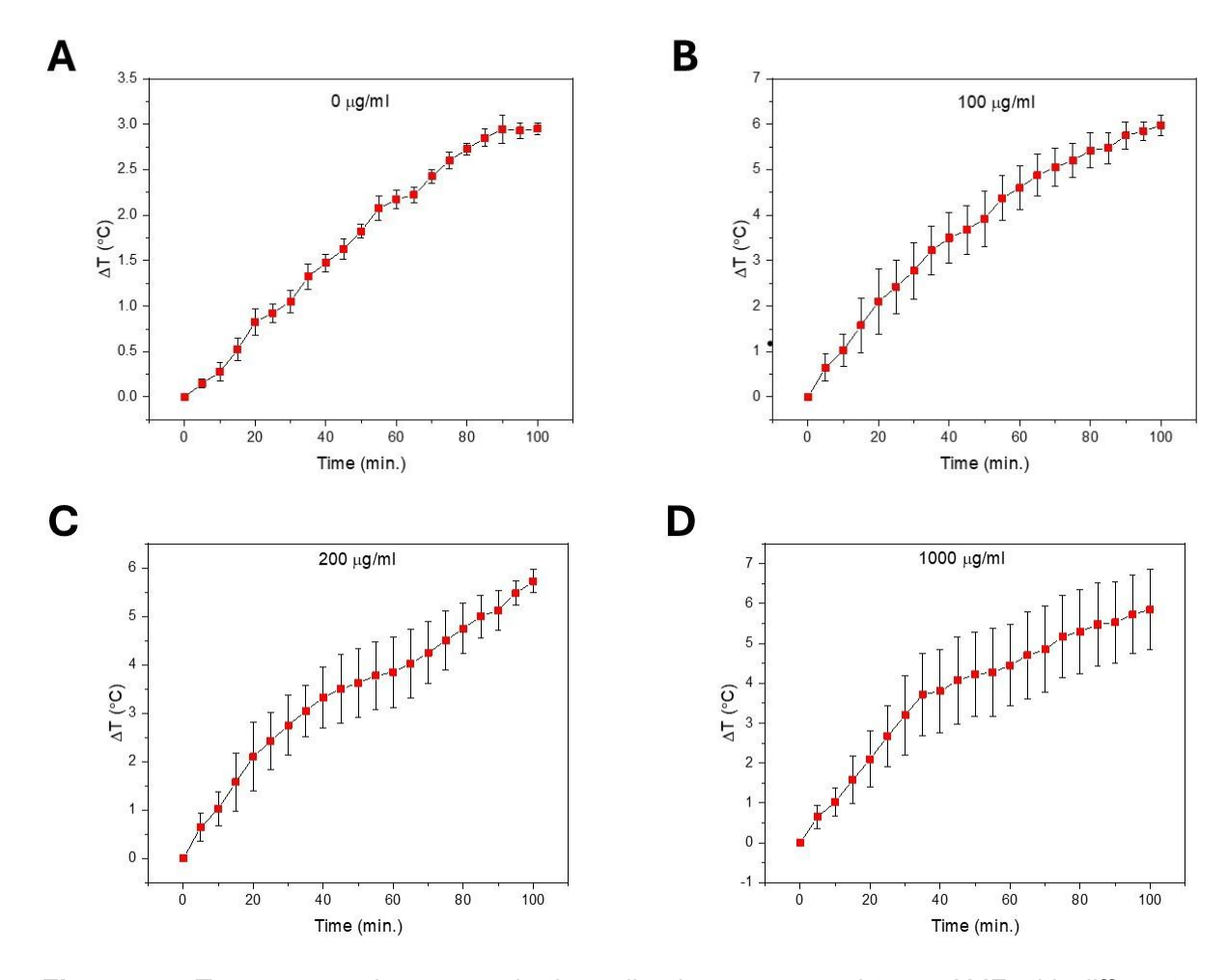


Figure 4.5. Temperature rise means in the cell cultures exposed to an AMF with different MNPs@RGD concentrations. A) 0 μ g/ml. B) 100 μ g/ml. C) 200 μ g/ml. D) 1000 μ g/ml. In the absence of MNPs, there was only an elevation of 3 °C; in the following concentrations: 100, 200 and 1000 μ g/ml, the temperature increased over 5 °C.

Cell viability test

Figure 4.6 shows the percentage of cell viability 24 hours after exposure to the MHT. They exhibit an almost linear decline in viability as the concentration of MNPs increases. To achieve greater similarity in the conditions of cells exposed to MHT, positive viability controls were established by removing cells from the incubator and placing them next to the stimulated cells, but outside the coil, to prevent them from being affected by the magnetic field, as shown in Figure 4.1.

Additionally, a group of cells was exposed to the AMF without the presence of MNPs in the medium to evaluate the effects of the magnetic field on the cells themselves. In this group, labeled as 0 μ g/ml, the highest rate of cell death was approximately 15%, given by the lowest viability percentage of 85.14 % (Figure 4.6), although it is

not the temperature threshold required for the MHT, which could have induced cellular stress and consequently reduced cell viability.

For the case where 100 μ g/ml of MNPs were added to cells, a 33% decrease in viability was achieved, which is slightly more than double that obtained in the case where no nanoparticles were used. Subsequently, the concentration of particles at 200 μ g/ml decreased viability to just over half; in this case, the achieved decrease reached 55%, resulting in a viability of only 45% of cells (Figure 4.6).

Finally, as expected, the highest particle concentration (1000 μ g/ml) reduced cell viability by up to 18%, meaning that it induced cell death in approximately 4 out of 5 cells in the culture. Although the temperature reached did not exceed 6 °C, as in the case of the 100 μ g/ml concentration, the elevated number of nanoparticles was the main contributor to the high cytotoxicity achieved. Table 4.5 summarizes the viability values obtained for each group in the four experimental sets performed.

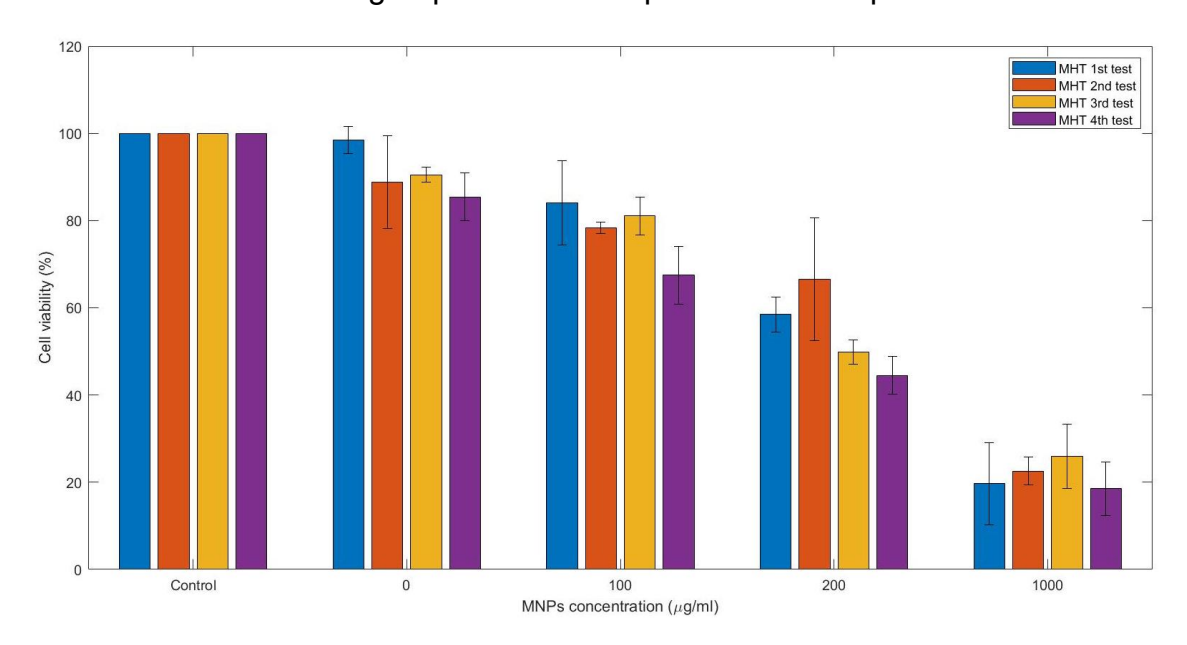


Figure 4.6. WST-1 cell viability assay after exposing cells to MHT. The increase in MNPs concentration in MHT significantly reduced their viability. In the absence of MNPs, but with magnetic stimulation, cellular viability was reduced by \sim 10 %, it dropped by \sim 15 % with a 100 µg/ml concentration, and by \sim 45 and 80 % with concentrations of 200 and 1000 µg/ml, respectively.

Table 4.5. Cellular viability for cells exposed to MHT.

MHT	Control	0 μg/ml		100 μg/ml		200 μg/ml		1000 μg/ml	
Experiment	Mean	Mean	Std Err	Mean	Std Err	Mean	Std Err	Mean	Std Err
1st Test	100	98.48	3.13	84.09	9.68	58.49	4.026	19.71	9.41
2nd Test	100	88.83	10.58	78.34	1.36	66.51	14.03	22.59	3.15

3rd Test	100	90.52	1.77	81.09	4.22	49.92	2.77	25.95	7.42
4th Test	100	85.44	5.44	67.48	6.68	44.49	4.30	18.54	6.17

Prussian Blue / Hematoxylin & Eosin staining

Figure 4.7 shows the combination of PB and H&E staining for the cells treated with MHT. It can be observed that increasing MNP concentration in the treatment affected the cells' structures. When the cells were exposed to the AMF without adding MNPs, they did not exhibit significant morphological changes or visible malformations. The outer edges of the cells can be seen in a darker reddish shade than the inside, corresponding to the membrane that surrounds each cell; nonetheless, during the cells' processing, there could be some cell damage due to their manipulation or exposition to formaldehyde, which produced som red dying outside the cells, but not considerable (Figure 4.7 A, B).

In the case of cells treated with 100 μ g/ml of MNPs, most of them seem to preserve their membrane intact, but their nuclei are hardly observed only in a few cells, the cellular cytoplasm appears to be dispersed outside of cells, some of them seem to have shrunk or in some cases fragmented when compared with the previous micrographs (A and B), besides the shrinkage a dark coloration is observed on the edges of the membrane that can correspond both to MNPs@RGD (Figure 4.7 C, D).

For cells to which 200 μ g/ml of MNPs were added, it is observed how their cell membranes disappeared almost completely, some of their cytoplasm is dispersed outside the cells (red arrows), and denser structures are presented out of the cells that could correspond either to cellular residues or MNPs@RGD (blue arrows) (Figure 4.7 E, F).

Finally, the cells with the major MNPs concentration, 1000 μ g/ml, seem to have lost almost all of their cellular integrity, it is very difficult to observe a well-defined cell membrane; the cytoplasm and cellular organelles are no longer inside the cells and dark spots appeared that could correspond to the dispersed nucleic material and MNPs (Figure 4.7 G, H).

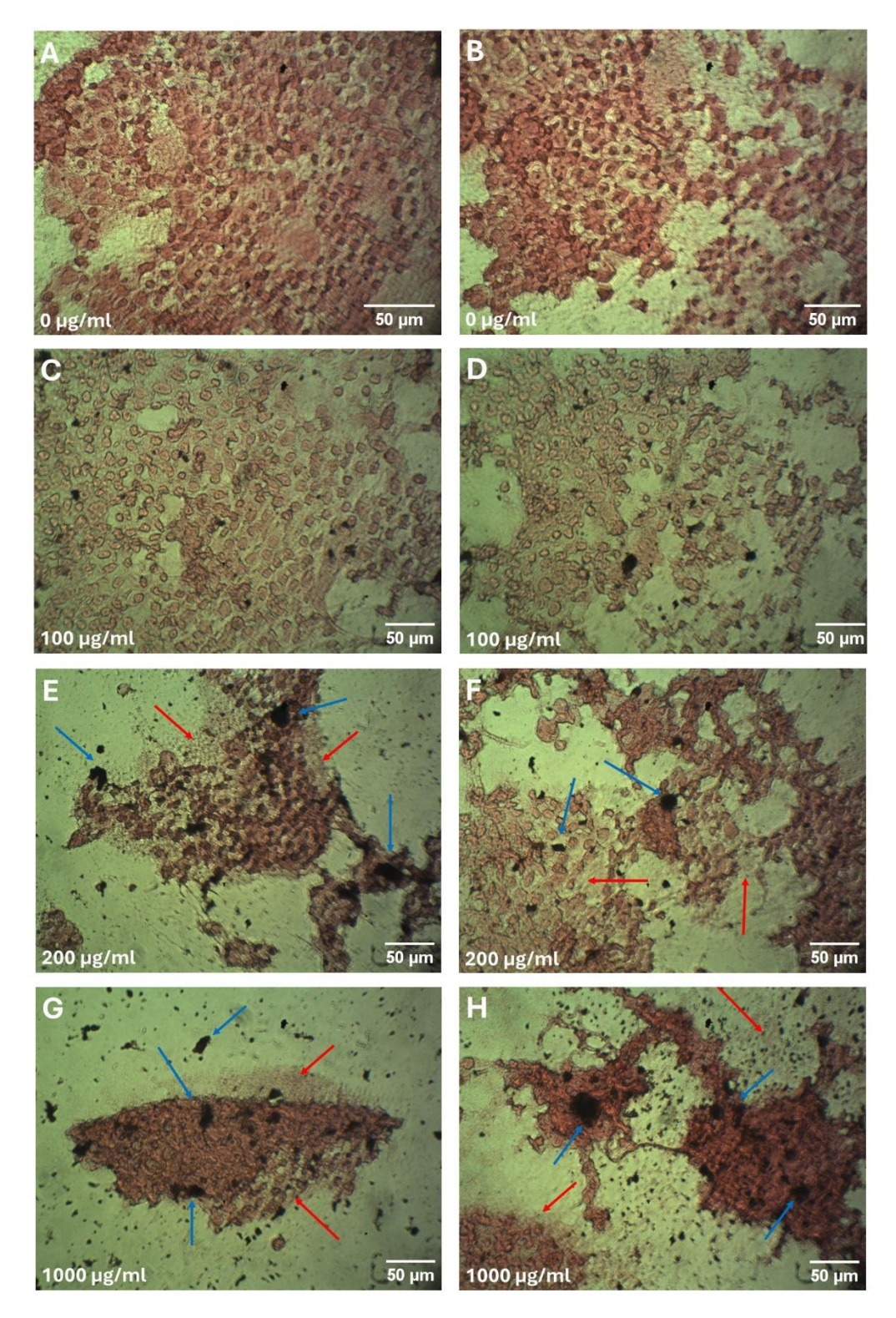


Figure 4.7. PB and H&E combination stain on cells treated by MHT with different MNPs concentrations. A), B) 0 μ g/ml. C), D) 100 μ g/ml. E), F) 200 μ g/ml. G), H) 1000 μ g/ml. The cellular morphology and integrity were lost as the MNPs' concentration increased.

Protein analysis

Figure 4.8 shows the electrophoretic migration pattern of two cell groups (A and B), which were stimulated for 100 minutes under magnetic hyperthermia treatment with different MNPs concentrations (0, 100, 200, or 1000 μ g/ml).

As a lane overview (from left to right), lane 1 corresponds to the molecular weight marker (MWM); here, the ladder shows distinct, evenly spaced bands indicating accurate protein sizing that was used as a reference for estimating molecular weights of experimental bands. On the second lane (control), there are strong and sharp bands in the mid region (~37–50 kDa), indicating the presence of intact proteins. However, there is also some fainting in the lower bands, indicating minor protein degradation.

The appearance and intensification of a distinct band at higher nanoparticle concentrations suggest the induction or accumulation of a specific protein associated with magnetic hyperthermia. Likewise, the strong bands may correspond to heat shock proteins (HSPs) or stress-induced proteins.

Lane 3 (0 µg) exhibits a pattern similar to the untreated control, validating that magnetic field exposure alone does not cause significant molecular change, suggesting that the effect is nanoparticle concentration-dependent. Some diffuse bands indicate partial denaturation or aggregation; finally, the appearance of lower MW species suggests proteolysis or thermal degradation (Figure 4.8).

Lanes 4, 5, and 10 correspond to the first series of applied MHT, labeled as A_{100} , A_{200} and A_{1000} , respectively. In them, there is no show the appearance of any band above a molecular weight (MW) of 50 kDa. This is due to the exposure to MHT, where the proteins were broken down into smaller portions and thus with a lower MW, which can be observed in the respective lanes.

For the second experimental group, named B, lanes 6, 7,8, and 9, corresponding to concentrations of 1000, 0, 100, and 200 μ g/ml, and labelled as B₁₀₀₀, B₀, B₁₀₀, and B₂₀₀, respectively. This experiment seems to have maintained a better protein integrity than experiment A; however, there was an accumulation of proteins around the 50 kDa band, and it is even more prominent in the lane where no MNPs were added.

In Figure 4.9, the western blot shows the band of Glyceraldehyde-3-phosphate dehydrogenase (GAPDH) at a molecular weight of 37 kDa. These bands can be observed in the control and A_0 samples; however, the bands corresponding to samples submitted to the AMF with different concentrations of MNPs disappeared, indicating protein denaturation.

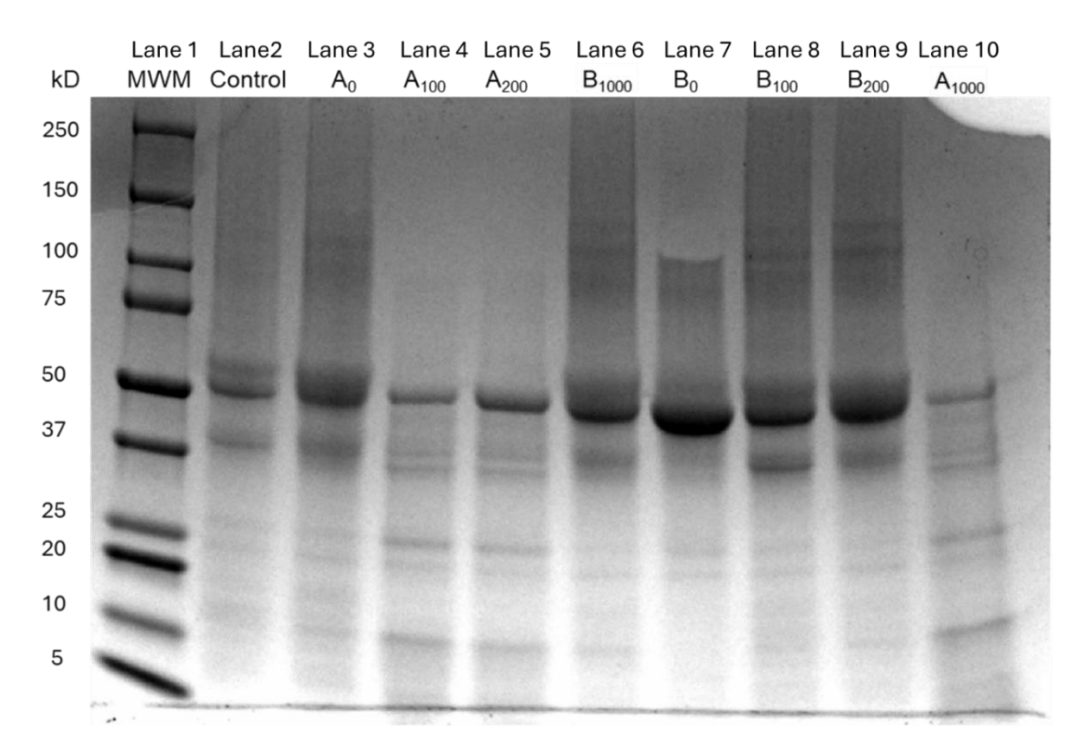


Figure 4.8. Gel electrophoresis for evaluation of protein integrity after MHT. The control lanes do not show significant protein degradation. Nonetheless, the lanes with proteins that were treated with 100, 200, or 1000 μg/ml show the disappearance of high MW bands or protein agglomeration.

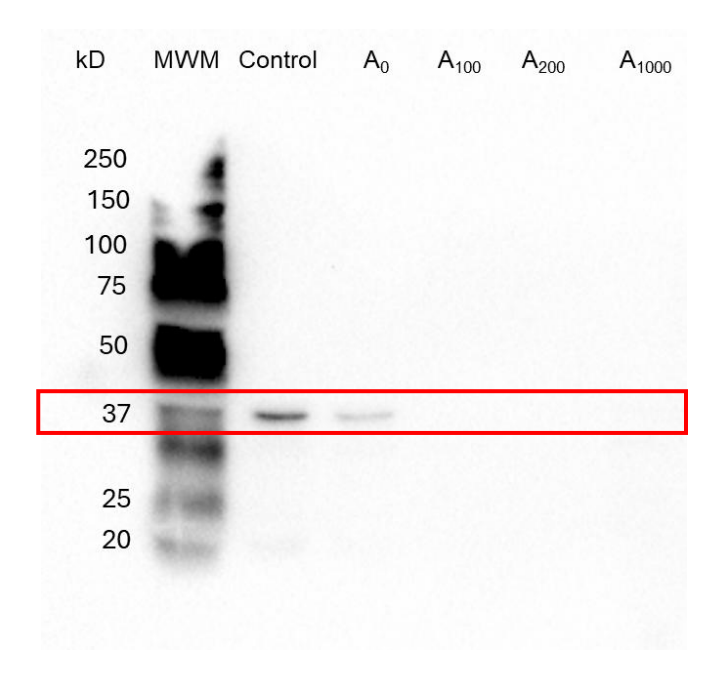


Figure 4.9. Western blot for GAPDH (37 kDa). The band only appeared in the control lane and the one with no MNPs. While in the groups treated by MHT with MNPs, the band did not appear, indicative of protein denaturation.

CHAPTER 4 DISCUSSION

4. Discussion

The presentation and discussion of the results obtained during the development of this research work are divided into three major parts. The first one discusses how the particles were prepared, from their synthesis to their characterization, and how the results obtained are comparable with particles synthesized by other routes. The second one describes how the synthesized particles were able to perform MHT and their promising results as heating agents for their specificity and lethality. Finally, it is discussed how the modified synthesis routes presented an enhancement in particle properties and performance.

This study investigated a modified synthesis route by co-precipitation. This method is commonly used in nanoparticle synthesis because it is simple, does not require long reaction times or high temperatures, and hardly achieves a monodisperse nanoparticle distribution.

The synthesized particles presented excellent properties to be employed in biomedical applications, such as magnetic hyperthermia treatment. Among some of their attributes, our MNPs are monodisperse, which indicates a narrow particle size distribution; superparamagnetic, meaning that they do not maintain magnetization in the absence of an external magnetic field; and biocompatible, thanks to the molecule attached to their surface, because MNPs did not present a significant toxic effect on cells by themselves, but until reaching elevated concentrations; these properties are required to apply MHT in biological systems.

After analyzing the XRD patterns and the SEM images, it was found that indeed a high percentage of the iron oxide prepared was magnetite by the characteristic peaks in the diffractograms, besides the fact that both syntheses reached a low polydispersity index, which is helpful when using them for MHT. It is also worth mentioning that the obtained XRD patterns in the co-precipitation synthesis are similar to the ones presented by Patel [107], and the peaks obtained showed a better definition than the ones presented by Dheyab [106], which indicates a better crystalline structure. As for the MNPs synthesized by the reduction route in both solvents, deionized water, and EG the XRD patterns are very similar to those presented by Aslam [115]. Also, the low values of coercivity, magnetic remanence, and high magnetic saturation are characteristic of superparamagnetic materials, which were intended to be obtained by the particles and confirmed by SEM images.

In addition, the use of DMSA as a coating agent provided several advantages, like its biocompatibility enhancement, aggregation reduction, and functional groups capable of performing a subsequent bioconjugation by a peptide that specifically targets cancerous cells. The ability of this peptide (RGD) could be observed when comparing the blue staining between cancerous and regular cells (HCT-15 and HEK-293), where it can be appreciated how the MNPs@RGS attached to the cancerous

cell line, while they did not adhere to the regular cells, despite having high particle concentrations.

Taking advantage of this specificity, the MHT results were satisfactory because by only using a low concentration of 100 μ g/ml, MNPs reached a temperature elevation above 5 °C, with similar results for the other two concentrations, 200 and 1000 μ g/ml, and which is enough to perform MHT. This is an advantage compared to previous works, where the particle concentrations required to perform MHT are higher and start from 0.5 mg/ml for spherical particles that are similar to those in this work [116].

The effects of the MHT at different particle concentrations can be observed in both subsequent experiments on MHT, the cells' staining, and their protein analyses. In the staining micrographs, it is appreciated how the cellular structure of the membrane and organelles was lost as the concentration of MNPs increased. Such results are consistent with the protein analysis by electrophoresis, and the fact that no GAPDH bands were found by western blot, possibly due to their denaturation.

Our MNPs were able to perform MHT and presented other good properties despite the simplicity of their production; nevertheless, it is desirable to obtain a narrower size distribution, and if possible, shape control when synthesizing the particles. Additionally, better control of the environmental conditions when applying the MHT would be helpful to reduce external variables such as additional heating by convection or possible contamination.

Despite the reduction in viability and the denaturing of proteins following the application of the MHT, further studies could investigate which specific proteins are mainly affected by this treatment to better understand the metabolic pathways that lead to cell death after heat exposure.

Our results were consistent in proving the effectiveness of MHT with the synthesized MNPs; they not only reach the minimum temperature necessary to perform this treatment, but the posterior analysis showed abnormalities in the treated cells. This makes our particles good and novel candidates for MHT after only changing some of the original procedure conditions and making it easier to perform.

CHAPTER 5 CONCLUSIONS

5. Conclusions

Fe₃O₄ nanoparticles can be successfully synthesized by the co-precipitation route at room temperature by controlling the rate at which a determined volume of the reducing agent (NaOH) is added to the iron precursor solution. Specifically, when referring to magnetic nanomaterials for biomedical applications, these properties include crystallinity, monodispersity, biocompatibility, and superparamagnetism, which are essential for minimizing risks when used in biological systems.

The bioconjugation route is important to be considered since the particles' preparation, as long as their surface molecules could be considered the first step into a stable attachment that leads from the particle core to the most external biomolecule, which will interact in a desired way with their specific target, and avoiding changing the nanoparticle intrinsic properties.

A low concentration of MNPs is considered to be preferable as it reaches the same or better temperature increment when exposed to an AMF, it decreases the MNPs' cytotoxicity generated by themselves without MHT application, it reduces the "noise" when taking micrography images, not to mention the reduction in the particles' usage and waste diminution.

MHT is a promising cancer treatment as it can be specifically designed to attack cancerous cells with the advantages of targeted therapy, as well as regulated use in temperature increase to only affect cancer cells, causing minimal damage to healthy cells.

References

- [1] M. Hejmadi, Introduction to Cancer Biology, 2nd ed., 2010. https://doi.org/10.1517/14656566.2.4.613.
- [2] An Overview of Colorectal Cancer | Gleneagles Hospital Johor, (n.d.). https://gleneagles.com.my/johor/articles/an-overview-of-colorectal-cancer (accessed March 13, 2025).
- [3] Colorectal cancer, (n.d.). https://www.who.int/news-room/fact-sheets/detail/colorectal-cancer (accessed March 13, 2025).
- [4] J.D. Vogel, S.I. Felder, A.R. Bhama, A.T. Hawkins, S.J. Langenfeld, V.O. Shaffer, A.J. Thorsen, M.R. Weiser, G.J. Chang, A.L. Lightner, D.L. Feingold, I.M. Paquette, The American Society of Colon and Rectal Surgeons Clinical Practice Guidelines for the Management of Colon Cancer, Dis. Colon Rectum. 65 (2022) 148–177. https://doi.org/10.1097/DCR.0000000000002323.
- [5] N.C.I. NIH, Side Effects of Cancer Treatment | CDC, (2019) 11–12. https://www.cancer.gov/about-cancer/treatment/side-effects (accessed July 11, 2022).
- [6] A.B. Salunkhe, V.M. Khot, S.H. Pawar, Magnetic Hyperthermia with Magnetic Nanoparticles: A Status Review, Curr. Top. Med. Chem. 14 (2014) 572–594. https://doi.org/10.2174/1568026614666140118203550.
- [7] Mohite, Self Contrilled Magnetic Hyperthermia, CWL Publ. Enterp. Inc., Madison. 2004 (2004) 352. https://repository.lib.fsu.edu/islandora/object/fsu:180575.
- [8] Z. Hedayatnasab, F. Abnisa, W.M.A.W. Daud, Review on magnetic nanoparticles for magnetic nanofluid hyperthermia application, Mater. Des. 123 (2017) 174–196. https://doi.org/10.1016/j.matdes.2017.03.036.
- [9] C. Sun, J.S.H. Lee, M. Zhang, Magnetic nanoparticles in MR imaging and drug delivery, Adv. Drug Deliv. Rev. 60 (2008) 1252–1265. https://doi.org/10.1016/J.ADDR.2008.03.018.
- [10] D. Hanahan, R.A. Weinberg, Hallmarks of cancer: The next generation, Cell. 144 (2011) 646–674. https://doi.org/10.1016/j.cell.2011.02.013.
- [11] A. Urruticoechea, R. Alemany, J. Balart, A. Villanueva, F. Vinals, G. Capella, Recent advances in cancer therapy: an overview, Curr. Pharm. Des. 16 (2010) 3–10. https://doi.org/10.2174/138161210789941847.
- [12] Types of Cancer Treatment NCI, (n.d.). https://www.cancer.gov/about-cancer/treatment/types (accessed April 7, 2025).
- [13] A. Chicheł, J. Skowronek, M. Kubaszewska, M. Kanikowski, Hyperthermia Description of a method and a review of clinical applications, Reports Pract.

- Oncol. Radiother. 12 (2007) 267–275. https://doi.org/10.1016/S1507-1367(10)60065-X.
- [14] P. Wust, B. Hildebrandt, G. Sreenivasa, B. Rau, J. Gellermann, H. Riess, R. Felix, P. Schlag, Hyperthermia in combined treatment of cancer, Lancet Oncol. 3 (2002) 487–497. https://doi.org/10.1016/S1470-2045(02)00818-5.
- [15] M. H. Falk, R. D. Issels, Hyperthermia in oncology, Int. J. Hyperth. 17 (2001) 1–18. https://doi.org/10.1080/02656730118511.
- [16] Q. Dai, B. Cao, S. Zhao, A. Zhang, Synergetic Thermal Therapy for Cancer: State-of-the-Art and the Future, Bioengineering. 9 (2022). https://doi.org/10.3390/bioengineering9090474.
- [17] V. Mohite, Self Controlled Magnetic Hyperthermia, 2004.
- [18] B. Hildebrandt, P. Wust, O. Ahlers, A. Dieing, G. Sreenivasa, T. Kerner, R. Felix, H. Riess, The cellular and molecular basis of hyperthermia, Crit. Rev. Oncol. Hematol. 43 (2002) 33–56. https://doi.org/10.1016/S1040-8428(01)00179-2.
- [19] J.L. Roti Roti, Introduction: Radiosensitization by hyperthermia, Int. J. Hyperth. 20 (2004) 109–114. https://doi.org/10.1080/0265673032000173898.
- [20] K. Aloss, P. Hamar, Augmentation of the EPR effect by mild hyperthermia to improve nanoparticle delivery to the tumor, Biochim. Biophys. Acta - Rev. Cancer. 1879 (2024). https://doi.org/10.1016/j.bbcan.2024.189109.
- [21] M.H.M.G.M. Den Brok, R.P.M. Sutmuller, R. Van Der Voort, E.J. Bennink, C.G. Figdor, T.J.M. Ruers, G.J. Adema, In situ tumor ablation creates an antigen source for the generation of antitumor immunity, Cancer Res. 64 (2004) 4024–4029. https://doi.org/10.1158/0008-5472.CAN-03-3949.
- [22] J. van der Zee, Heating the patient: A promising approach?, Ann. Oncol. 13 (2002) 1173–1184. https://doi.org/10.1093/annonc/mdf280.
- [23] S.A. Curley, Radiofrequency Ablation of Malignant Liver Tumors, Oncologist. 6 (2001) 14–23. https://doi.org/10.1634/theoncologist.6-1-14.
- [24] L. Xiaoping, Z. Leizhen, Advances of high intensity focused ultrasound (HIFU) for pancreatic cancer, Int. J. Hyperth. 29 (2013) 678–682. https://doi.org/10.3109/02656736.2013.837199.
- [25] S. Krishnan, P. Diagaradjane, S.H. Cho, Nanoparticle-mediated thermal therapy: Evolving strategies for prostate cancer therapy, Int. J. Hyperth. 26 (2010) 775–789. https://doi.org/10.3109/02656736.2010.485593.
- [26] P. Wust, U. Gneveckow, M. Johannsen, D. Böhmer, T. Henkel, F. Kahmann, J. Sehouli, R. Felix, J. Ricke, A. Jordan, Magnetic nanoparticles for interstitial thermotherapy Feasibility, tolerance and achieved temperatures, Int. J. Hyperth. 22 (2006) 673–685. https://doi.org/10.1080/02656730601106037.
- [27] Z. Liu, Gastrointestinal cancers, 2019.

- https://doi.org/10.1201/9781351208277-17.
- [28] Colon cancer Symptoms and causes Mayo Clinic, (n.d.). https://www.mayoclinic.org/diseases-conditions/colon-cancer/symptoms-causes/syc-20353669 (accessed July 7, 2025).
- [29] G. Cao, Nanostructures and Nanomaterials, PUBLISHED BY IMPERIAL COLLEGE PRESS AND DISTRIBUTED BY WORLD SCIENTIFIC PUBLISHING CO., 2004. https://doi.org/10.1142/p305.
- [30] S. Lanone, J. Boczkowski, Biomedical Applications and Potential Health Risks of Nanomaterials: Molecular Mechanisms, Curr. Mol. Med. 6 (2006) 651–663. https://doi.org/10.2174/156652406778195026.
- [31] V. Wagner, A. Dullaart, A.K. Bock, A. Zweck, The emerging nanomedicine landscape, Nat. Biotechnol. 24 (2006) 1211–1217. https://doi.org/10.1038/nbt1006-1211.
- [32] O.C. Farokhzad, R. Langer, Nanomedicine: Developing smarter therapeutic and diagnostic modalities, Adv. Drug Deliv. Rev. 58 (2006) 1456–1459. https://doi.org/10.1016/j.addr.2006.09.011.
- [33] X. Chen, S.T.C. Wong, Cancer Theranostics: An Introduction, Cancer Theranostics. (2014) 3–8. https://doi.org/10.1016/B978-0-12-407722-5.00001-3.
- [34] V.S. Sivasankarapillai, A.K. Somakumar, J. Joseph, S. Nikazar, A. Rahdar, G.Z. Kyzas, Cancer theranostic applications of MXene nanomaterials: Recent updates, Nano-Structures and Nano-Objects. 22 (2020) 100457. https://doi.org/10.1016/j.nanoso.2020.100457.
- [35] D.O. Lapotko, Nanophotonics and theranostics: Will light do the magic?, Theranostics. 3 (2013) 138–140. https://doi.org/10.7150/thno.6062.
- [36] V. Mody, R. Siwale, A. Singh, H. Mody, Introduction to metallic nanoparticles, J. Pharm. Bioallied Sci. 2 (2010) 282. https://doi.org/10.4103/0975-7406.72127.
- [37] N.T. Khan, M.J. Khan, Metallic Nanoparticles Fabrication Methods— A Brief Overview., SunKrist Nanotechnol. Nanosci. J. 2 (2020) 1–6. https://doi.org/10.46940/snnj.02.1002.
- [38] T. Yonezawa, Preparation of Metal Nanoparticles and Their Application for Materials, Elsevier B.V., 2018. https://doi.org/10.1016/B978-0-444-64110-6.00085-8.
- [39] Z.R. Stephen, F.M. Kievit, M. Zhang, Magnetite nanoparticles for medical MR imaging, Mater. Today. 14 (2011) 330–338. https://doi.org/10.1016/S1369-7021(11)70163-8.
- [40] and M.Z. Conroy Sun, Jerry S.H. Lee, Magnetic Nanoparticles in MR Imaging and Drug Delivery, Bone. 23 (2008) 1–7.

- https://doi.org/10.1016/j.addr.2008.03.018.
- [41] A. Lahooti, S. Shanehsazzadeh, S. Laurent, Dual-Modality Imaging, Elsevier Ltd., 2018. https://doi.org/10.1016/b978-0-08-101925-2.00006-1.
- [42] S. Laurent, S. Boutry, I. Mahieu, L. Elst, R. Muller, Iron Oxide Based MR Contrast Agents: from Chemistry to Cell Labeling, Curr. Med. Chem. 16 (2009) 4712–4727. https://doi.org/10.2174/092986709789878256.
- [43] P.B. Tsitovich, P.J. Burns, A.M. McKay, J.R. Morrow, Redox-activated MRI contrast agents based on lanthanide and transition metal ions, J. Inorg. Biochem. 133 (2014) 143–154. https://doi.org/10.1016/j.jinorgbio.2014.01.016.
- [44] I. Ocsoy, D. Tasdemir, S. Mazicioglu, C. Celik, A. Katı, F. Ulgen, Biomolecules incorporated metallic nanoparticles synthesis and their biomedical applications, Mater. Lett. 212 (2018) 45–50. https://doi.org/10.1016/j.matlet.2017.10.068.
- [45] Z. Liu, J. T. Robinson, X. Sun, H. Dai, PEGylated Nanographene Oxide for Delivery of Water-Insoluble Cancer Drugs, J. Am. Chem. Soc. 130 (2008) 10876–10877. https://doi.org/10.1021/ja803688x.
- [46] S. Trigueros, Nanoscale Metal Particles as Nanocarriers in Targeted Drug Delivery System, J. Nanomedicine Res. 4 (2016) 2–7. https://doi.org/10.15406/jnmr.2016.04.00086.
- [47] J. Conde, G. Doria, P. Baptista, Noble Metal Nanoparticles Applications in Cancer, J. Drug Deliv. 2012 (2012) 1–12. https://doi.org/10.1155/2012/751075.
- [48] G. Paramasivam, N. Kayambu, A.M. Rabel, A.K. Sundramoorthy, A. Sundaramurthy, Anisotropic noble metal nanoparticles: Synthesis, surface functionalization and applications in biosensing, bioimaging, drug delivery and theranostics, Acta Biomater. 49 (2017) 45–65. https://doi.org/10.1016/j.actbio.2016.11.066.
- [49] G.F. Paciotti, D.G.I. Kingston, L. Tamarkin, Colloidal gold nanoparticles: A novel nanoparticle platform for developing multifunctional tumor-targeted drug delivery vectors, Drug Dev. Res. 67 (2006) 47–54. https://doi.org/10.1002/ddr.20066.
- [50] J.-A.L. Mhatre V. Ho and Kelsey C. Martin, The optical, photothermal, and facile surface chemical properties of gold and silver nanoparticles in biodiagnostics, therapy, and drug delivery, Bone. 23 (2012) 1–7. https://doi.org/10.1007/s00204-014-1245-3.The.
- [51] I.H. El-Sayed, X. Huang, M.A. El-Sayed, Selective laser photo-thermal therapy of epithelial carcinoma using anti-EGFR antibody conjugated gold nanoparticles, Cancer Lett. 239 (2006) 129–135. https://doi.org/10.1016/j.canlet.2005.07.035.

- [52] M.K. Popp, I. Oubou, C. Shepherd, Z. Nager, C. Anderson, L. Pagliaro, Photothermal therapy using gold nanorods and near-infrared light in a murine melanoma model increases survival and decreases tumor volume, J. Nanomater. 2014 (2014). https://doi.org/10.1155/2014/450670.
- [53] M. Kim, J. Lee, J. Nam, Plasmonic Photothermal Nanoparticles for Biomedical Applications, Adv. Sci. 6 (2019) 1900471. https://doi.org/10.1002/advs.201900471.
- [54] G. Gao, Y.W. Jiang, W. Sun, Y. Guo, H.R. Jia, X.W. Yu, G.Y. Pan, F.G. Wu, Molecular Targeting-Mediated Mild-Temperature Photothermal Therapy with a Smart Albumin-Based Nanodrug, Small. 15 (2019) 1–15. https://doi.org/10.1002/smll.201900501.
- [55] C.L. West, A.C.V. Doughty, K. Liu, W.R. Chen, Monitoring tissue temperature during photothermal therapy for cancer, J. Bio-X Res. 2 (2019) 159–168. https://doi.org/10.1097/jbr.00000000000050.
- [56] I.P. Gomes, J.A. Duarte, A.L.C. Maia, D. Rubello, D.M. Townsend, A.L.B. de Barros, E.A. Leite, Thermosensitive nanosystems associated with hyperthermia for cancer treatment, Pharmaceuticals. 12 (2019). https://doi.org/10.3390/ph12040171.
- [57] G. Nijhawan, S.S. Nijhawan, M. Sethi, Hyperthermia Treatments, Noble Met. Oxide Hybrid Nanoparticles Fundam. Appl. (2018) 241–263. https://doi.org/10.1016/B978-0-12-814134-2.00012-7.
- [58] R.W.Y. Habash, R. Bansal, D. Krewski, H.T. Alhafid, Thermal therapy, Part 1: An introduction to thermal therapy, Crit. Rev. Biomed. Eng. 34 (2006) 459–489. https://doi.org/10.1615/CritRevBiomedEng.v34.i6.20.
- [59] M.H. Falk, R.D. Issels, Hyperthermia in oncology, Int. J. Hyperth. 17 (2001) 1–18. https://doi.org/10.1080/02656730150201552.
- [60] R.K. GILCHRIST, R. MEDAL, W.D. SHOREY, R.C. HANSELMAN, J.C. PARROTT, C.B. TAYLOR, Selective inductive heating of lymph nodes, Ann. Surg. 146 (1957) 596–606. https://doi.org/10.1097/00000658-195710000-00007.
- [61] X. Liu, Y. Zhang, Y. Wang, W. Zhu, G. Li, X. Ma, Y. Zhang, S. Chen, S. Tiwari, K. Shi, S. Zhang, H.M. Fan, Y.X. Zhao, X.J. Liang, Comprehensive understanding of magnetic hyperthermia for improving antitumor therapeutic efficacy, Theranostics. 10 (2020) 3793–3815. https://doi.org/10.7150/thno.40805.
- [62] C. Blanco-Andujar, F.J. Teran, D. Ortega, Current Outlook and Perspectives on Nanoparticle-Mediated Magnetic Hyperthermia, Elsevier Ltd., 2018. https://doi.org/10.1016/b978-0-08-101925-2.00007-3.
- [63] R.M. Fratila, J.M. de la Fuente, Introduction to Hyperthermia, Nanomater. Magn. Opt. Hyperth. Appl. (2018) 1–10. https://doi.org/10.1016/B978-0-12-

- 813928-8.09997-X.
- [64] W. Wu, Z. Wu, T. Yu, C. Jiang, W.S. Kim, R.M. Fratila, J.M. de la Fuente, Recent progress on magnetic iron oxide nanoparticles: Synthesis, surface functional strategies and biomedical applications, Sci. Technol. Adv. Mater. 16 (2015) 23501. https://doi.org/10.1088/1468-6996/16/2/023501.
- [65] G. Salas, C. Casado, F.J. Teran, R. Miranda, C.J. Serna, M.P. Morales, Controlled synthesis of uniform magnetite nanocrystals with high-quality properties for biomedical applications, J. Mater. Chem. 22 (2012) 21065– 21075. https://doi.org/10.1039/c2jm34402e.
- [66] J. Park, K. An, Y. Hwang, J.E.G. Park, H.J. Noh, J.Y. Kim, J.H. Park, N.M. Hwang, T. Hyeon, Ultra-large-scale syntheses of monodisperse nanocrystals, Nat. Mater. 3 (2004) 891–895. https://doi.org/10.1038/nmat1251.
- [67] R.E. Rosensweig, Heating magnetic fluid with alternating magnetic field, J. Magn. Magn. Mater. 252 (2002) 370–374. https://doi.org/10.1016/S0304-8853(02)00706-0.
- [68] R. Chen, M.G. Christiansen, P. Anikeeva, Maximizing hysteretic losses in magnetic ferrite nanoparticles via model-driven synthesis and materials optimization, ACS Nano. 7 (2013) 8990–9000. https://doi.org/10.1021/nn4035266.
- [69] P.J. Sugumaran, X.L. Liu, T.S. Herng, E. Peng, J. Ding, GO-Functionalized Large Magnetic Iron Oxide Nanoparticles with Enhanced Colloidal Stability and Hyperthermia Performance, ACS Appl. Mater. Interfaces. (2019). https://doi.org/10.1021/acsami.9b04261.
- [70] S.H. Noh, W. Na, J.T. Jang, J.H. Lee, E.J. Lee, S.H. Moon, Y. Lim, J.S. Shin, J. Cheon, Nanoscale magnetism control via surface and exchange anisotropy for optimized ferrimagnetic hysteresis, Nano Lett. 12 (2012) 3716–3721. https://doi.org/10.1021/nl301499u.
- [71] Y. Yang, X. Liu, Y. Lv, T.S. Herng, X. Xu, W. Xia, T. Zhang, J. Fang, W. Xiao, J. Ding, Orientation Mediated Enhancement on Magnetic Hyperthermia of Fe ₃ O ₄ Nanodisc, Adv. Funct. Mater. 25 (2015) 812–820. https://doi.org/10.1002/adfm.201402764.
- [72] W. Xiao, X. Liu, X. Hong, Y. Yang, Y. Lv, J. Fang, J. Ding, Magnetic-field-assisted synthesis of magnetite nanoparticles via thermal decomposition and their hyperthermia properties, CrystEngComm. 17 (2015) 3652–3658. https://doi.org/10.1039/c5ce00442j.
- [73] M. Colombo, S. Carregal-Romero, M.F. Casula, L. Gutiérrez, M.P. Morales, I.B. Böhm, J.T. Heverhagen, D. Prosperi, W.J. Parak, Biological applications of magnetic nanoparticles, Chem. Soc. Rev. 41 (2012) 4306–4334. https://doi.org/10.1039/c2cs15337h.

- [74] M. Creixell, A.C. Bohórquez, M. Torres-Lugo, C. Rinaldi, EGFR-targeted magnetic nanoparticle heaters kill cancer cells without a perceptible temperature rise, ACS Nano. 5 (2011) 7124–7129. https://doi.org/10.1021/nn201822b.
- [75] W. Wu, Æ.Q. He, Æ.C. Jiang, Magnetic Iron Oxide Nanoparticles: Synthesis and Surface Functionalization Strategies, (2008) 397–415. https://doi.org/10.1007/s11671-008-9174-9.
- [76] M. Ferreira, J. Sousa, A. Pais, C. Vitorino, The role of magnetic nanoparticles in cancer nanotheranostics, Materials (Basel). 13 (2020) 1–25. https://doi.org/10.3390/ma13020266.
- [77] W. Wu, Q.G. He, R. Hu, J.K. Huang, H. and Chen, Preparation and characterization of magnetite Fe3O4 nanopowders, Rare Met. Mater. Eng. 36 (2007) 238. https://www.researchgate.net/publication/295728921_Preparation_and_characterization_of_magnetite_Fe3O4_nanopowders (accessed December 10, 2020).
- [78] C. Pereira, A. M. Pereira, C. Fernandes, M. Rocha, R. Mendes, M. Paz Fernández-García, A. Guedes, P. B. Tavares, J.-M. Grenèche, J. P. Araújo, C. Freire, Superparamagnetic MFe2O4 (M = Fe, Co, Mn) Nanoparticles: Tuning the Particle Size and Magnetic Properties through a Novel One-Step Coprecipitation Route, Chem. Mater. 24 (2012) 1496–1504. https://doi.org/10.1021/cm300301c.
- [79] S. Sun, H. Zeng, Size-Controlled Synthesis of Magnetite Nanoparticles, J. Am. Chem. Soc. 124 (2002) 8204–8205. https://doi.org/10.1021/ja026501x.
- [80] J. Rockenberger, E. C. Scher, A. Paul Alivisatos, A New Nonhydrolytic Single-Precursor Approach to Surfactant-Capped Nanocrystals of Transition Metal Oxides, J. Am. Chem. Soc. 121 (1999) 11595–11596. https://doi.org/10.1021/ja993280v.
- [81] K. Woo, J. Hong, S. Choi, H.-W. Lee, J.-P. Ahn, C. Sung Kim, S. Won Lee, Easy Synthesis and Magnetic Properties of Iron Oxide Nanoparticles, Chem. Mater. 16 (2004) 2814–2818. https://doi.org/10.1021/cm049552x.
- [82] T. Hyeon, S. Seong Lee, J. Park, Y. Chung, H. Bin Na, Synthesis of Highly Crystalline and Monodisperse Maghemite Nanocrystallites without a Size-Selection Process, J. Am. Chem. Soc. 123 (2001) 12798–12801. https://doi.org/10.1021/ja016812s.
- [83] X. Sun, C. Zheng, F. Zhang, Y. Yang, G. Wu, A. Yu, N. Guan, Size-Controlled Synthesis of Magnetite (Fe3O4) Nanoparticles Coated with Glucose and Gluconic Acid from a Single Fe(III) Precursor by a Sucrose Bifunctional Hydrothermal Method, J. Phys. Chem. C. 113 (2009) 16002–16008. https://doi.org/10.1021/jp9038682.
- [84] G. Gao, R. Shi, W. Qin, Y. Shi, G. Xu, G. Qiu, X. Liu, Solvothermal synthesis

- and characterization of size-controlled monodisperse Fe3O4 nanoparticles, J. Mater. Sci. 45 (2010) 3483–3489. https://doi.org/10.1007/s10853-010-4378-7.
- [85] J.S. Xu, Y.J. Zhu, α-Fe2O3 hierarchically hollow microspheres self-assembled with nanosheets: Surfactant-free solvothermal synthesis, magnetic and photocatalytic properties, CrystEngComm. 13 (2011) 5162–5169. https://doi.org/10.1039/c1ce05252g.
- [86] J. Ma, J. Lian, X. Duan, X. Liu, W. Zheng, α-Fe2O3: Hydrothermal Synthesis, Magnetic and Electrochemical Properties, J. Phys. Chem. C. 114 (2010) 10671–10676. https://doi.org/10.1021/jp102243g.
- [87] T. J. Daou, G. Pourroy, S. Bégin-Colin, J. M. Grenèche, C. Ulhaq-Bouillet, P. Legaré, P. Bernhardt, C. Leuvrey, G. Rogez, Hydrothermal Synthesis of Monodisperse Magnetite Nanoparticles, Chem. Mater. 18 (2006) 4399–4404. https://doi.org/10.1021/cm060805r.
- [88] A.K. Gupta, M. Gupta, Synthesis and surface engineering of iron oxide nanoparticles for biomedical applications, Biomaterials. 26 (2005) 3995–4021. https://doi.org/10.1016/j.biomaterials.2004.10.012.
- [89] C. Bednarek, U. Schepers, F. Thomas, S. Bräse, Bioconjugation in Materials Science, Adv. Funct. Mater. 34 (2024). https://doi.org/10.1002/adfm.202303613.
- [90] S.L. Goodman, M. Picard, Integrins as therapeutic targets, Trends Pharmacol. Sci. 33 (2012) 405–412. https://doi.org/10.1016/j.tips.2012.04.002.
- [91] M. Barczyk, S. Carracedo, D. Gullberg, Integrins, Cell Tissue Res. 339 (2010) 269–280. https://doi.org/10.1007/S00441-009-0834-6,.
- [92] N.A. Spaldin, Magnetic Materials Fundamentals and Applications, 2nd ed., Cambridge, 2019. http://scioteca.caf.com/bitstream/handle/123456789/1091/RED2017-Eng-8ene.pdf?sequence=12&isAllowed=y%0Ahttp://dx.doi.org/10.1016/j.regsciurbeco.2008.06.005%0Ahttps://www.researchgate.net/publication/305320484_SISTEM_PEMBETUNGAN_TERPUSAT_STRATEGI_MELESTARI.
- [93] C. Kittel, Introduction to Solid State Physics, 1957. https://doi.org/10.1088/0031-9112/8/9/012.
- [94] N.D. Thorat, O.M. Lemine, R.A. Bohara, K. Omri, L. El Mir, S.A.M. Tofail, Superparamagnetic iron oxide nanocargoes for combined cancer thermotherapy and MRI applications, Phys. Chem. Chem. Phys. 18 (2016) 21331–21339. https://doi.org/10.1039/c6cp03430f.
- [95] N.A. Frey, S. Peng, K. Cheng, S. Sun, Magnetic nanoparticles: Synthesis, functionalization, and applications in bioimaging and magnetic energy storage, Chem. Soc. Rev. 38 (2009) 2532–2542.

- https://doi.org/10.1039/b815548h.
- [96] X. Liu, N. Fang, C. Li, X. Li, H. Liu, J. Wu, A free-standing magneto-fluorescent La1-xSrxMnO3@ZnO nanoparticle: Synthesis, properties and sharp Curie transition, J. Alloys Compd. 693 (2017) 518–526. https://doi.org/10.1016/J.JALLCOM.2016.09.212.
- [97] A.G. Kolhatkar, A.C. Jamison, D. Litvinov, R.C. Willson, T.R. Lee, Tuning the Magnetic Properties of Nanoparticles, Int. J. Mol. Sci. 2013, Vol. 14, Pages 15977-16009. 14 (2013) 15977–16009. https://doi.org/10.3390/IJMS140815977.
- [98] A.J. GIUSTINI, A.A. PETRYK, S.M. CASSIM, J.A. TATE, I. BAKER, P.J. HOOPES, Magnetic Nanoparticle Hyperthermia in Cancer Treatment, Nano Life. 01 (2010) 17–32. https://doi.org/10.1142/s1793984410000067.
- [99] M. Mahmoudi, S. Sant, B. Wang, S. Laurent, T. Sen, Superparamagnetic iron oxide nanoparticles (SPIONs): Development, surface modification and applications in chemotherapy, Adv. Drug Deliv. Rev. 63 (2011) 24–46. https://doi.org/10.1016/J.ADDR.2010.05.006.
- [100] L.L. Vatta, R.D. Sanderson, K.R. Koch, Magnetic nanoparticles: Properties and potential applications, Pure Appl. Chem. 78 (2006) 1793–1801. https://doi.org/10.1351/pac200678091793.
- [101] F. Liu, Y. Hou, S. Gao, Exchange-coupled nanocomposites: Chemical synthesis, characterization and applications, Chem. Soc. Rev. 43 (2014) 8098–8113. https://doi.org/10.1039/c4cs00162a.
- [102] K. Kalantar-zadeh, B. Fry, Nanotechnology-Enabled Sensors, (n.d.).
- [103] M.J. Murty, B.S., Shakar P., Raj B., Rath B.B., Textbook of Nanoscience and Nanotechnology, 1st ed., Springer, Universities Press (India), India, 2013. https://doi.org/10.1007/978-3-642-28030-6.
- [104] J.D.E. Gaffner J.S., Marley N.A., Fourier Transform Infrared Spectra, Fourier Transform Infrared Spectra. (1978). https://doi.org/10.1016/c2009-0-22072-1.
- [105] T. Brander, A. Gerfer, B. Rall, H. Zenkner, Trilogy of Magnetics-Design Guide for EMI Filter Design, SMPS & RF Circuits, 2018.
- [106] M.A. Dheyab, A.A. Aziz, M.S. Jameel, Simple rapid stabilization method through citric acid modification for magnetite nanoparticles, Sci. Rep. (2020) 1–9. https://doi.org/10.1038/s41598-020-67869-8.
- [107] U. Patel, K. Chauhan, S. Gupte, Synthesis, characterization and application of lipase-conjugated citric acid-coated magnetic nanoparticles for ester synthesis using waste frying oil, 3 Biotech. 8 (2018). https://doi.org/10.1007/s13205-018-1228-9.
- [108] G.A. Monteiro, M. Biotech, A. V Fernandes, H.G. Sundararaghavan, D. Ph, D.I. Shreiber, D. Ph, Positively and Negatively Modulating Cell Adhesion to

- Type I Collagen Via Peptide Grafting, 17 (2011).
- [109] Thermo Scientific, Bioconjugation and crosslinking technical handbook, (2022) 1–63. https://assets.thermofisher.com/TFS-Assets/BID/Handbooks/bioconjugation-technical-handbook.pdf.
- [110] M. Coïsson, G. Barrera, F. Celegato, L. Martino, S.N. Kane, S. Raghuvanshi, F. Vinai, P. Tiberto, Hysteresis losses and specific absorption rate measurements in magnetic nanoparticles for hyperthermia applications, Biochim. Biophys. Acta Gen. Subj. 1861 (2017) 1545–1558. https://doi.org/10.1016/j.bbagen.2016.12.006.
- [111] S.J.H. Soenen, M. De Cuyper, Assessing iron oxide nanoparticle toxicity in vitro: Current status and future prospects, Nanomedicine. 5 (2010) 1261–1275. https://doi.org/10.2217/nnm.10.106.
- [112] Z. Sun, V. Yathindranath, M. Worden, J.A. Thliveris, S. Chu, F.E. Parkinson, T. Hegmann, D.W. Miller, Characterization of cellular uptake and toxicity of aminosilane-coated iron oxide nanoparticles with different charges in central nervous system-relevant cell culture models, Int. J. Nanomedicine. 8 (2013) 961–970. https://doi.org/10.2147/IJN.S39048.
- [113] K. Rowatt, R.E. Burns, S. Frasca, D.M. Long, A combination Prussian blue–hematoxylin and eosin staining technique for identification of iron and other histological features, J. Histotechnol. 41 (2018) 29–34. https://doi.org/10.1080/01478885.2017.1417696.
- [114] J. Sambrook, D.W. Russell, SDS-Polyacrylamide Gel Electrophoresis of Proteins, Cold Spring Harb. Protoc. 2006 (2006) pdb.prot4540. https://doi.org/10.1101/PDB.PROT4540,.
- [115] M. Aslam, E.A. Schultz, T. Sun, T. Meade, V.P. Dravid, Synthesis of amine-stabilized aqueous colloidal iron oxide nanoparticles, Cryst. Growth Des. 7 (2007) 471–475. https://doi.org/10.1021/cg060656p.
- [116] A. Włodarczyk, S. Gorgoń, A. Radoń, K. Bajdak-Rusinek, Magnetite Nanoparticles in Magnetic Hyperthermia and Cancer Therapies: Challenges and Perspectives, Nanomaterials. 12 (2022) 1–23. https://doi.org/10.3390/nano12111807.

Appendix – Publications

Materialo Lettero 313 (2022) 131718



Contents lists available at ScienceDirect

Materials Letters

journal homepage: www.elsevier.com/locate/matlet



Cellulose dialysis membrane tubing doped with gold nanoparticles as SERS substrate



ARTICLE INFO

Cellulose membrane Dialysis Gold-nanoparticles

ABSTRACT

In this study, we report for the first time the use of a dialysis method for simple preparation of a flexible substrate for Surface-Enhanced Raman Spectroscopy (SERS). The method consists of synthesized citrate gold nanoparticles capped with poly(allylamine-hydrochloride), poured into a commercial cellulose dialysis membrane, and set into a glass bealer with water under magnetic stirring for 48 h for dialysis. Then gold nanoparticles doped the cellulose membrane to get a SERS substrate, which was characterized by Raman spectroscopy using 4-Aminothio-phenol, and 4-Mercaptobensoic acid as a Raman probe in the range from 1×10⁻⁸ to 1×10⁻¹⁰M, Raman signal as a function of logarithm concentration shows a linear behavior and estimated analytical enhancement factor of the substrate using 4-Aminothiophenol was 4.3×105. The flexibility of our SERS substrate can be helpful in applications where solid SERS substrates have low performance. For example, when the surface needs bending for sample preparation or analysis, cut out into small pieces or washed without losing its SERS properties.

https://doi.org/10.1016/j.matlet.2022.131718

^a Photonics Department, Research Center in Optics A. C., León, Guanajuado, México
^b Department of Chemistry, Electronic and Biomedical Engineering, Division of Sciences and Engineering, University of Guanajuato, León, Guanajuato, México

J Nanopart Res (2023) 25:66 https://doi.org/10.1007/s11051-023-05711-8

RESEARCH PAPER



Facile synthesis of Fe₃O₄ nanoparticles at room temperature coated with meso-2,3-dimercaptosuccinic acid for improved biocompatibility

L. F. Gomez–Caballero · J. L. Pichardo-Molina D · Joel Briones · S. Oyarzún · J. C. Denardin · G. Basurto-Islas

Received: 20 October 2022 / Accepted: 12 March 2023

© The Author(s), under exclusive licence to Springer Nature B.V. 2023

Abstract Superparamagnetic magnetite Fe₃O₄ nanoparticles (NPs) were synthesized by the coprecipitation method and stabilized with meso-2,3-dimercaptosuccinic acid (DMSA) under ambient conditions and a nitrogen atmosphere at room temperature in one simple step. The X-ray diffraction (XRD) analysis of Fe₃O₄ NPs confirmed their cubic spinel structure with high crystallinity for both samples prepared with or without nitrogen atmosphere. The scanning electron microscopy analysis showed an average particle size of 15.0±3 nm and 23.0±5 nm in the absence and presence of nitrogen, respectively. Our particles have shown excellent magnetic properties with a high saturation magnetization (55 emu/g), low remanence (3.0 emu/g), and low coercivity (43 Oe). The method of synthesis proposed here offers excellent reproducibility of superparamagnetic NPs with narrow size distribution and low aggregation despite the simplicity of its preparation. The dose–response curves of the colorimetric assay MTT carried out in HCT 116 cell cultures in a range from 30 to 250 µg/mL reveal that magnetic nanoparticles coated with DMSA significantly improve their biocompatibility for applications like magnetic hyperthermia, magnetic resonance imaging, or biosensing.

Keywords Magnetite · Superparamagnetic · Nanoparticles · Coprecipitation · DMSA · Room-temperature synthesis

Introduction

Superparamagnetic nanoparticles (NPs) have acquired great attention for biomedical applications. Their preparation can be done at a low cost, showing good physical and chemical stability and biocompatibility. Besides, they can be designed to accomplish specific tasks [1, 2], for example, as a contrast agent in magnetic resonance imaging, magnetic hyperthermia therapy, cellular labeling, tracking in tumor therapy, targeted drug delivery systems, and soil and groundwater remediation, among other applications [3, 4]. These particles can be classified into two main categories depending on their structure: magnetic alloy nanoparticles and magnetic metal oxide nanoparticles. In the latter group, we can find iron oxide NPs (magnetite Fe₃O₄ and maghemite γ-Fe₂O₃) which have

L. F. Gomez–Caballero · J. L. Pichardo-Molina (⋈) · J. Briones

Photonics Department, Research Center in Optics A. C., León, Guanajuato, México e-mail: jpichardo@cio.mx

S. Oyarzún · J. C. Denardin Departamento de Fisica, Universidad de Santiago de Chile (USAH), Avenida Ecuador 3493, Santiago, Chile

G. Basurto-Islas
Department of Chemistry, Electronic and Biomedical
Engineering, Division of Sciences and Engineering,
University of Guanajuato, León, Guanajuato, México

Published online: 27 March 2023





Contents lists available at ScienceDirect

Materials Letters





Synthesis of magnetite nanoparticles by reduction in two different solvents

L.F. Gómez–Caballero **O, J.L. Pichardo-Molina ***, L. Aparicio-Ixta **O, ·T. Córdova-Fraga b, G. Basurto-Islas b

^a Research Center in Optics A. G., León, Guanajuato, Mexico ^b University of Guanajuato, León, Guanajuato, Mexico

ARTICLE INFO

Keywords: Analyte detection Magnetite Magnetic hyperthermia Octadecylamine

ABSTRACT

Magnetic nanoparticles (MNPs) have been studied in the last decades due to their properties and applications, acting as heating agents in magnetic hyperthermia or analytes detection, to mention a few. We developed magnetite (Pe₃O₄) MNPs capable of accomplishing previously mentioned applications. When stimulated with an alternating magnetic field (AMPs), our particles reached a temperature increment of 9 $^{\circ}$ C after being stimulated for 12 min. Also, they served as a peroxidase-like agent for H_2O_2 detection, reaching a limit of detection of 5 × 10^{-6} M. Our MNPs were synthesized by chemical reduction method using iron salts as precurroan doctade-cylamine as the reducing agent under a nitrogen atmosphere, in water or ethylene glycol. MNPs were characterized by X-ray diffraction, confirming their cubic spinel structure, and scanning electron microscopy analysis showed an average particle size of 35.0 and 34.0 nm, wheating sample magnetometry was used to analyze their magnetic properties, and UV-Vis spectroscopy to determine the Fe content of MNPs. The synthesis method here presents good reproducibility of MNPs with a moderate size distribution.

https://doi.org/10.1016/j.matlet.2025.138488